ADHESION MECHANISMS OF NANO-PARTICLE SILVER TO ELECTRONICS PACKAGING MATERIALS

A Thesis
Presented to
The Academic Faculty

By

Sung Chul Joo

In Partial Fulfillment of the Requirements for
the Degree Doctor of Philosophy
in Mechanical Engineering

Georgia Institute of Technology

December, 2009

ADHESION MECHANISMS OF NANO-PARTICLE SILVER TO ELECTRONICS PACKAGING MATERIALS

Approved by:

Dr. Daniel F. Baldwin, Advisor
School of Mechanical Engineering
Georgia Institute of Technology

Dr. C. P. Wong
Materials Science and Engineering
Georgia Institute of Technology

Dr. Steven Danyluk
School of Mechanical Engineering
Georgia Institute of Technology

Dr. Paul A. Kohl
Chemical and Biomolecular Engineering
Georgia Institute of Technology

Dr. Jianmin Qu
School of Mechanical Engineering
Georgia Institute of Technology

Date Approved: June 10th, 2009

To my families:

Sung Yong Lee, Chan Woo Joo, and Sa Rang Joo

My parents and parents-in-law

ACKNOWLEDGEMENTS

TABLE OF CONTENTS

LIST OF TABLES

LIST OF FIGURES

LIST OF SYMBOLS

H	Hardness
F_L	Indentation Load
d1, d2	Diagonal length of indentation mark ($(d1+d2) \div 2$)
T	Temperature
Ho	hardness at T= To=0℃,
So	Softening coefficient of hardness
$\Delta\gamma$	Surface energy change
γ_L	Total surface free energy of liquid
γ_S	Total surface free energy of solid
γ^{LW}	Lifshitz-van der Waals component of surface free energy
γ^{AB}	Acid-base component of surface free energy
γ^+	Lewis-acid parameter of surface free energy
γ^-	Lewis-base parameter of surface free energy
$W_{t(SL)}$	thermodynamic work of adhesion between solid and liquid
W_{SL}^{LW}	Lifshitz-van der Waals component of work of adhesion
W_{SL}^{AB}	Acid-base component of work of adhesion
θ	Contact angle
R_a	Arithmetic average surface roughness
D	Adhesive diameter
H	Adhesive heigh
F_c	Cohesive fracture force of NPS

F_f	Fracture force
σ_{UTS}	Ultimate tensile strength
t_{film}	Film thickness
F_i	Interfacial fracture force
F	Interface damage index
$\bar{\sigma}$	average tensile stress ($=\bar{\sigma}_z$)
$\bar{\tau}$	average shear stress ($=\sqrt{\tau_{xz}^2 + \tau_{yz}^2}$)
Z	interfacial bond strength in tension
S	interfacial bond strength in shear.
r_o	critical length.
P	normal force
t_i	thickness of each elastomeric layer
Ga	interfacial fracture energy at the fracture interface
Wa	Work of adhesion
E	Young's modulus
ν	Poisson's ratio
K	bulk modulus ($= E/3(1 - 2\nu)$)
a	contact radius
F_{vdw}	van der Waals force
h	van der Waals constant [eV]
d	particle diameter [um]
z_o	adhesion distance [Å]
$F_{vdw\,deform}$	additional van der Waals force due to deformation

$F_{total\ vdw}$ total adhesion force due to van der Waals force

$\sigma_{particle\ adhesion}$ particle adhesion strength

C_a adjusting constant

$H_{measured}$ measured substrate hardness (Vickers)

C_f fitting constant.

SUMMARY

To reduce electronics packaging lead time and potentially to reduce manufacturing cost, an innovative packaging process targeting rapid package prototyping (RPP) has been developed. The developed RPP process, which is based on a data-driven chip-first approach, provides electrical functionality as well as form factors for micro-systems packages. Such a technology will enable designers to rapidly and inexpensively make tangible prototypes of their electronics packaging designs in order to promptly assess new packaging materials and the performance of new devices.

The key component of the RPP process is the nano-particle silver (NPS) interconnect. However, NPS has not yet been adequately proven for use in electronics packaging applications. Moreover, its adhesion to electronics packaging materials such as polyimide, benzocyclobutene (BCB), copper, and aluminum is found to be weak. Thus, improving the adhesion strength of NPS will be a key issue for reliable package prototypes with NPS interconnects.

In this research, the adhesion of NPS to substrate materials is found to be attributed to particle adhesion and more specifically, van der Waals forces. An adhesion model based on the van der Waals force is suggested in order to predict NPS adhesion strength to packaging materials. A new adhesion test method that is based on a die shear test and a button shear test is developed to validate the NPS adhesion prediction model. The newly developed adhesion test method is generic in nature and can be extended to other thin films' adhesion tests. The NPS adhesion model provides a general and explicit relation between NPS tensile bond strength and adhesion factors such as substrate hardness, adhesion distance, van der Waals constant, and particle diameter. The NPS adhesion model is verified as a first order adhesion model using experimental data from

seventeen packaging materials. Substrate hardness is identified as a primary factor in NPS adhesion. Adhesion distance and van der Waals constant are also significant in organic and inorganic materials. Diffusion or other interfacial reaction between NPS and metal substrates such as copper and silver seems to exist. Finally, guidelines to improve the adhesion strength of NPS are suggested based on the adhesion model and on external adhesion factors such as Silane coupling agents and plasma treatment.

CHAPTER 1

INTRODUCTION

1.1 Problem Statement

Nano-particle silver (NPS) conductors are increasingly being investigated for package level electronics applications. Unlike traditional thick film materials and conductive inks, nano-particle conductors often do not incorporate compounds to promote interfacial adhesion such as binders used in thick films and polymer adhesives used in conductive inks, as these adhesion promoters can degrade the electrical performance.

The conventional thick film silver pasties are bonded to ceramic substrates due to inorganic binders such as glass frit or crystalline oxide powder. To improve wetting on a substrate and dispersion of a powder, surfactant can be added to the paste. The silver paste is fired, typically at peak temperatures of between 600°C and 1000°C, for a period of 20 – 60 min. During firing, the binder reacts with the ceramic substrate and forms a pillar structure, which provides a mechanical interlock in addition to a chemical bond to the metal film (Vest, 1986).

On the other hand, nano-particle silver, which is coated with a dispersion agent to prevent the particles from aggregation at room temperature, adheres to some metals and polymers during their sintering process at around 200°C for 60 min. Heat activates and removes the dispersion agent from the surface of the particles in order to initiate the connection among particles by atomic movement. However, the adhesion mechanism of the nano particle silver to substrate materials has not been identified yet. In particular, the

adhesion of nano-particle silver to polymer dielectric layers such as the widely used Kapton® dry film is concerned with low adhesion strength because the processed polymer surface is chemically inert.

Thus, in order to improve NPS adhesion, NPS adhesion mechanisms first need to be identified. Also, to check improvements in adhesion, a thin film adhesion test method should be developed, because conventional adhesion test methods are not directly applicable to the thin (~2um) NPS film. Therefore, in this thesis, the mechanism of NPS adhesion to organic and inorganic materials will be identified, and a new adhesion test method for measuring the interfacial bond strength of NPS film to substrates will be developed. NPS adhesion prediction model will be also developed, which provides explicit relationships between NPS tensile bond strength and adhesion factors. Finally, guidelines for improving the adhesion strength of NPS will be suggested and validated by conducting experiments.

1.2 Thesis objectives and structure

The primary objective of this thesis is to identify the mechanism by which nano-particle silver adheres to substrate materials and to improve the adhesion strength of nano-particle silver film for electronics packaging applications.

A motivation to the thesis is presented in Chapter 2. The focus of this chapter is to introduce the newly developed rapid package prototyping technology and the adhesion issue of nano-particle silver material used in the chip-first packaging technology. A comparison of nano-particle silver material to the conventional silver paste is also introduced in this chapter.

Chapter 3 deals with general adhesion mechanisms including adhesive adhesion mechanisms and particle adhesion mechanisms. Among all the adhesion mechanisms

considered, the adhesion mechanism relevant to NPS adhesion is extracted based on magnitude analysis and literature search. From each adhesion mechanism relevant to NPS adhesion, plausible adhesion factors are selected in this chapter.

Chapter 4 discusses the experimental results of evaluating the effects of plausible adhesion factors. A qualitative adhesion test method to quickly assess the adhesion level between NPS and various substrate materials is explained. Also, materials to NPS adhesion test are introduced in this chapter. The effects of substrate hardness, surface roughness, contact angle, hydrogen bonding, Silane coupling agent, and diffusion will be dealt with using experimental approach. The experimental results are analyzed and significant adhesion factors are identified in this chapter.

Chapter 5 presents a creative thin film adhesion test method that is developed to quantify the adhesion strength of NPS with various substrate materials. The reasons for ineffectiveness of existing adhesion test methods are explained. Test sample preparation, test procedure, force analysis, FEM analysis, interfacial fracture criterion, and Kendall's model are exhibited.

In Chapter 6, an existing adhesion model that contains significant factors for NPS adhesion is introduced. The adhesion model provides general and explicit relations between adhesion strength and adhesion factors. The adhesion model will be evaluated, and a modified adhesion prediction model will be developed by fitting the measured adhesion strength data using the adhesion test method described in Chapter 5. The adhesion prediction model is separately fitted into the experimental data for organic and inorganic materials because of the two distinctively different material property groups.

Each adhesion prediction model for organic and inorganic materials is verified in Chapter 7. Test materials used to verify the adhesion prediction model are also introduced. Comparisons between the model and the experimental results for these particular cases of

materials will be made to prove the validity of the adhesion prediction model. Finally, guidelines for improving the adhesion strength of NPS are suggested. The guidelines are based on the developed adhesion prediction model as well as extra adhesion factors that can be added by external assistance

Chapter 8 summarizes the conclusions of this research and presents several recommendations for future works.

CHAPTER 2

MOTIVATION AND BACKGROUND

2.1 Chip First Packaging Technology

The electronics packaging process is becoming more complex, and its complexity increases manufacturing cost and lead time. In addition, more electronics components for more functions must be placed in the limited space of an electronics package and the resulting high density makes it difficult to improve the mechanical and electrical reliability performance of electronics packages.

For the purpose of increasing the functional density of the electronics package, General Electric (GE) and Texas Instruments (TI) developed a chip-first approach, which is also called high density interconnect (HDI) as shown in Figure 2.1. In this approach, ICs are placed in the cavities of a ceramic or plastic substrate and bonded to the substrate. Above the substrate, a dielectric layer is formed, micro-vias are created by the laser drilling technique, and Ti/Cu/Ti metallization is used to form a multilayer interconnect (Daum, 1993).

As a similar HDI technology, Intel developed bumpless build-up layer packaging process that involves chips embedded in a bismaleimide triazine (BT) laminate or a copper heat spreader, which then has one or more build-up layers formed on top(Towle, 2001). A standard micro-via formation process makes the connections between the build-up layers and the chip pads. The embedding of the chips in the panel may be done with molding or dispensed encapsulation material.

In addition, the Technical University of Berlin and the Fraunhofer Institute IZM developed somewhat different HDI process (Topper, 2001). This process consists of die-

bonding to laser-cut windows of ceramic or silicon substrates by filling the gap between chips and substrate with an epoxy, planar embedding of multi chip module (MCM) by mechanical polishing of its backside, a standard thin film multi-layer process with a photosensitive polymers on the surface of the embedded substrate, and interconnects of bare dies or standard passive components to the copper routing of the MCM.
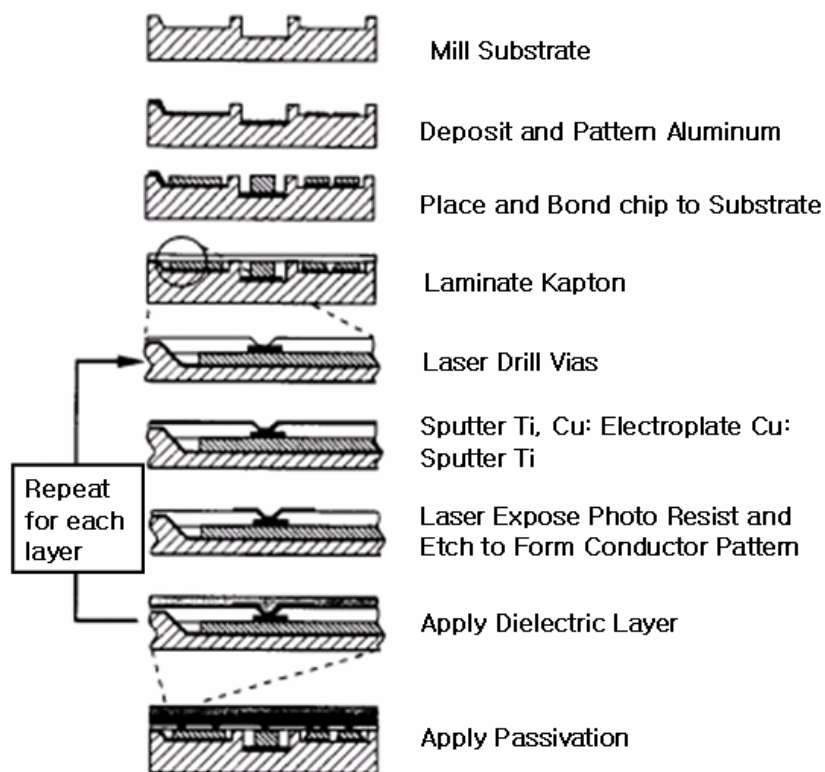
Figure 2.1 GE HDI fabrication process (Source: Daum, 1993)

Although the traditional HDI approaches can meet the requirements of increasing functional density, they cannot avoid the effect of extreme processing conditions required for standard IC fabrication such as vacuum sputtering and wet chemistry processing, and the capital constrains of vacuum and wet chemistry processing, critical factors influencing process complexity, the manufacturing cost, and the lead time of the process.

An innovative chip-first approach based on data-driven processes using nano-particle silver (NPS) as an interconnect and specifically targeting rapid package prototyping and low volume production in microelectronic packaging is being developed not only to reduce process complexity, manufacturing cost, and lead time but also to potentially enhance electrical and mechanical reliability performance.

The assembly process starts with a bare stainless steel or suitable substrate, where cavities for inserting chips are formed as shown in Figure 2.1. Chips are upside-down bonded into the cavities by compression bonding of a thermoplastic adhesive film. After the chips are bonded, polyimide or LCP film is laminated on the active surface of the chips and the substrate to form a thin film structure used for a dielectric layer. Through the dielectric layer micro-vias are drilled to the chip pads by an excimer-laser ablation technology. Finally, nano-particle metal is deposited to complete an electrical circuit by screen printing. The details of each process are discussed in the following sections.

2.1.1 Substrate

Historically, alumina, aluminum nitride, or silicon have been preferred as machinable substrate materials for the chip-first HDI technology (Topper, 1997). However, stainless steel was used in this process development in order to make a robust and flat substrate, and to form a heat spreader. The norminal thickness of the substrate is 0.625mm and it should be slightly larger than that of the thickest chip (0.6mm) for leveling coplanar in the lamination process. The computer-generated artwork of wire-electro discharge machining (w-EDM) mills cavities, where IC components are placed, in the stainless steel substrate. With respect to the chip size, slightly oversized cavities are cut into the stainless steel substrate so that the gap between the die and the cavity wall is filled by adhesives. The gap size in this experiment was designed as 100um on each side.

An array of two cavities with each side length of 5.23±0.02mm was milled in the stainless steel substrate with four ficucials of 1.01±0.02mm for a demonstration purpose as in Figure 2.3.
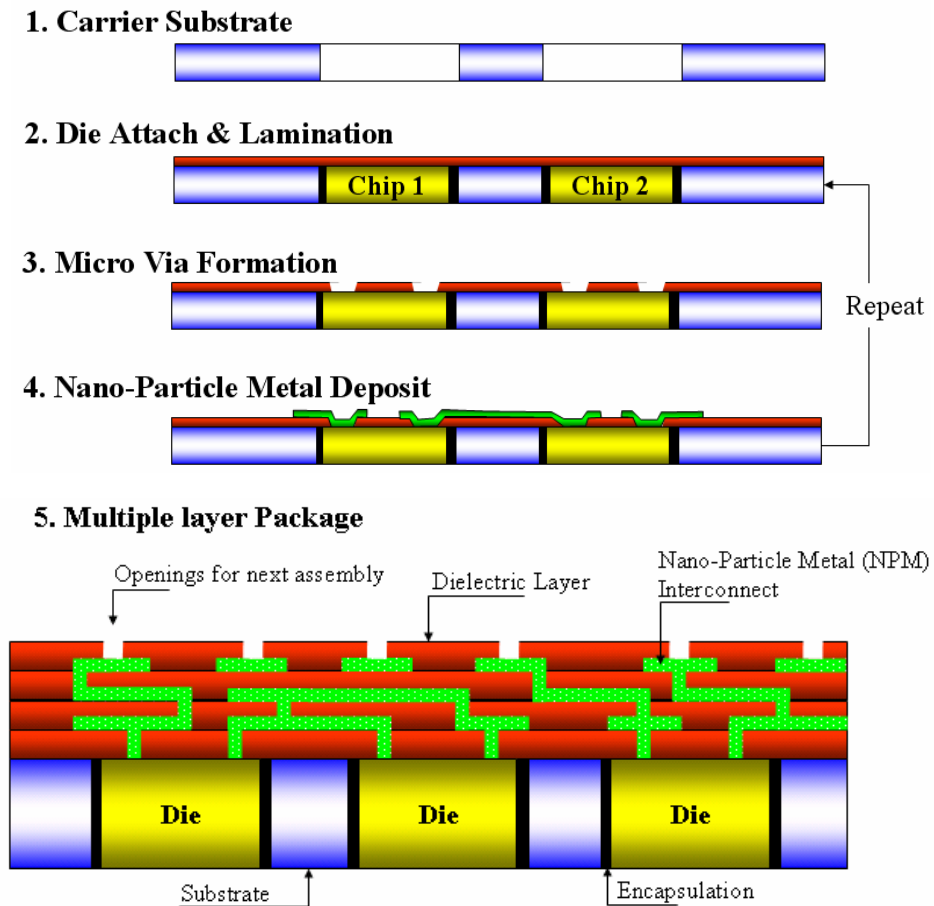
Figure 2.2 Schematic outline of a rapid package prototyping process
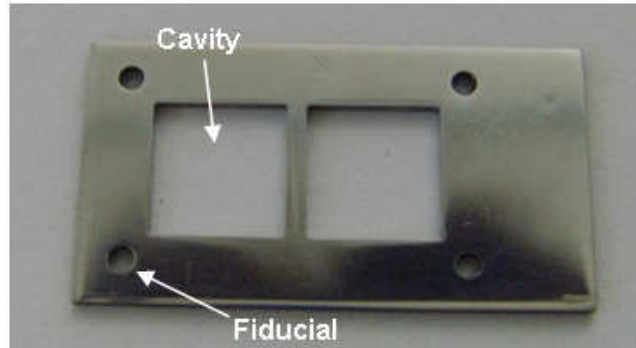
Figure 2.3 Photograph of stainless steel substrate

2.1.2 Die attach

A high precision pick and place machine, whose alignment tolerance is 5um, is used to align the dies of 5x5 mm size with the substrate cavities. In order to temporarily maintain the initial position of the dies aligned by the machine and to make a coplanar surface with the substrate, thermal resistant tape such as polyimide tape is attached to the top of the substrate as shown in Figure 2.4.

Components that are placed in the cavities are fixed by filling up the gap between dies and substrate using thermoplastic adhesive. The adhesive filling process is achieved by using a hot press as shown in Figure 2.5. In this figure, the aluminum foil is used to protect the platen from sticking to the adhesives. The temperature of the hot platen should be controlled to prevent the dies from moving inside the cavities. If dies move, resulting in the die position change from the initially designed location, then misalignment will take place in the following data-driven processes such as micro-via formation and NPS deposition. The die moving problem at high temperature has been one of the challenges in the typical chip-first approach. This challenge was resolved in this experment by controlling the temperature of the top and bottom platen as 315℃ and 200℃, respectively, as shown in Figure 2.5. The lower temperature of the bottom platen that is close to the polyimide tape prevents the adhesive of the polyimide tape from flowing, and

9

holds the initial position of the dies placed by the pick and place machine. In this step, the thermoplastic adhesive does not need to completely fill the gap because the complete filling will be done in the subsequent lamination step. Temperature below 200℃, however, was not sufficient for the thermoplastic adhesive to fill the gap and to hold the dies after detaching polyimide tape.

   After the thermoplastic adhesive is cured, the polyimide tape should be removed before the next lamination step. After removing the temporary polyimide tape, the die position should be checked to make sure that the initial position is maintained after die attach process. Figure 2.6 shows the die position before and after tape removal with the intentionally drawn cross mark for checking the relative position. The distances of A, A', B, and B' from each cross mark were measured and listed in Table 2.1. The die position was changed as much as 4 - 33 um after die attach in this experiment. This amount of die position change is acceptable as long as the micro-via size is large enough to expose the chip metal pads even under this amount of misalignment, and NPS ink can reach and connect to the exposed pads.
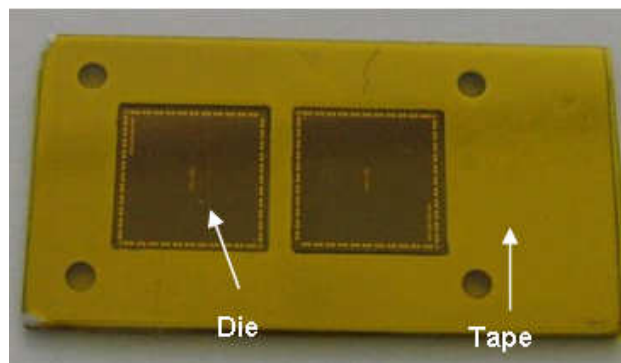
Figure 2.4 Polyimide tape attach
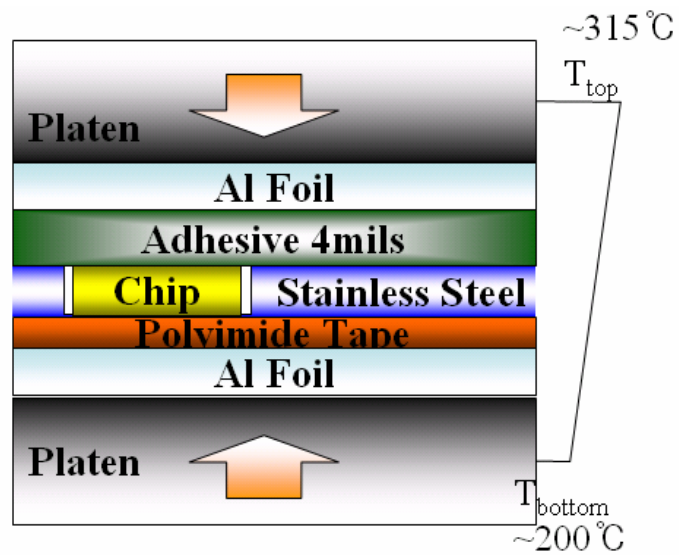
Figure 2.5 Die attach Process
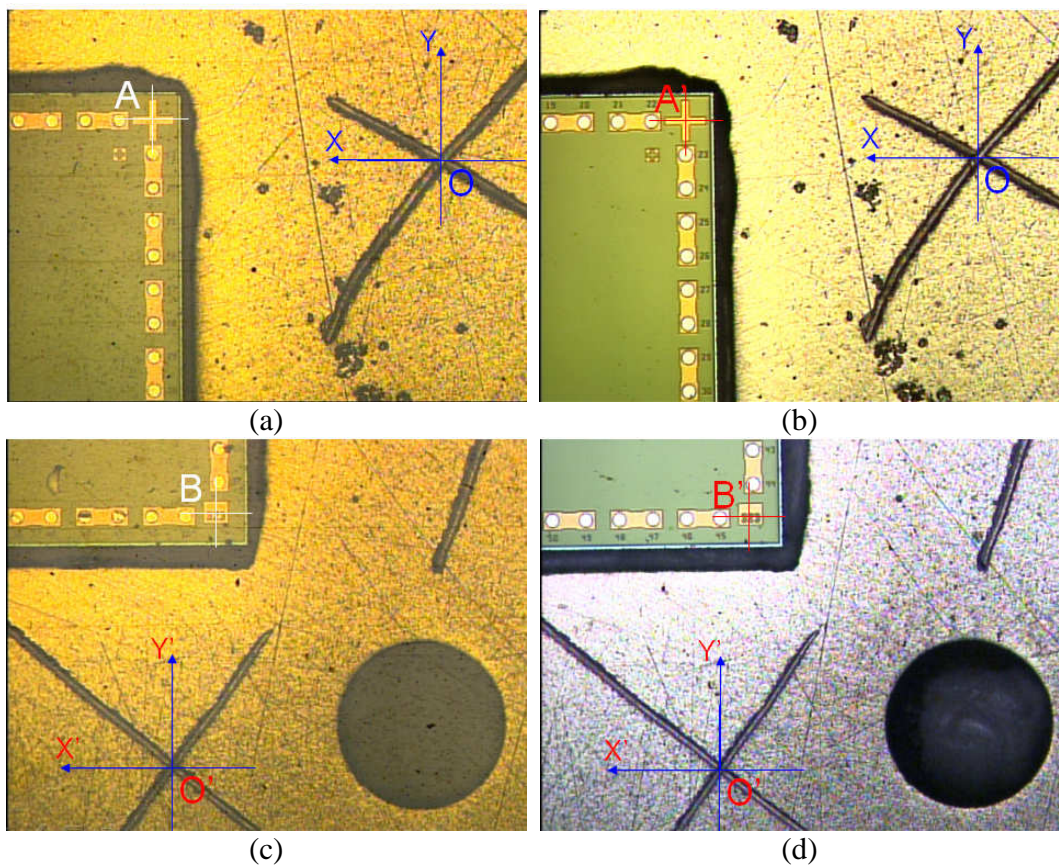
Figure 2.6 Die position experiment: (a) Position A before and after (b) tape removal
(c) Position B before and after (d) tape removal

Table 2.1 Die Position before and after tape removal

Point	Direction	Relative Position from O (O') [mean±standard deviation, mm]	Position Change [um]
A	X	1.775±0.001	-
	Y	0.202±0.003	-
A'	X	1.792±0.004	17
	Y	0.202±0.003	24
B	X	1.556±0.002	-
	Y	0.225±0.002	-
B'	X	1.552±0.003	4
	Y	0.192±0.002	33

2.1.3 Lamination

In the chip-first approach, a thin film structure is built on dies rather than having the chips attached to the finished interconnected structure as in a chip-last approach. To form the first thin film structure used for a dielectric layer, a self-adhesive polyimide film of 50um thickness is laminated over the chips and the substrate as in Figure 2.7. LCP or BCB can also be used as a dielectric layer instead of polyimide. These dry process materials are preferred over wet chemistry materials in the data driven process. In contrast with the aerosol-jet printing, the screen printing application requires an additional polymer mask as shown in Figure 2.6(b). Figure 2.4(c) shows a representative cross section of the dielectric layer lamination.
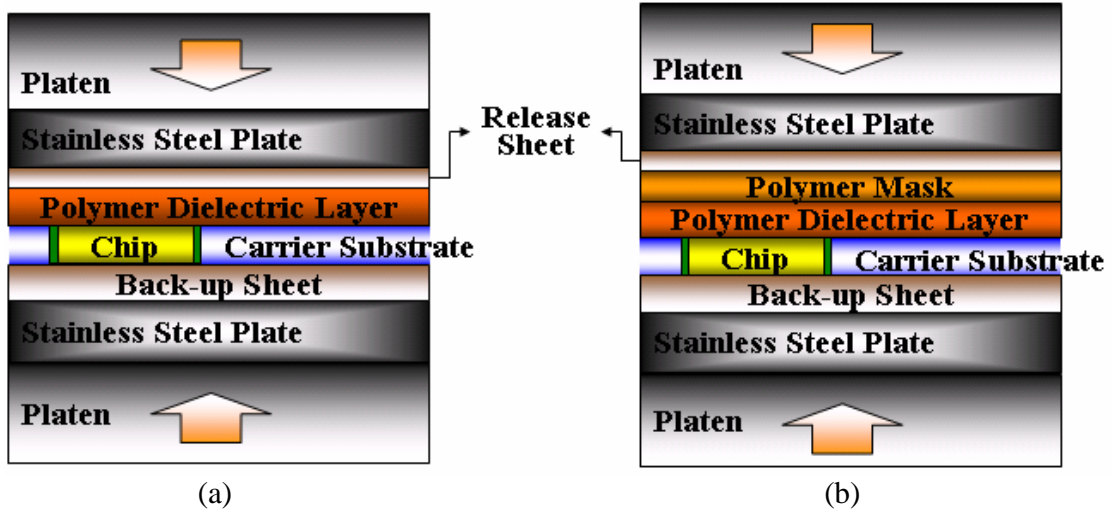
Figure 2.7 Materials stacking for laminating polymer dielectric layer
(a) aerosol-jet printing application (b) screen-printing application

The lamination process parameters are pressure, temperature, and dwell time at the maximum temperature. These parameters are determined by avoiding the primary defects in the lamination process, which are non-filling, non-planarity, and edge delamination as shown in Figure 2.8 (a)-(c). First, the non-filling can be resolved by increasing the viscosity of the adhesive by increasing temperature, whose maximum value is limited by the chip's maximum exposure temperature and time of 350-400℃ for a short period of time and whose minimum value is limited by NPS sintering conditions of 230℃ for 1 hour. Second, the co-planarity can be achieved by using a thick polymer film at the bottom of the substrate at the die attach step and keeping it at the lamination step. For this purpose, 125 um thick polyimide film was used in this experiment. The thick polymer film makes up for the lower level of the chips by thermal deformation. Last but not least, to solve the edge delamination problem, the pressure should be uniformly applied to the whole surface of the chip, and the temperature and the time above melting temperature should be appropriate enough for the adhesive to melt and to bond to the dies

and the dielectric layer. With consideration on these process defects, the lamination process parameters were determined for each dielectric material used in this research as summarized in Table 2.2.

Table 2.2 Lamination Process Parameters

Dielectric Material	Peak Temperature [℃]	Dwell Time [mins]	Pressure [psi]
Kapton KJ	315	20	500
Kapton FN	315	5	300

Figure 2.8(d) shows the good lamination with complete filling, perfect coplanarity, and no edge delamination.
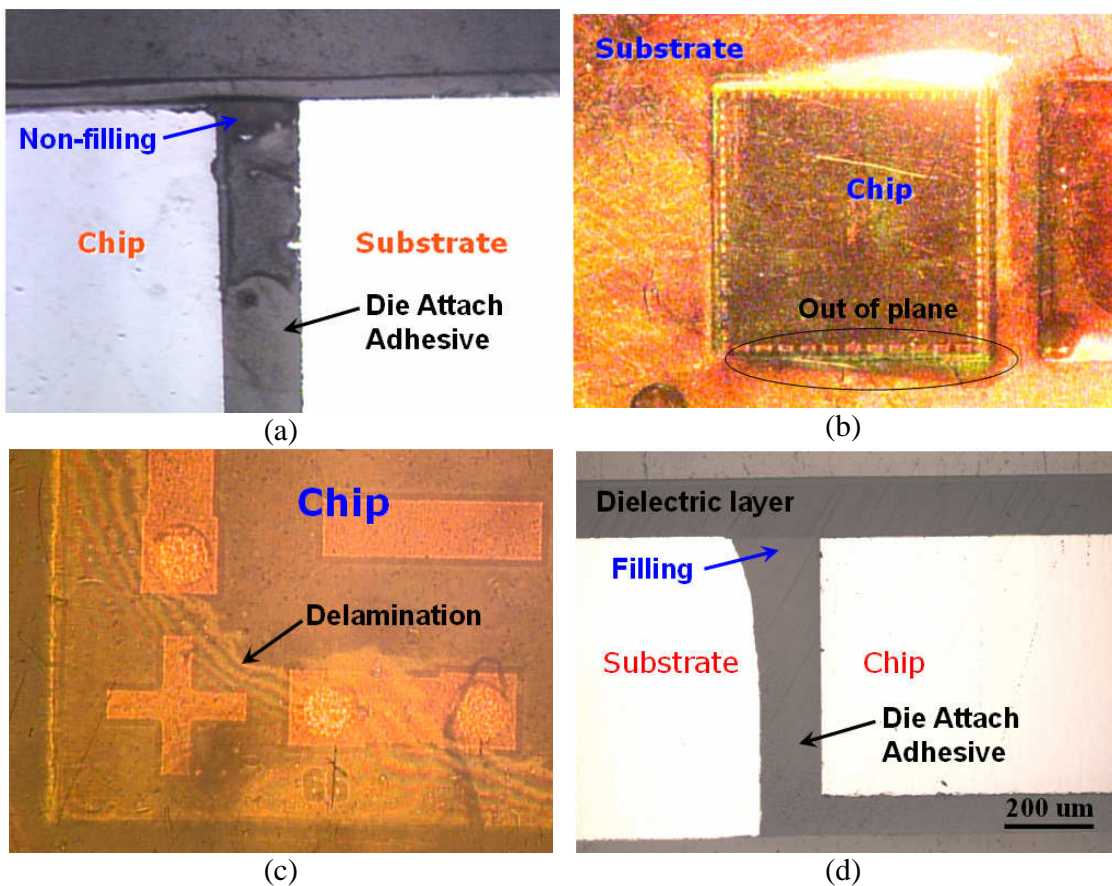
Figure 2.8 Primary defects in the lamination step and good lamination
(a) Non-filling (b) Non-planarity (c) Edge delamination (d) good lamination

2.1.4 Micro-Via Formation

Micro-via formation and circuit patterning are accomplished by using a computer controlled excimer laser ablation technology. In this technology, laser photons directly excite and break the chemical bonds of the solid, causing ejection of material. The excimer laser machine uses KrF that produces a wavelength of 248nm. The primary factors for forming vias by controlling laser intensity are demagnification, number of bursts, fluence (or energy density, transmission of light), and repetition rate (or burst frequency). Demagnification is dependent of a size ratio of via with respect to a mask, but it is also known to affect the laser intensity. A conformal mask made of brass with 500um size square aperture were used for creating 125 um size micro-vias under 4.0 demagnification. The brass mask is nominally 150um thick. The number of bursts is determined as the number to expose the chip pad, which is determined by the fluence and the repetition rate. The flunece can be varied by changing the transmission of light in the eximer laser machine used in this experiment.

To optimize the laser ablation process, design of experiment (DOE) was performed. In this DOE, the repetition rate (burst frequency) and fluence (transmission of light) werre selected as two factors and etch rate as a response. The levels of each factor were chosen as 10Hz and 100Hz for the repetition rate, and 40% and 80% for the fluence under the constant energy mode of 200mJ. DOE analysis results illustrated in Figure 2.9 show that both the two factors are significant because each p-value is less than 0.05. From the main effect plot, fluence looks more dominant to etch rate than repetition rate. However, repetition rate looks more influential in the low flunece level as shown in interaction plot, Figure 2.9(c). Figure 2.10 shows an example of a good via in a polyimide film created by the optimum settings of 200mJ of energy, 80% of fluence (transmission of light), 100Hz of repetition rate, 240 times of bursts, and 4.0

demagnification with 500 um mask aperture size. Table 2.3 summarizes the Micro-via process parameters for dielectric materials used in this research.

Fractional Factorial Fit: etch rate versus fluence, rep rate

Estimated Effects and Coefficients for etch (coded units)

Term	Effect	Coef	SE Coef	T	P
Constant		0.099125	0.001858	53.34	0.000
fluence	0.128750	0.064375	0.001858	34.64	0.000
rep rate	0.017250	0.008625	0.001858	4.64	0.010
fluence*rep rate	-0.012250	-0.006125	0.001858	-3.30	0.030

Significant !

Analysis of Variance for etch (coded units)

Source	DF	Seq SS	Adj SS	Adj MS	F	P
Main Effects	2	0.0337482	0.0337482	0.0168741	610.83	0.000
2-Way Interactions	1	0.0003001	0.0003001	0.0003001	10.86	0.030
Residual Error	4	0.0001105	0.0001105	0.0000276		
Pure Error	4	0.0001105	0.0001105	0.0000276		
Total	7	0.0341589				

(a)

(b)

(c)
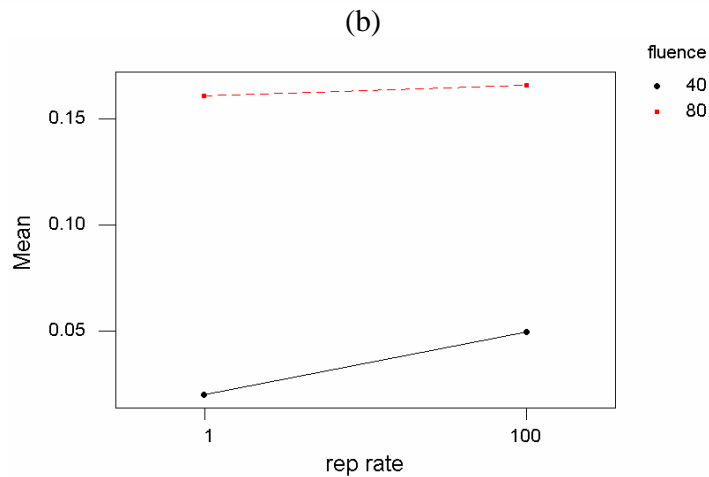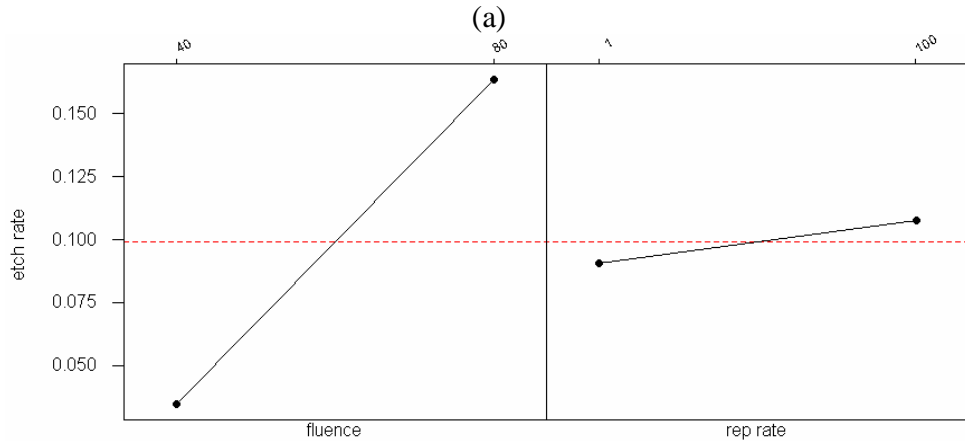
Figure 2.9 Micro-Via DOE analysis results (a) ANOVA (b) Main effect plot (c) Interaction plot
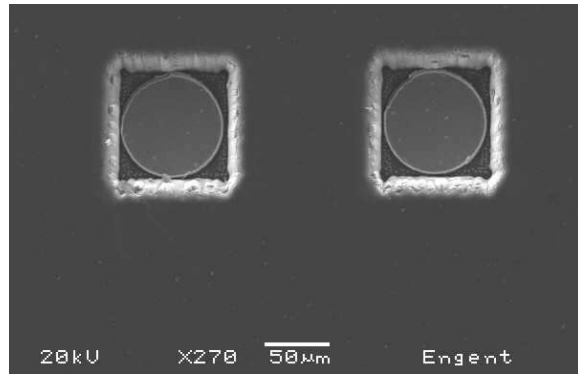
Figure 2.10 Micro Vias created in polyimide layer

Table 2.3 Micro-Via Process Parameters

Dielectric Material		Thickness [um]	Mask aperture size [um]	Demagni-fication	Number of Bursts	Transmission of light [%]
Kapton KJ		50	500 x 500	4	240	80
Kapton FN	HN	25	500 x 500	4	75	97
	Teflon FEP	5	720 x 2000	6	70	97

※Other Parameters: Constant Energy 200mJ, Repetition Rate 100Hz

2.1.5 Screen Printing

The particle size of nano-particle metals is typically in the range of 1 to 100 nm. The nano-particle metal interconnect is due to the sintering behavior of nano-sized metal particles at much lower temperatures than the melting point of their bulk metals, which is called the size effect. The size effect of nano-particle metal results from a considerably high surface area to volume ratio in nano particles (Allen, 1986). However, the sintering behavior is known to be very complicated, where grain boundary diffusion, volume diffusion, surface diffusion, and evaporation and condensation are simultaneously involved. The physics of the nano particle sintering phenomena are not clearly known yet.

The sintering process temperature should be as low as possible since many common organic materials deform at around 200℃.

The silver nano particles were measured as 8nm in diameter with a standard deviation of 0.7nm for 25 samples using TEM as shown in Figure 2.11(a). Figure 2.11(b) shows a SEM picture of the surface morphology of NPS sintered at 230℃ for 1 hour. The particle size of the processed NPS is about 150nm, which is much bigger than the initial particle size, and this result indicates that sintering occurred. As the silver nano particles are sintered at high temperature conditions, solvents in the NPS are evaporated and NPS conductivity slowly increases over time.

(a)   (b)
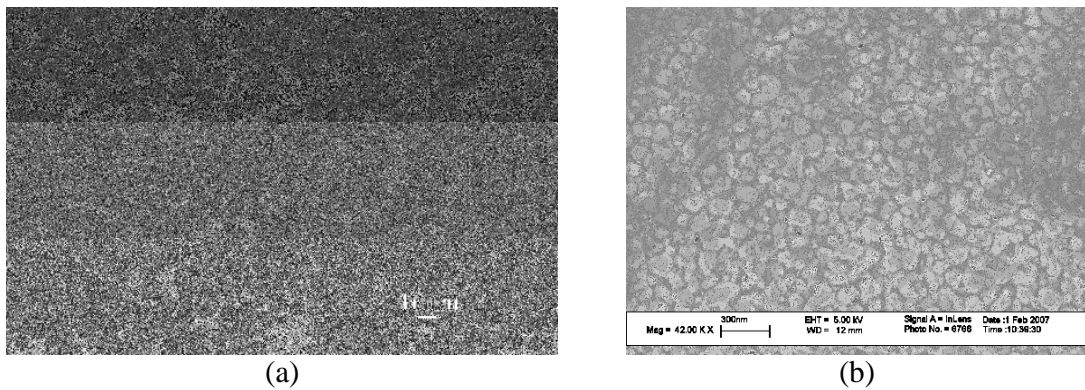
Figure 2.11 Nano-Particle Silver
(a) TEM image before sintering (b) SEM image after sintering

Figure 2.12 shows the screen printing process for NPS deposition. The NPS drops on the substrate and micro-vias are squeezed using a squeeze blade. All the materials with NPS coating are put into a convection oven, which is already pre-heated at 230C. After 1 hr sintering, the polymer mask layer is peeled off and the electrical pattern is formed on the substrate and the micro-vias with NPS film as shown in Figure 2.12(c).
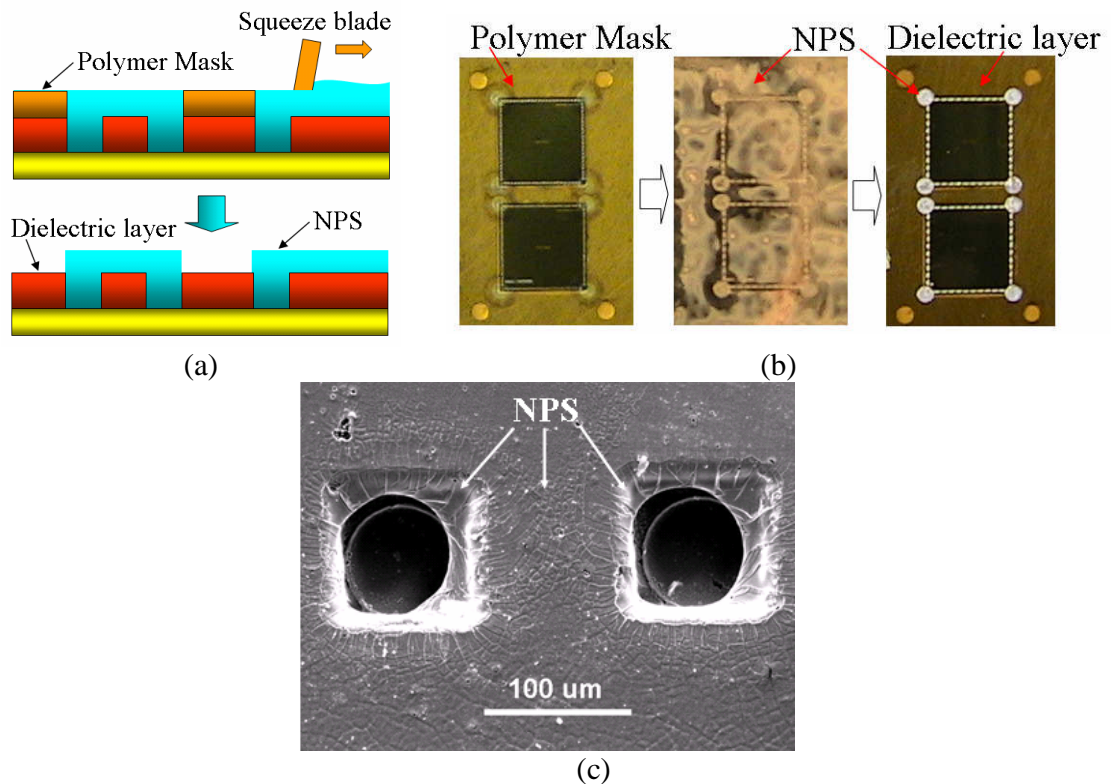
Figure 2.12 NPS Screen Printing (a) schematic diagram (b) photographs of screen

printing (c) Micro-vias after NPS deposition

2.1.6 Aerosol-jet Printing

To make micro sized electrical circuits without using the conventional lithographic process, aerosol-jet printing technology has been developed (Colvin 2005). The aerosol-jet printing process, which is also called Maskless Mesoscale Material Deposition (M3D), consists of three basic steps: aerosolization (transport), deposition, and heat treatment of the deposition. In the aerosolization step, as the name suggests, aerosols are created, and they are entrained in an air stream as schematically shown in Figure 2.13(a). The entrained aerosols pass through a heating element that heats the air stream, and they reach a collector in which the air flow is focused to a tight point for deposition. The focused air is deposited on a substrate by traveling through a nozzle tip. The aerosol droplets are impacted on the substrate sub-sonically. Finally, by heating the

deposition, the nano particles are sintered and bonded to the substrate, forming electrical paths as in Figure 2.13(b). Figure 2.13(c)-(e) shows the microscopic view on some of the electrical features formed by aerosol-jet printing technology.

In the aerosol-jet printing process, the technique for making aerosols depends on the viscosity of the material. Thus, the viscosity of the deposited material should be determined first. Materials with a viscosity of less than 10cP can be atomized with an ultrasonic atomizer, while those with a higher viscosity up to 1000cP could be atomized with a pneumatic atomizer. Depending on the application, the viscosity of the fluids may be adjusted using solvents.
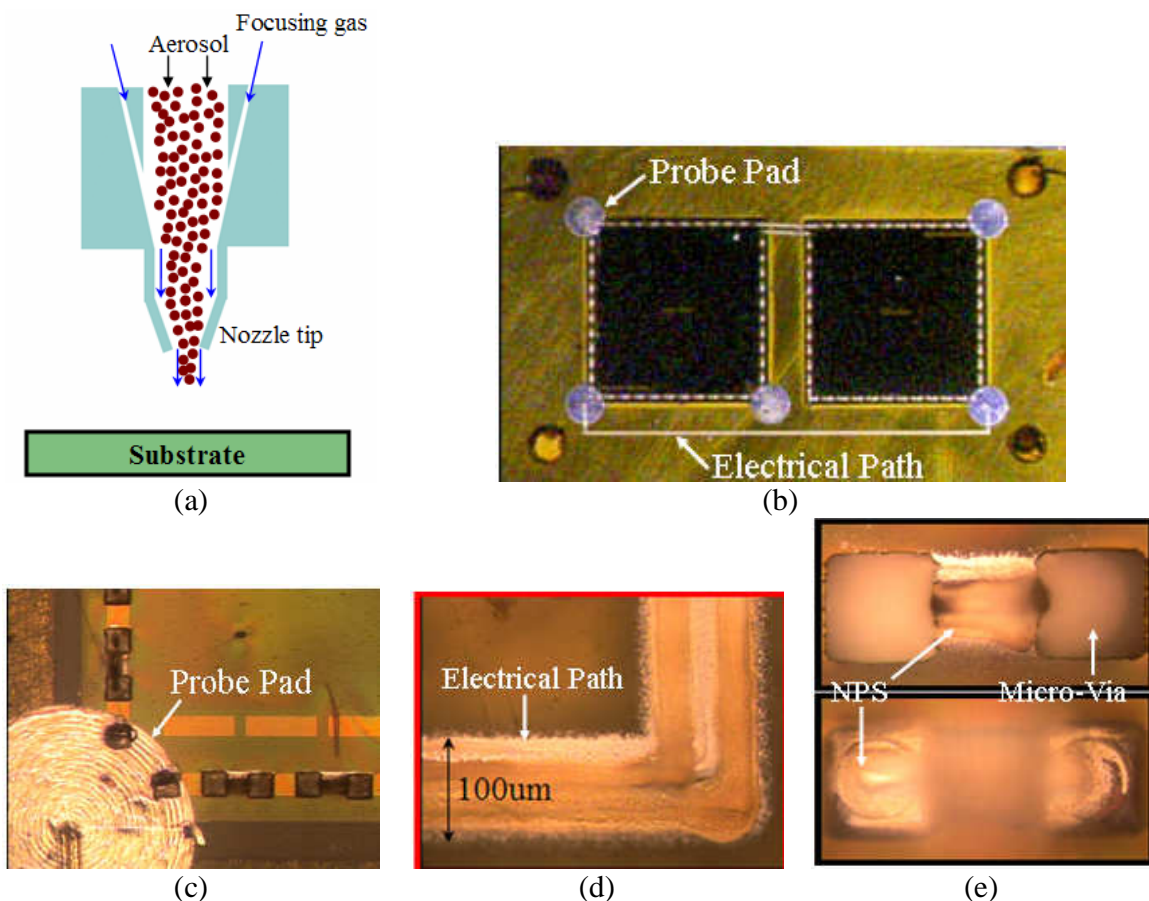
Figure 2.13 Aerosol-jet printing technology
(a) Schematic diagram (b) Electrical paths formed using M3D (c) Magnification on Probe Pad Printing (d) Electrical Path (e) Micro-Vias

2.1.7 Multilayer Packaging

By repeating the unit assembly process described in Figure 2.2, a multilayer package prototype can be constructed as shown in Figure 2.15. This packaging approach for constructing multilayer packages has many advantages over the conventional techniques from the assembly perspective. The packaging approach is data driven and a dry process. It does not require any photo masks for circuit patterning; this reduces packaging turn-around time from months to days. Also, it is not as limited by substrate composition and morphology, eliminates the need for special chip processing such as flip chip solder bumps, and it permits the use of any chip technology and any chip supplier allowing mixed devices. The embedded-active process with NPS avoids the extreme processing conditions required for standard IC fabrication, such as wet chemistry processing and vacuum sputtering. In addition, the NPS is sintered at polymer-compatible temperatures as low as 230℃. These results represent an important step to a system packaging characterized by high density, low cost, and data-driven fabrication for rapid package prototyping.

(a)   (b)

(c)   (d)
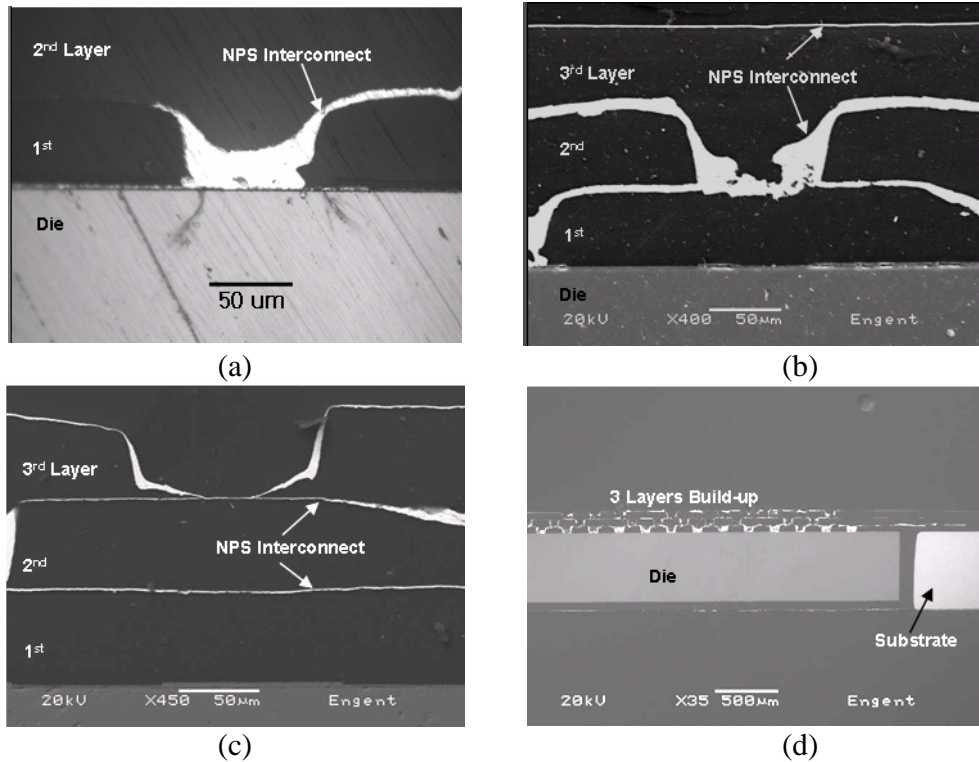
Figure 2.14 Cross sections of a three layer package
(a) 1st layer interconnect (b) 2nd layer interconnect (c) 3rd layer interconnect (d)
overall cross section view

2.1.8 Summary

Rapid package prototyping technology that combines a chip-first approach and a data-driven process has been developed. In this packaging technology, the conventional wet chemical process that influences process complexity and manufacturing lead time has been changed to a dry, data-driven process, resulting in potentially reducing packaging turn-around time from months to days. The rapid package prototyping technology will allow package designers to rapidly and less expensively make tangible prototypes of their designs so that they have excellent visual aids for communicating design concepts with co-workers or customers.

2.2 Nano-Particle Metals (NPM)

The size of metal nano particles typically is in the range of 1 to 100 nm (Fuller, 2002). Due to the small size of nano particles, it has been found that they have much lower melting or sintering temperatures compared to their bulk materials (Allen 1986, Buffat 1976). As cited in Figure 2.16, the melting temperature of gold nano particles depends on particle size. Gold particles with a diameter of 20 Å are predicted to melt at a temperature of 600K (327℃), while bulk gold melts at 1337K (1064℃). Also, nano-particle silver sinters at around 230℃, while the melting point of pure bulk silver is 961℃.

The lower melting point results from a high surface area to volume ratio in nano particles, which makes it possible to form bonds between neighboring particles at lower temperatures due to high surface energy.
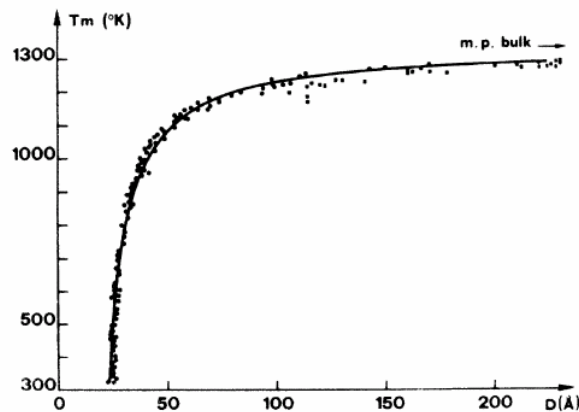
Figure 2.15 Size effect of Au nano particle on melting temperature
(Source: Buffat, 1976)

The development of a fast and convenient fabrication technique to create conductive lines has been a focus for conductive inks. In the research concerning conductive inks, metallic nano-particle suspensions gained significant interest in recent years due to their high conductivity and room temperature operation. Among the metals,

silver and gold nano particles are widely used in the studies of conductive inks due to their high conductivity, lower oxidation rates, and thermal stability. Huang (2003) developed plastic-compatible nano-particle gold materials, which can be sintered at 150°C for 30 min, with very small particle size of 1.5 nm for flexible electronics application. Fuller (2002) used silver and gold nano particles as structural materials to demonstrate how to build a 3-D MEMS device using inkjet printing technology. Lee (2005) synthesized silver nano particles by a chemical reduction method using solvents currently used in commercial color inks without using toxic substances such as toluene to make environmentally friendly inks. Szczech (2004) reported the resistivities of nano-particle gold and nano-particle silver after sintering at 300°C for 15 min as $10 \mu \Omega \cdot cm$ and $35 \mu \Omega \cdot cm$, respectively. Okada (2006) found low resisitivity nano-particle silver of 2 $\mu \Omega \cdot cm$ processed at 300°C for 30 min, which is comparable to 1.59 $\mu \Omega \cdot cm$ of bulk silver (Serway 1998). The larger resistivity of nano particle metal film than that of bulk material might be due to the porosities inside the nano-particle metal film. Figure 2.17 shows an example of the porosities for the nano-particle silver film. The pores in this figure occupy about 7.9% of the whole cross-section surface. These porosities could be the passage of volatile solvent that comes out during the sintering process.

While the nano-particle fabrication research has been in progress, characterization and performance of the nano-particle materials has not been adequately proven yet as an electronics packaging interconnect material. Open problems include resistivity, sintering behaviors, adhesion, leakage current, frequency response, and reliability performance. Specially, adhesion mechanisms of nano- particle metals are very important for the electronics packaging application, but these mechanisms have not been identified yet.
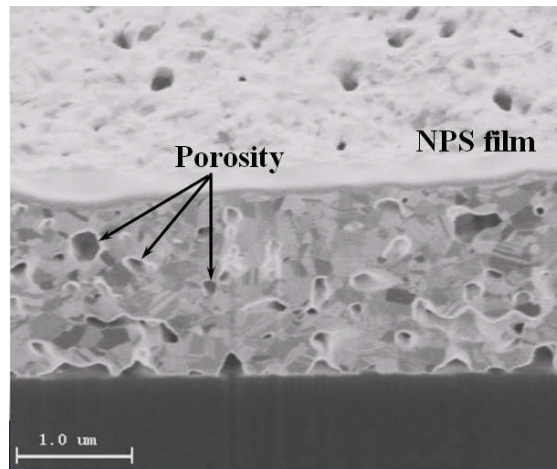
Figure 2.16 Cross section sample of porosities inside NPS film
(Data from NPS manufacturer)

2.3 Nano-Particle Silver (NPS) Adhesion

Nano-particle silver paste or ink (NPS) looks very similar to thick film silver paste except for its particles. While the silver nano particle size is of the order of a nano meter, the thick film silver paste has silver powder sizes at the micro meter level. The thick film silver paste consists of three main components: functional phase, binder, and vehicle. The silver paste functions as a conductor, and thus, silver nano powder is the functional part. It can be bonded to ceramic substrates due to inorganic binders such as glass frit or crystalline oxide powder. The thick film silver paste can be screen-printed on substrates due to the rheological properties given by its vehicle component, which is composed of volatile solvent and nonvolatile resin. To improve wetting on the substrate and dispersion of powder, surfactant can be added into the paste. The silver paste is fired typically at peak temperatures of between 600°C and 1000°C for a period of 20-60 min. During firing, the binder reacts with the ceramic substrate and forms a pillar structure, which provides a mechanical interlock in addition to a chemical bond to the metal film (Vest, 1986).

On the other hand, nano-particle silver consists of silver nano particles, a dispersion agent, and a volatile organic solvent as vehicle. Oda (2005) reported that silver nano particles can be coated with a dispersion agent such as a surfactant to prevent the particles from aggregation at room temperature. At their sintering temperature of around 200℃ for 60 min, heat activates and then removes the dispersion agent from the surface of the particles in order to initiate the connection among particles by atomic movements. It is known that nano-particle silver adhere to some metals and polymers. However, the adhesion mechanisms of nano particle metals including silver have not been identified yet. In particular, the adhesion of nano-particle silver to polymers is concerned with low adhesion strength because most of the processed polymer surface is chemically inert.

Figure 2.18 illustrates examples of NPS adhesion to some electronics packaging materials using an ASTM tape test. NPS film forms a weak adhesion to Kapton FPC, Kapton HN, and aluminum thin film as almost all the NPS film was detached from these materials after attaching and detaching the tape on the NPS film as in Figure 2.18(a)-(c). No detection of NPS detachment from the etched Cu in Figure 2.18(d) means a strong adhesion of NPS to etched Cu.
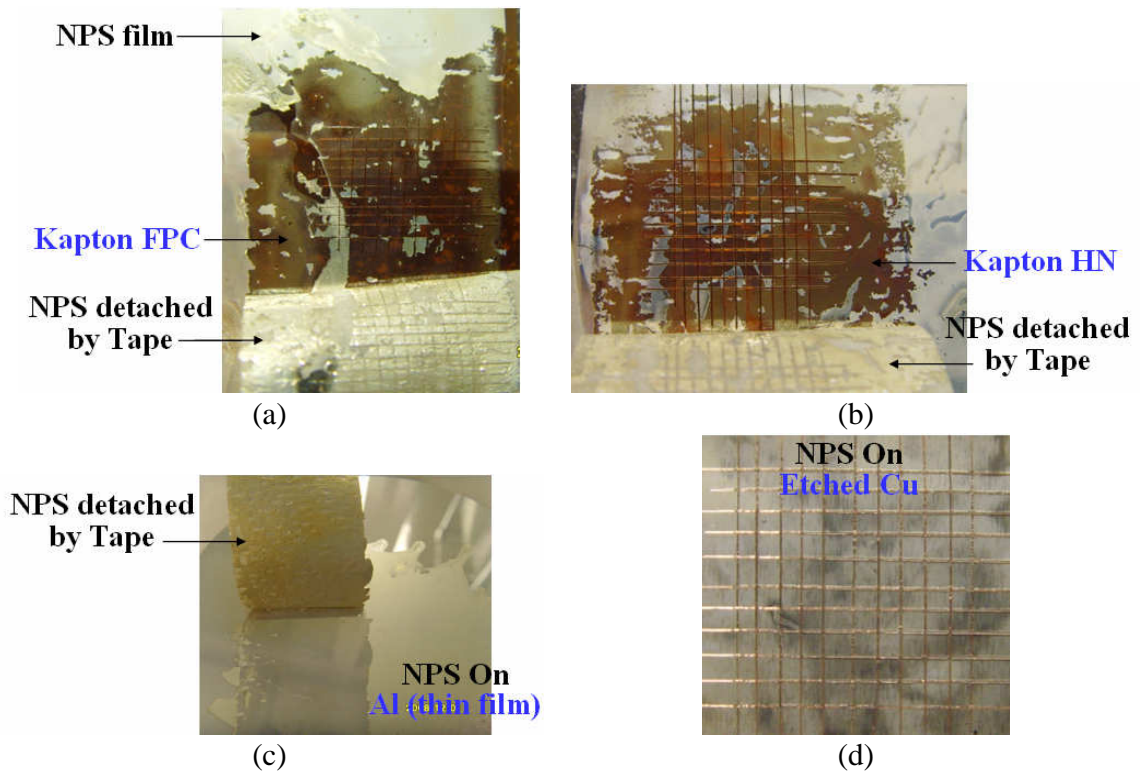
Figure 2.17 ASTM Tape Test on NPS/Electronics Materials

CHAPTER 3

ADHESION MECHANISMS

3.1 General Adhesion Mechanisms

The weakness of the rapid package prototypes with nano-particle silver interconnects has been found to be the weak adhesion of the nano-particle silver to some electronics materials such as Kapton polyimide film and aluminum thin film. Thus, resolving the weak adhesion of the nano-particle silver to substrate materials will be the key issue in developing reliable package prototypes that use nano-particle silver interconnects. In order to improve the adhesion strength of NPS, the adhesion mechanisms of nano-particle silver to substrate materials need to be first known. The adhesion mechanisms of NPS, however, have not been found yet. Therefore, identification of NPS adhesion mechanisms is necessary as an approach to NPS adhesion improvement. In order to identify the NPS adhesion mechanisms, the adhesion mechanisms of general bonding methods were studied in this chapter. Adhesion between two different materials is a complicated phenomenon, and it is based on physical, mechanical, electrostatic, diffusion, and chemical mechanisms.

3.1.1 Physical Adsorption

The well known wetting phenomenon is closely related to physical adsorption, in which surface forces are due to molecular contact - at distances within 5 Å - between two materials. Physical adsorption is mostly due to van der Waals attraction force. Kinloch (1979, 1980) suggested that physical adsorption is the only adhesion mechanism in many

adhesive joints. Allara (1986) concluded that the van der Waals force is the most common surface force, but Fowkes (1987) mentioned that acid-base interactions may also contribute to adhesion forces. Lee (1991) argued that the van der Waals force is the most important mechanism in achieving adhesion. Good (1992) found that wetting due to van der Waals force can be determined by contact angle measurements. Young and Dupre's equation (Van Oss, 1990) describes the relationship between contact angle and thermodynamic work of adhesion. Therefore, the contribution of physical adsorption to the total work of adhesion could be determined by measuring contact angles and using Young and Dupre's equation, which will be discussed in the next section.

Pressure Sensitive Adhesive

Elastomer-based adhesives are used in coated form on a backing as the adhesives in pressure-sensitive adhesive tapes. When the tape and adherend are brought into contact under no more than finger pressure to form measurable bond strength, the adhesive can be defined as a pressure sensitive adhesive (PSA). The primary feature of PSA in contrast with other adhesives is their ability to deflect or lift the backing on which the adhesive is coated with little applied pressure. This property is known as tack, a viscoelastic property of the adhesive. Tack is the instantaneous wetting, which is related to the physical adsorption mechanism. When a PSA is applied to a substrate, the adhesive is expected to spontaneously spread on the surface with little or no applied pressure just like a liquid. The tape is often allowed to sit on the substrate for a period on the order of a second or more after application. However, when the adhesive is peeled, the adhesive is expected to resist the peeling like a solid, but peeling is done on the order of tenths of a second. Thus, a PSA behaves as a liquid for long time scales (wetting) and as a solid for short timescales (peeling). This behavior is achieved in a viscoelastic material. (Pocius, 2002)

3.1.2 Electrostatic Force

It is very well known that rubbing a balloon made of latex rubber on a wool sweater gives rise to a surface charge on the balloon. The forces between atoms or molecules which bear such a charge are called electrostatic forces. Derjaguin (1955) stated that the electrostatic adhesion mechanism can explain all adhesion phenomena. Huntsberger (1967) found that plastic deformations of adhesive and adherend should be considered in the adhesion analysis. Possart (1988) identified the electrical double layer that is closely related to electrostatic force by using potential contrast scanning electron microscope (SEM). Horn and Smith (1992) verified charge transfer between glass and mica. Dickinson (1994) found that discharge occurred when adhesive was peeled from substrates.

Laser Printing (Laser Printer, Photocopier)

A laser printer uses the electrostatic force for a temporary adhesion. The core component of the printing system is the photoreceptor drum, as shown in Figure 3.1, which is made out of highly photoconductive material. The photoconductive material is discharged by light photons.

The drum is positively charged by a charged roller or a charge corona wire. As the drum revolves, the printer discharges certain points by shining a tiny laser beam across the drum surface, forming negatively charged areas (electrostatic image). Then, the printer coats the drum with positively charged toner, a fine black powder. Since the toner has a positive charge, it sticks to only the negatively discharged areas of the drum surface. Next, a sheet of paper that bears a stronger negative charge, given by the transfer corona wire, than that of the electrostatic image rolls under the drum and pulls the toner powder away. The paper is discharged again by another corona wire immediately after

picking up the toner to keep it from clinging to the drum. Finally, the paper goes through a pair of heated rollers (fuser) that melt the loose toner powder and fuse it with the fibers in the paper. The paper passes through the rollers so quickly that it becomes hot but not dangerously hot.
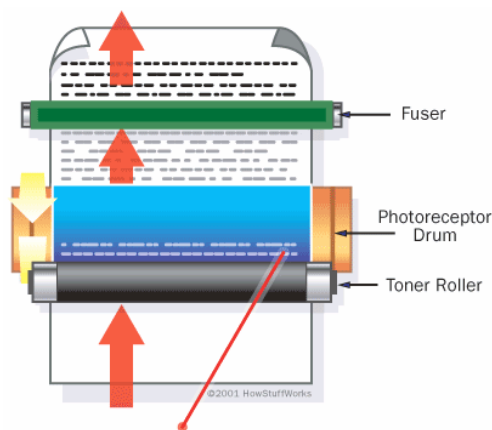
Figure 3.1 Laser printing mechanism
(Source: http://computer.howstuffworks.com/laser-printer3.htm)

3.1.3 Particle Adhesion

Particles in the atmosphere include dusts, metals, fibers, metal oxides, hydrocarbons, pollens, and organic matter. These particles are abundant around us and very easily adhere to surfaces. The adhesion force of such particles is known to be greater than the gravitational force on those particles, as one can demonstrate by inverting the surface with adhered particles. For example, for a 1 um diameter particle, the adhesion force exceeds gravitational force by factors greater than 10^6 (Visser, 1975). The total force of adhesion of micro-sized particles to surfaces can range from 10^{-10} to 10^{-3} N. This force corresponds to a tremendous pressure of up to 100MPa pressure. The total adhesion force on a particle is known to decrease approximately linearly with decreasing particle diameter (Bowling, 1985). Although the forces of adhesion seem to simply decrease with

decreasing particle diameter, the force per unit area increases with decreasing particle size. Therefore, for nano-sized particles, the adhesion force per unit area is expected to be higher than that for micro-sized particles.

In particle adhesion, the attractive interaction forces between a particle and a substrate can be categorized by long and short range forces. Long-range forces are those forces that bring the particle to the surface and establish the adhesion contact area. Van der Waals and electrostatic forces are included in these long-range forces. Short-range forces refer to those forces that can be activated once the adhesion contact area has been established. Various types of chemical bonds such as metallic, ionic, covalent, and hydrogen bonds are included in the short-range forces. However, these chemical interactions with other adherents may not be available because the surfaces of still separate adherents tend to be chemically saturated by contaminating substances (Krupp 1967, Bowling 1985).

Much work on the adhesion forces between a particle and a substrate surface concluded that van der Waals, electrostatic, and capillary adhesion forces are the major contributors to adhesion, while leaving a possibility that chemical bonds at the contact area between the adherents may play an important role. (Krupp, 1967, Bowling, 1985, Ranade, 1987, Donovan, 1993, Kitchener, 1973, Bhattacharya, 1978)

It has been found that electrostatic forces are dominant for particles greater than about 1 um diameter and that van der Waals forces predominate for smaller particles (Chow, 2003). Van der Waals forces refer to forces between molecules having dipoles caused by the spontaneous polarizations of the atoms and molecules in the material. The van der Waals force is large enough for most particles and/or surfaces to be deformed. Thus, the amount of deformation depends on the hardness of the particle and surface, and the adhesion distance between particle and substrate atoms.

3.1.4 Mechanical Interlocking

Adhesives penetrate into any irregularities such as pores, holes and crevices, and they lock mechanically to the adhered surface. This adhesion mechanism, which is called mechanical interlocking, has been understood by many researchers from the perspective of surface roughness effects. Arrowsmith (1970) examined the surface roughness effect of copper on epoxy adhesive. Venables (1984) also investigated the roughness effect of metal oxide films to polymer adhesion. Gent and Lin (1990) developed a mechanical interlocking model to predict the interfacial fracture energy between adhesives and substrates with cylindrical pores. Yao (2000) suggested another mechanical interlocking model to estimate the contribution of mechanical interlocking to the total work of adhesion.

Amalgam restoration

Mercury amalgam has been used for filling tooth cavities utilizing the mechanical interlocking adhesion mechanism, although recently adhesive materials have been used to eliminate the need to remove sound tooth material and to rely on the interfacial forces. In the amalgam restoration, a relatively large 'ink-bottle' pit is formed by drilling out tooth material with an undercut angle of about 5°; then the mercury amalgam paste is forced into the hole, and is cured by shining bright blue light. Mechanical interlocking is the main adhesion mechanism of the amalgam restoration; it ensures that the required service life of seven to ten years is achievable. (Kinloch, 1987)

3.1.5 Chemical Bonding

Chemical bonding is achieved by various mechanisms such as ionic bonds between positive and negative ions, covalent bonds, metallic bonds, coordinate bonds,

and hydrogen bonds. Chemical bonds have large energies of an order of 100 times the energy of physical forces of equivalent physical scale (Eley, 1961). Cantrell (2004) found that the epoxy to aluminum bond was due to hydrogen bonds formed from the OH groups on the oxidized aluminum surface and the epoxy groups of the adhesive. Many researchers including Grivas (1986), Parent (1988), and Lee (1999) investigated the intermetallic formation between lead or lead-free solders and copper. The covalent bonding effect obtained by adding silane coupling agent on the glass-fiber composite has been examined by several researchers such as Shyu (1985), Park (2000), Bikiaris (2001), and Feller (2004). It has been known, however, that identifying each chemical bond across an interface is almost impossible because the interface layer is extremely thin and chemical bonding is very complicated. Instead, experimentally estimating the contribution of the whole set of chemical bonds to the interfacial fracture toughness tends to be the preferred approach.

Rubber to Brass bonding

The bond between brass (70wt% copper and 30wt% zinc) and rubber is achieved during vulcanization of the rubber. Brass is laid on top of unvulcanized rubber and they are heated in a press with the addition of sulfur. During heating, various reactions are believed to take place at the same time inside the rubber and on the interface between rubber and brass. Above all, the cross-linking reaction of rubber and the bonding between rubber and brass take place, resulting in adhesion. The interfacial layer between rubber and brass is about 100nm thick. This layer is double, with a zinc oxide layer containing a small quantity of zinc sulfide on the metal side and a cuprous sulfide layer on the rubber side. Cuprous sulfide on the adhesive interface is a nonstoichiometric compound, $Cu_{1.97}S$, which contains more sulfur than Cu_2S. Sulfur exists in the form of a cross-link, -C-S-C-,

in the interfacial layer. Therefore, adhesion takes place between the rubber surface and the brass surface covered with a thin layer of cuprous sulfide formed by chemical bonding. (Yosomiya, 1989)

3.1.6 Diffusion

Diffusion refers to a net transport of molecules due to concentration difference. The result of diffusion is a gradual mixing of material by random molecular motion from a higher concentration region to a lower concentration region. Without any external net forces and under uniform temperature, the diffusion process will eventually result in complete mixing or a state of equilibrium.

Molecular diffusion is typically described using Fick's laws of diffusion as in Equation (3.1). This well-known diffusivity equation indicates that the velocity of diffusion at the bonding interface is influenced by the diffusion coefficients of the interface materials, their activation energies, and the temperature.

$$D = D_o e^{(-Q/RT)} \tag{3.1}$$

where D is diffusivity, Q is activation energy, T is temperature, D_0 and R are constants.

The activation energy of metal atoms is different for the different types of diffusion. Generally, diffusion is classified into body (or bulk) diffusion and short-circuit diffusion, which includes boundary diffusion, dislocation diffusion and surface diffusion. The body diffusion is much slower than the short-circuit diffusion.

Polymer to polymer adhesion generally occurs through the inter-diffusion of molecules in the adhesive and the adherend. They must be chemically compatible with each other in terms of diffusion and miscibility for the inter-diffusion to take place. Voyutskii (1963) suggested that polymer adhesion is due to the mutual diffusion of polymer molecules across the interface. Vasenin (1969) found that the adhesion for

polyisobutylene was a function of temperature and time, following Fick's 2nd law. De Gennes (1974) described the diffusion of a mobile polymer chain through a net of impenetrable and immobile obstacles using the Reptation model, which is a widely used concept of polymer motion.

Diffusion Bonding

Diffusion bonding is a joining process that uses the general assumption that all metals bond if thoroughly cleaned surfaces are brought together within the range of interatomic forces. Once two fresh metal surfaces come into contact, interdiffusion occurs, resulting in bond formation. This process is achieved using an applied pressure at an elevated temperature usually in the range of 0.5 – 0.8 Tm, where Tm is the absolute melting point of the material being joined.

Solid-state reaction (SSR) and transient liquid phase diffusion bonding (TLP) are the two main variants of diffusion bonding. In the SSR, disruption of the surface oxide or films on the metal surface allows intimate metallic contact and hence bonding. Many studies have been done to remove the oxide films and to complete the diffusion bonding. While some metals such as copper, titanium and steel dissolve the surface oxides into the bulk of the metal or decompose at the bonding temperature, a chemically stable oxide layer such as aluminum oxide needs to be ruptured by imposing a substantial amount of plastic deformation of 40% at the minimum.

In the TLP, a liquid layer is formed during the bonding process and then, as a consequence of continued interdiffusion at the bonding temperature, isothermal solidification occurs to generate bonding (Shirzadi, 2001). The formation of the liquid phase generally is achieved by inserting an interlayer with suitable composition, which has a lower melting point than the alloy being joined. A zinc interlayer for aluminum

alloys corresponds to this case. The liquid phase can also be formed using a eutectic composition that locally lowers the melting point as in the case of copper interlayer with aluminum alloys. While the interlayer in brazing solidifies only when the bond is cooled, the liquid phase in TLP subsequently solidifies isothermally as a consequence of continued diffusion at the constant bonding temperature.

Cold Welding

Bonding can be achieved even at room temperature when deformation causes fresh metal surfaces to be exposed and the deformation is high enough to establish contact between the two fresh surfaces. This technique is called cold welding. In cold welding, external pressure produces cracks on the surface layer or the oxide layer on the metal surface and extrudes virgin metals through the cracks in order to form metallic bonding (Manesh, 2004). Since rolling is capable of producing high pressure, cold roll bonding (CRB) is one of the best methods for using the cold welding mechanism, which is also referred to cold pressure welding by rolling, bonding by cold rolling, clad sheet by rolling, and cold roll bonding. The bonding strength of CRB is known to be affected by various factors such as surface preparation conditions, the amount of deformation, storage time between surface preparation and the bonding, and the time of bonding (Li, 2008, Zhang, 1996).

There are many theories on the bonding mechanism of cold welding. Thin membrane theory states that the material's weldability is not dependent on the materials properties, but on the state to be welded. Recrystallization theory suggests that the cold welding process is the course of recrystallization. Dislocation theory says that the plastic deformation of metals can cause dislocations to move to the metal surface and to achieve bonding. Diffusion theory holds that cold welding is due to atomic diffusion. However,

energy theory is against the diffusion theory by saying that atomic energy rather than atomic diffusion is required in the bonding. Yuntao (2003) insists that in a hardly soluble system such as Ag-Ni and Al-Pb, the bonding mechanism of cold welding is the mechanical bonding force and metal atomic linkage (metallic bonding), but not atomic diffusion or super-saturated solid solution, because no compounds or solid solutions appear on the interface.

Wire bonding

The traditional wire bonding process has been widely used as an interconnection method in the microelectronic packaging industry for many years. Thermosonic bonding technology, one of the widely used wire bonding technologies, has some known bonding steps as follows:

First, the wire balls and the metal pads of the chip or the substrate are brought into contact under the force on the capillary, generating some initial deformation. However, there is no adhesion in this step due to the presence of surface oxides. Ultrasonic energy is propagated to the contact surfaces through transducer and capillary and removes the oxide layers on the surfaces by vibrating the capillary with high frequency. The ultrasonic energy also forces the exposed fresh surfaces of the bonding material together with additional thermal energy applied from a heat source. At this step, atomic diffusion occurs and causes micro-welds at the bonding interface, forming bonding strength (Jeng, 2005).

Li (2008) suggests that the diffusion mechanism at the beginning of ultrasonic bonding is surface diffusion and that as the bonding evolves, dislocation diffusion becomes dominant. He also suggests that the ultrasonic bonding is completed at relatively low temperature and so is different from a thermal melting mechanism.

Soldering, Brazing, and Welding

The soldering and brazing processes are different from welding in that they have lower melting points than the metals to be joined. Soldering and brazing are distinguished by the process temperature of below 800°F for soldering and above 800°F for brazing, resulting in different adhesion strength and service temperature. While soldering joins metals using a metallic alloy filler material such as Pb-Sn and Sn-Ag-Cu solder, brazing uses brazing metals such as brazing brass (60% Cu, 40%Zn), nickel silver and copper silicon.

Both soldering and brazing processes require heat to melt and to spread the filler so that the molten filler can wet the base metals by alloying and diffusion. Fluxes are used to promote wetting by removing stubborn oxide films and other surface contaminants.

Solder adhesion depends more on its ability to be interlocked into minute surface irregularities than on alloying or diffusion. The molten solder wets the joint surfaces and is drawn, by surface tension, into minute fissures and capillary openings. Thus, in order for molten filler metal to spread well, it is more important to get the work surfaces clean thoroughly.

Whereas diffusion is of secondary importance in soldering, in the brazing process, bonding conditions are set up so that a large amount of diffusion can take place in order to strengthen and improve the bond.

Welding melts the base metals to be joined and combines them into one piece by solidification during cooling down. The fused joint may be achieved either by simply fusing metal surfaces together or by introducing additional molten metal of similar composition to form a metallic bond. Fluxes can be also used in welding to promote metallurgical processes to join metallic surfaces. (Baxter, 1994)

3.1.7 Paint Adhesion and others

Paint Adhesion

Paint usually consists of four basic components: Pigments, binder, liquid, and additives. Pigments provide color, binder plays a role of binding the pigments together and provides adhesion to the substrate, liquid functions as a carrier to make it possible to apply the pigment and the binder to the surface to be painted, and additives provide additional paint properties such as good flow and leveling.

When the paint coating is applied on the substrate, particles of pigment and binder are dispersed in water. As the water evaporates, the particles come closer together. At the last trace of water evaporation, capillary force will draw the binder and the pigment particles together. In the case of polymer pigments, the polymers start to interdiffuse and coalesce into a continuous film above the minimum film-forming temperature (MFFT) of the paint. In addition, the paint coating is believed to be mechanically interlocked into the pores or irregularities of the substrate because sanding or etching the substrate surface enhance the paint adhesion. Also, electrostatic force increases the paint adhesion in the electrostatic painting technique. The paint gun applies a high-voltage electrostatic charge to the paint particles as they exit the gun. These charged particles are then drawn to the object being painted, which has been grounded.

Instant Adhesive (Super Glue, Cyanoacrylate adhesive)

Instant adhesive sets within seconds. This quick reaction is due to anionic polymerization, as described in Figure 3.2, which occurs when a substance having anions, such as water (H·OH), methanol (CH3OH), or caustic soda (NaOH), causes polymerization. The anionic polymerization is initiated by anion (OH) addition to the carbon-carbon double bond of the monomer as shown in Figure A. The polymerization

propagates by undergoing repeated addition of monomer units and then terminates. (Brinkmann, 2002)
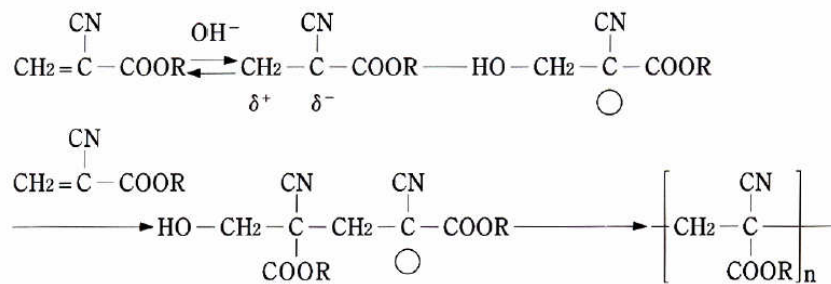
Figure 3.2 Anion Polymerization

Chalk, Pencil

The drawing or writing principle of blackboard chalk is to leave particles on the board surface. The chalk is often supplied in sticks of compressed powder that is made from calcium sulfate. As it is rubbed on a rough board surface, it readily falls apart leaving particles that stick loosely to the surface. The same principle is applied to pencil that is made of graphite. Thus, pencil erasers pick up graphite particles from a paper. Since the molecules in erasers are stickier than those of the paper, the graphite sticks to the eraser preferentially over the paper when the eraser is rubbed onto the pencil mark. Some hard erasers damage the top layer of the paper and remove it as well.

Adsorption

While adsorption refers to the phenomena on a surface, absorption is a physical or chemical phenomenon in which atoms, molecules, or ions enter the bulk phase of another substance (gas, liquid or solid). Thus, adsorption will not be considered in the interfacial adhesion study, in which the surface phenomena are dealt with.

Inkjet Printing (Inkjet Printer, Ink on Paper, Ballpoint Pen)

The printing or writing principle of ink-based tools, such as inkjet printers, ballpoint pens, and regular inks, is absorption of inks into the paper. In order to improve print quality, inkjet printer manufacturers try to make the ink stay in a tight, symmetrical dot. This is because if the ink is absorbed too far into the paper, the dot will begin to feather. As a result, high-quality inkjet paper is typically coated with a waxy film, resulting in low absorption of the ink. The surface roughness of paper also affects the print quality, especially the brightness. While a rough paper scatters light in several directions, a smooth paper reflects more of the light back in the same direction. This makes the paper and in turn any images on the paper appear brighter.

3.2 Sintering Mechanisms

It turns out that the melting temperature of materials can be dramatically reduced by decreasing the size of the material, which is called size effect. It has been found that the sintering process is a primary mechanism of the low melting point of the small particles. Surface diffusion, volume diffusion, grain boundary diffusion, and evaporation and condensation can be the four mechanisms in sintering process. However, they are simultaneously involved in the sintering behavior, which is hence very complicated, and therefore the physical behavior of the sintering mechanism is not completely understood.

Figure 3.3 illustrates a Cu-Ni two-sphere system forming a neck between two dissimilar materials when subjected to sintering. Sintering can be categorized into three processes, adhesion, densification, and grain growth process. The four major mechanisms aforementioned are simultaneously involved in each process (Shimosaka, 2003, Kingergy, 1955).
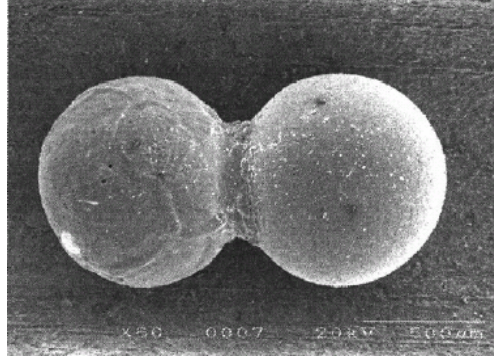
Figure 3.3 Sintering between Cu and Ni
(Source: Shimosaka, 2003)

Adhesion Process

The adhesion process occurs due to the vacancy concentration gradient between the grain surface and the neck. If the neck has a high vacancy concentration and the grain surface has a lower concentration, a substance transfer occurs from the grain surface to the neck while the vacancy diffuses from the neck to the grain surface. The substance transfer mechanisms involved in this process are the surface diffusion and the volume diffusion from the grain surface to the neck, and the evaporation from the grain surface and the condensation on the neck.

Densification Process

The densification process takes place owing to substance migration causing shrinkage. As a result of the adhesion process, the distance between the centers of the two grains decreases. This shrinking behavior is called as the densification process. Two mechanisms are involved in the densification process: the volume diffusion and the grain boundary diffusion from the grain boundary to the neck surface.

Grain Growth Process

The grain growth process occurs due to the surface energy difference between two grains. The substance transfers through the grain boundary from the Ni grain having a greater surface energy to the Cu grain having a smaller surface energy, if the grain-to-grain distance changes as time passes. The growth of the Cu grain is promoted by the energy, defined as the difference in energy between the Cu grain and entire system. Also, the energy difference between the Ni grain and the entire system promotes the substance transfer of the Ni grain, causing shrinkage of the Ni grain.

3.3 Relevant Adhesion Mechanisms to NPS

Adhesion mechanisms of the general bonding methods can be classified into adhesive adhesion and particle adhesion mechanisms as summarized in Figure 3.4. These mechanisms can be narrowed down to more relevant adhesion mechanisms to NPS adhesion by an order of magnitude analysis and considering relevancy to NPS adhesion.

First, the electrostatic force contribution to the total adhesion force (between metal and polymer) is known to be negligible by an order of magnitude comparison. Possart (1988) found that electrostatic work was only 0.171% of the peel strength between aluminum and polyethylene. By considering that about 30% of the peel strength is occupied by interfacial fracture energy, including electrostatic force for copper and Kapton H polyimide composite (Yu, 2002), the electrostatic force can be estimated to be roughly 0.57% (=0.171%/0.3) of the total adhesion force. The fact that the interfacial fracture energy is about 30% of the total fracture energy is supported by Yao's experiments (2000) for aluminum and epoxy bonding using a four-point bending test. Roberts (1977) argued that the electrostatic energy density (10e-5 mJ/m2) is negligible compared to van der Waals energy density (60 mJ/m2) for rubber to glass bonding.

4 4

Therefore, the electrostatic force contribution is negligible and is excluded in this study.

Since the NPS consists of silver nano particles, general particle adhesion mechanisms may work. In the NPS particle adhesion, however, electrostatic force, one of the particle adhesion forces, can be neglected because van der Waals forces predominate for smaller particles than about 1 um diameter (Bowling, 1985, Chow, 2003). Since the silver nano particles (8 nm) are much less than 1um, the van der Waals force could be dominant over the electrostatic force.
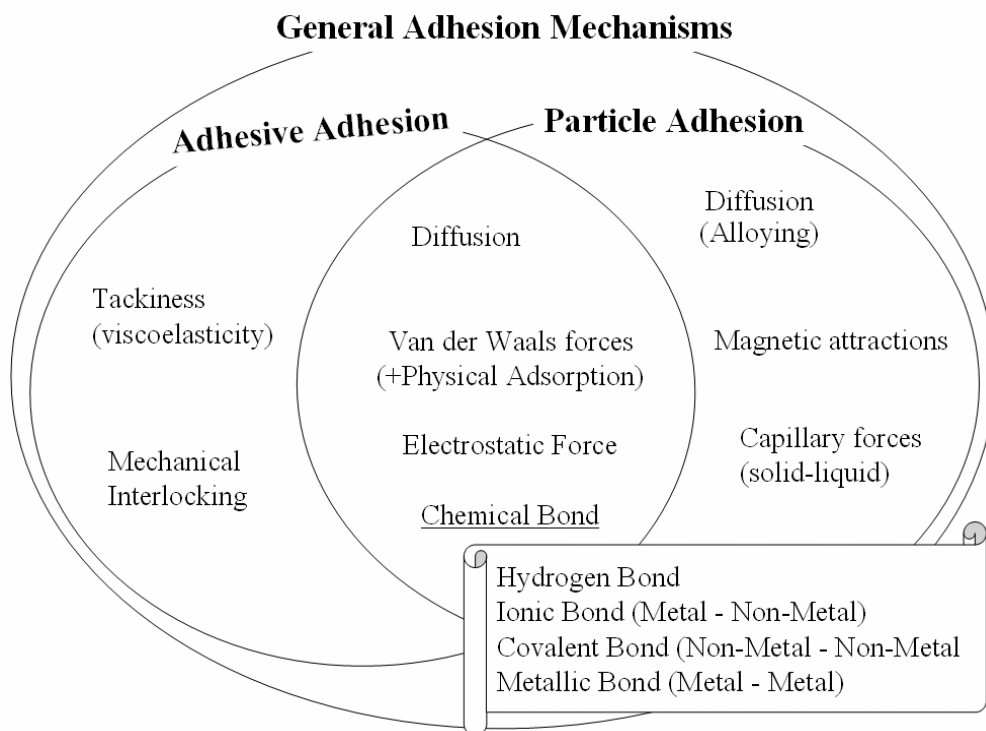
Figure 3.4 Classification of adhesion mechanisms of general bonding methods

Diffusion may exist between NPS and substrates. In the NPS adhesion, only silver to metal diffusion will be considered because of the insufficient evidence for polymer-metal diffusion. Although Wu (1986) examined the migration of sputtered gold particles toward the fastest-diffusion phase, it is not clear that the migrated gold particles contributed to the improvement of adhesion strength. Thus, the metal like silver to

polymer diffusion will not be considered as a significant factor in the NPS adhesion study.

Capillary force is the force between solid and liquid due to the surface tension of the liquid. The magnitude of capillary force is higher than that of van der Waals force or electrostatic force at the same particulate size as shown in Figure 3.5. During the NPS sintering, however, all solvent is assumed to be evaporated, and thus capillary force could be assumed as an insignificant factor in NPS adhesion.
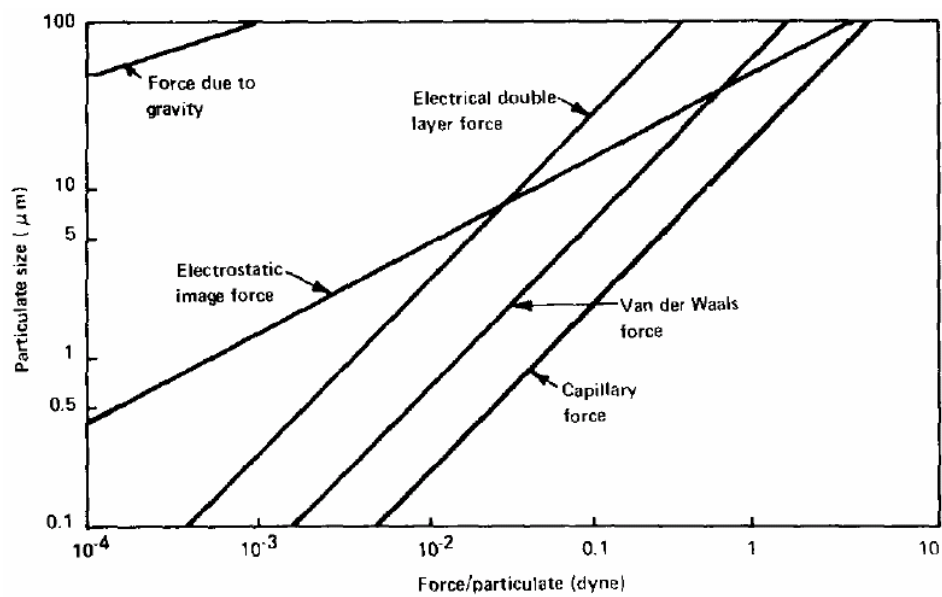
Figure 3.5 Comparison of adhesion forces (source: Bhattacharya, 1978)

In the particle adhesion mechanisms, magnetic attractions between particles and substrate materials can take place due to the intrinsic magnetic moments of particles as opposed to the moving electric charges for magnetic forces in general. These magnetic moments can be quantified by one of the surface energy terms, which is Lifshitz-van der Waals component of surface free energy, γ^{LW}. This surface energy corresponds to the electromagnetic interactions between the contiguous surfaces due to oscillating temporary, permanent or induced dipoles. The magnetic attractions can be incorporated into the physical adsorption mechanism, in which surface forces are due to molecular contact

4 6

between two materials. The physical adsorption, which is mostly due to van der Waals attraction force, can be determined by contact angle measurements. The physical adsorption mechanism also includes the adhesion mechanism of pressure sensitive adhesive, tackiness, which is the instantaneous wetting.

Thus, by considering the magnitude analysis and the relevancy to NPS adhesion, adhesion mechanisms more relevant to NPS are selected as physical adsorption, mechanical interlocking, chemical bonding, van der Waals force, and silver to metal diffusion.

3.4 Plausible Adhesion Factors of NPS

Among the general adhesion mechanisms, more relevant adhesion mechanisms to NPS adhesion have been selected in section 3.3. From these relevant adhesion mechanisms to NPS adhesion, adhesion factors will be extracted and the effect of each adhesion factor on NPS adhesion will be examined

First, van der Waals force from the general particle adhesion mechanism has two adhesion factors: substrate hardness and adhesion distance. The substrate hardness can be measured from indentation methods, and the adhesion distance between particle and substrate atoms will be estimated from the surface energy change. The surface energy change, which is also an adhesion factor of the physical adsorption mechanism, can be calculated from the contact angle measurement using the Young-Dupre equation.

The mechanical interlocking mechanism is mostly understood as the surface roughness effect. When NPS forms a thin film on a substrate, it may fill surface irregularities and locking to the surface just like an adhesive. Chemical bonding depends on bond species and bond density, which covers hydrogen bond, ionic bond, covalent bond, and metallic bond (intermetallic bond). The NPS sticks to polymer substrates selectively, which means that NPS may have any preferable chemical sites in forming

chemical bonds such as covalent bonds to organic substrates. The silver nano particles also adhere to metals as well as polymers, which may be due to metallic bonds.

Finally, diffusion is critically dependent on temperature, which may be regarded as the primary activation energy as in wire bonding. The plausible adhesion factors in the relevant adhesion mechanisms to NPS adhesion are summarized in Table 3.1.

Table 3.1 Plausible Adhesion Factors of NPS

Adhesion Mechanism	Adhesion Factor	Physical Phenomenon
Van der Waals Force	- Substrate Hardness - Adhesion Distance	Particle Adhesion
Physical Adsorption	- Surface Energy Change (Contact Angle)	Adhesive Adhesion
Chemical Bonding	- Bond Species & Density	Hydrogen bond Ionic bond (Metal to non-Metal) Covalent bond (non-Metal to non-Metal) Metallic bond (Metal to Metal)
Mechanical Interlocking	- Surface Roughness	Adhesive Adhesion
Diffusion	- Temperature (Activation energy)	Metal to Metal diffusion

CHAPTER 4

ADHESION EXPERIMENTS

4.1 Introduction

The nano-particle silver (NPS) used in this work was purchased from a commercial source. The silver nano particles have an average diameter of 8 nm based on the TEM measurement, as shown in Figure 4.1. The NPS inks are composed of silver nano particles, a dispersion agent coating on the particles, and a solvent (n-tetradecane). When the sintering temperature of around 200℃ is maintained for 60 min, heat activates and removes the dispersion agent from the surfaces of the particles and the connections between particles initiate.
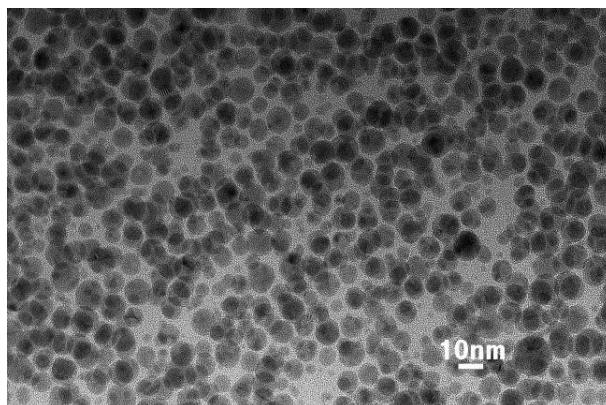
Figure 4.1 TEM image of silver nano particles

Figure 4.2 shows a SEM picture of surface morphology of NPS film that has been thermally treated at 230°C for 1 hr, which is a sintering condition recommended by the manufacturer. Compared to Figure 4.1, the particle size after thermal treatment is more than ten times the initial particle size, which indicates that sintering occurred.
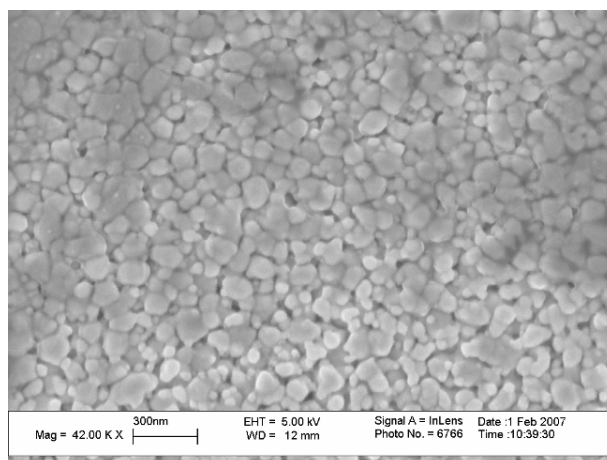
Figure 4.2 SEM image of NPS thermally treated at 230°C for 1 hr

4.2 Experimental Procedure

The adhesion experiments to identify and extract significant adhesion factors follow the experimental procedure in Figure 4.3. First, one of the substrate materials is selected and then the plausible adhesion factors such as substrate hardness, contact angle, and surface roughness will be measured for the substrate material. An adhesion factor can be modified in order to examine the significance of the adhesion factor. For example, Silane coupling agents can be mixed into NPS inks or the sintering temperature can be changed. After cleaning using isoprophyl alcohol as the basic sample surface preparation, NPS inks will be deposited on the substrate and heated in the convection oven at the appropriate temperature and time. Using the ASTM tape test, the adhesion level will be quickly assessed. Finally, adhesion strength will be measured quantitatively using a newly developed adhesion test methods, which will be discussed in detail in Chapter 5.
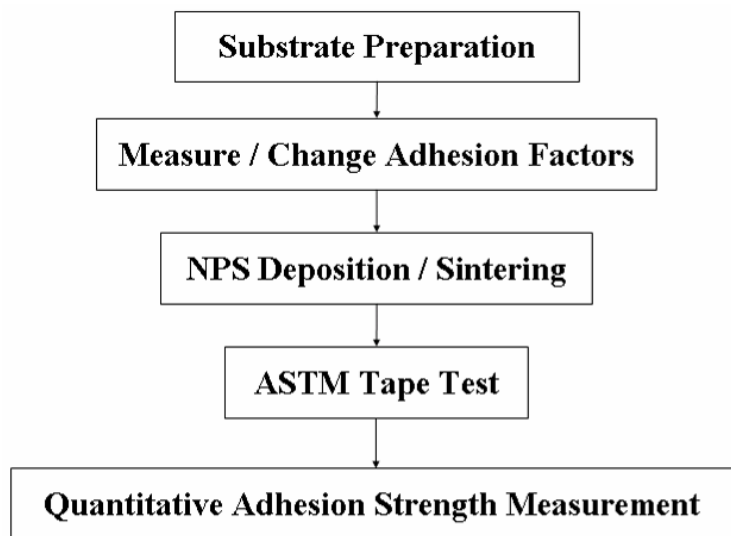
Figure 4.3 Experimental procedure

4.2.1 Thickness Control

In order to control NPS film thickness uniformly across all the samples used in the experiments, one drop of NPS ink, which corresponds to 25.4 mg, will be put on the substrate as in Figure 4.4, and it spreads uniformly across the 50x50 mm area as in Figure 4.5. Eventually, the NPS film thickness after sintering is about 2 um as shown in Figure 4.6.
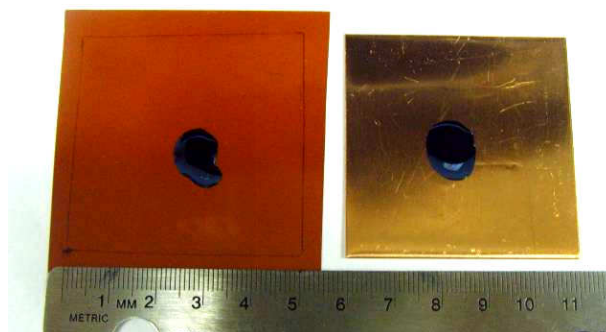
Figure 4.4 One drop of NPS inks on substrates
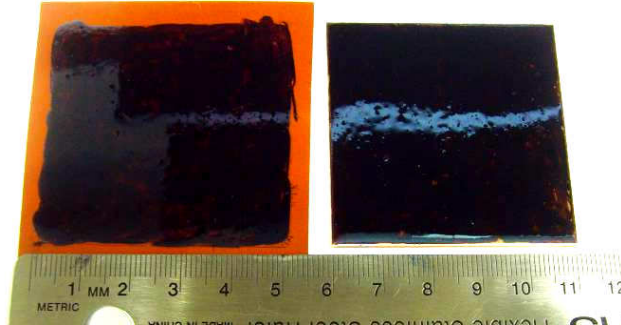
Figure 4.5 50x50 mm^2 coverage of one drop of NPS inks
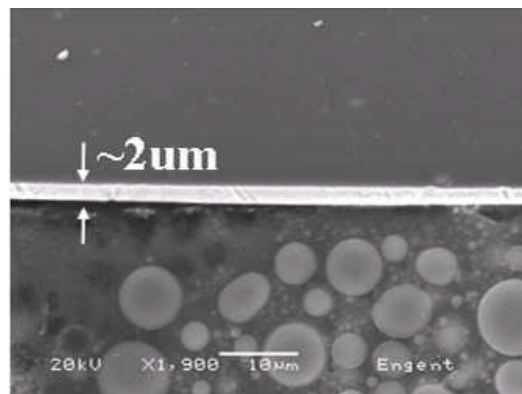
Figure 4.6 SEM image of NPS film thickness

4.2.2 ASTM Tape Test

  To determine how well the selected substrates adhere to NPS, the generally used tape test based on the ASTM standard (ASTM D 3359-08) was performed by applying and removing pressure-sensitive tape over cuts made in the sintered films. The tape test is qualitative, that is it provides only a 'yes or no' decision, but it is simple and moreover it provides rapid assessment of adhesion level. The adhesion level is classified into 6 levels from 0B (more than 65% area removed) to 5B (0% of removal area) according to the standard as cited in Figure 4.7. Examples of the adhesion test results are also displayed in Figure 4.7 by inspecting the grid area for removed coating from the substrate and rating the adhesion. As a suitable tape for this purpose, P-tape is used in accordance with the

standard. The tape is about 140um thickness and it has typical adhesion strength to steel of 57 N/mm.

CLASSIFICATION	PERCENT AREA REMOVED	SURFACE OF CROSS-CUT AREA FROM WHICH FLAKING HAS OCCURRED FOR SIX PARALLEL CUTS AND ADHESION RANGE BY PERCENT
5B	0 %	
4B	<5%	
3B	5-15%	
2B	15-35%	
1B	35-65%	
0B	>65%	

FIG. 1 Classification of Adhesion Test Results
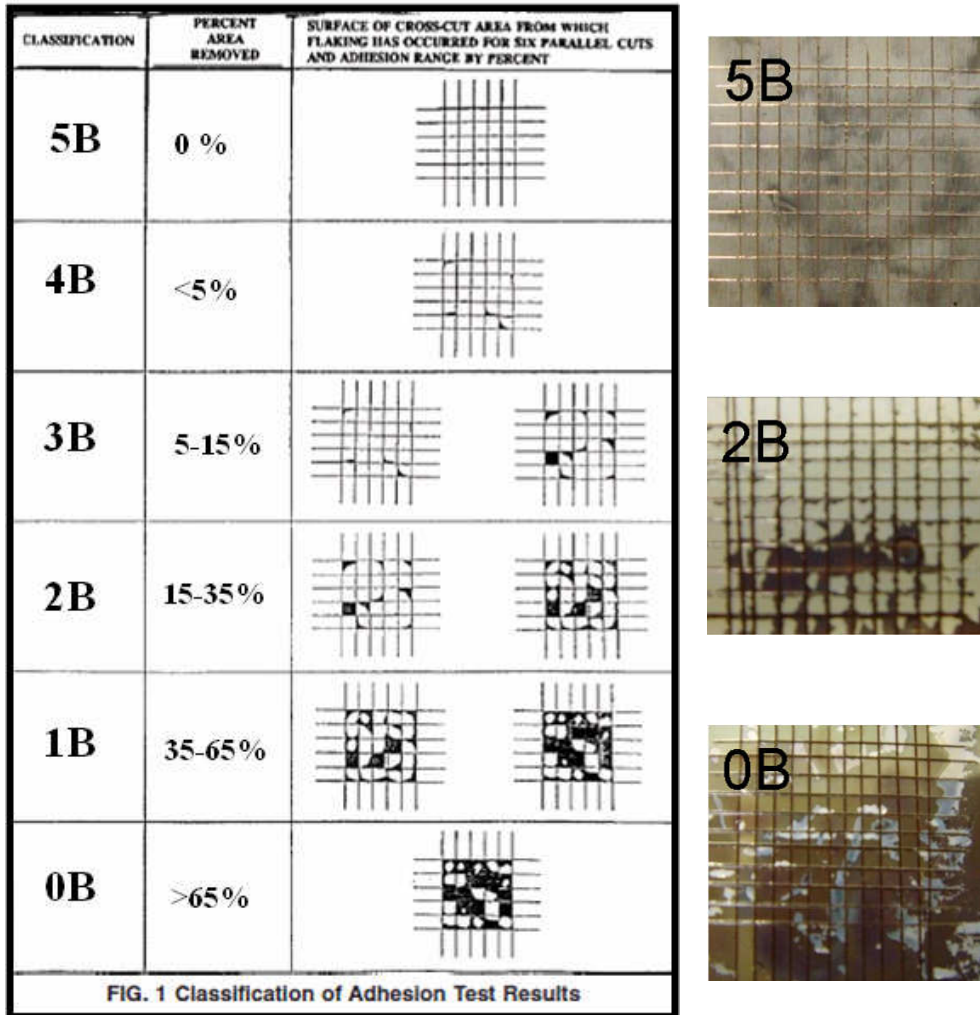
Figure 4.7 Classifications of Adhesion Test Results
(ASTM D 3359-08)

4.2.3 Test Materials

The substrate materials used in the adhesion experiments can be classified by two groups of organic and inorganic materials. The typical properties of the test materials used are summarized in Table 4.1(Howatson 1991, Dupont 2009, Rogers 2009). The

organic materials include Kapton HN, Kapton KJ, LCP 315, SS 415, and Teflon FEP and their chemical structure is shown in Figure 4.8. The Kapton HN is the widely used thermosetting polyimide film supplied by Dupont. Kapton KJ is a thermoplastic polyimide film that can be used for an adhesiveless lamination. LCP 315 is a liquid crystal material with melting point of 315°C supplied from Rogers Corp. SS415 is a thermoplastic material with a glass transition temperature (Tg) of 180℃. Teflon FEP is also a thermoplastic polymer, but its low surface energy property is very well known.

The inorganic materials include copper, copper oxide, aluminum, aluminum oxide, and silicon nitride (Si3N4). Copper and aluminum are the most used chip-pad metals. Each metal has a natural oxide on each surface. Bare copper and aluminum surfaces will be prepared by etching the surface oxide layer from each metal using chemical etching. Copper oxide (Cu2O) is formed on a copper surface when it is exposed to oxygen although it takes extensive time. The copper oxide thickness is known to be about 23-247 nm (Zhang, 2004). The bare copper substrate is prepared by removing the copper oxide layer on the copper substrate using 10% HCl mixed with DI water. Aluminum oxidizes very quickly once it is exposed to air, forming a very stable native aluminum oxide of 2-3 nm thickness (Trunov, 2005). In this study, aluminum oxide (Al2O3) is removed by etching using 10% H3PO4 and 90% DI water. Since the aluminum will be re-oxidized once the chemically etched surface contacts air, a soft solvent such as isoprophyl alcohol will cover the surface and protect it from exposure to air until NPS deposition. Last but not the least, silicon nitride was chosen because of its popular use as a dielectric material.

Table 4.1 Test materials

Category	Material	Supplier	Thick-ness [um]	Tg [℃]	Tm [℃]	UTS [MPa]	CTE [ppm/℃]
Organic	Kapton HN	Dupont	125	360-410	N/A	231	20
	Kapton KJ	Dupont	50	220	N/A	139	20
	LCP 315	Rogers Corp.	50	190*	315	200	17(x,y) 150(z)
	SS 415	Cookson Electronics	50	180-185	N/A	N/A	60
	Teflon FEP	Dupont	50	N/A	260-280	21	N/A
Inorganic	Cu	McMaster Carr (Etched Cu)	625	N/A	1084	210	17
	Cu2O	(Native oxide on Cu)		N/A	1235	N/A	17
	Al	McMaster Carr (Etched Al)	1250	N/A	660	45	23.1
	Al2O3	Native oxide on Al		N/A	2072	260	23.1
	Si3N4	SVM**	675	N/A	1900	375	3.3

*Relative Thermal Index (Mechanical) ** Silicon Valley Microelectronics, Inc.

(a)

(b)

(c)

(d)
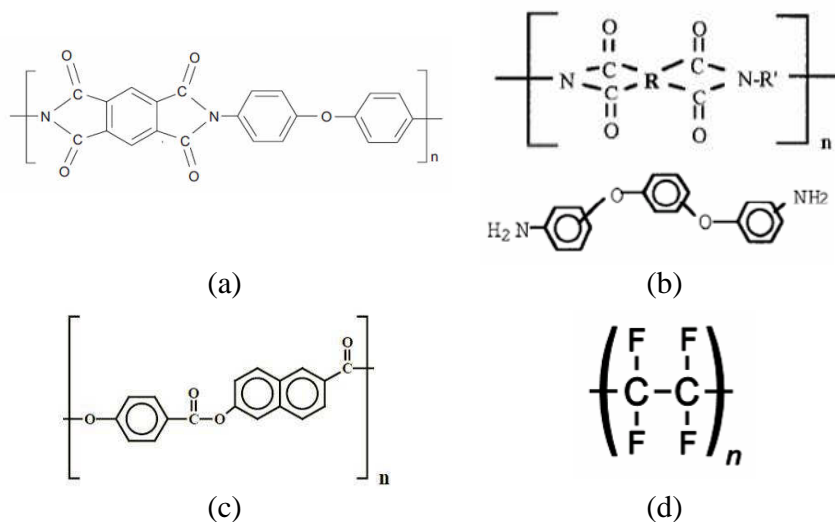
Figure 4.8 Chemical Structure of substrate materials
(a) Kapton HN (b) Kapton KJ (c) LCP 315 (Vectra A950) (d) Teflon FEP

4.3 Experimental Results

4.3.1 Substrate Hardness

4.3.1.1 Organic substrates

As Table 4.2 shows, the adhesion level depends on the substrate materials and the sintering temperature. While SS415 has the strongest adhesion at 182℃ sintering, all the others have very weak adhesion to NPS at the same sintering conditions. At the recommended sintering temperature of 230℃, Kapton KJ, SS415, and LCP 315 show a high adhesion level of 5B, but Kapton HN and Teflon FEP do not stick very well to NPS. These results can be related to the mechanical properties such as the hardness of organic substrates at the associated sintering temperature.

Table 4.2 Tape Test Results at various sintering temperatures

Sintering Temperature [℃]	Kapton KJ	SS 415	LCP 315	Kapton HN	Teflon FEP
174	0B	0B	0B	0B	0B
182	0B	5B	2B	0B	0B
210	2B	5B	5B	0B	0B
230	5B	5B	5B	0B	0B
245	5B	5B	5B	0B	0B

The substrate hardness should be measured at the sintering temperature of around 230℃ because the NPS adhesion might be achieved at such temperature together with NPS sintering. Obtaining a hardness measurement at high temperature is a challenge because it requires a special heating tool and low and stable thermal drift. A hand-made micro heater has been tried for use with Nanoindenter XP and Micro hardness tester, but

problems arose with each.

In a Nanoindenter XP from MTS, there was a massive thermal drift due to the large temperature difference between sample and the indenter tip, shaft, and sensor when the substrate was heated. The thermal drift was about 500nm/s level even at 100℃, but the machine requires a lower value of about 1nm/s in order to obtain reliable data. It took about 2 hrs, for the thermal drift to be stabilized even below 100nm/s at 100C.

A micro hardness tester requires thicker samples than nano-indentation requires because the larger indentation tip requires deeper indentation and larger applied force. In order to provide enough thickness of about 1.5 times indentation depth, the polymer films had to be stacked with more than 10 layers. Worse still, it was almost impossible to heat all the stacked thin films uniformly and to maintain uniform temperature during hardness measurement. Also, the whole process of indenting and cooling down the substrate and the indenter tip to room temperature must be completed within the maximum cycle time of 99 seconds of the machine, which is almost impossible. If thinner samples are used, then a lower load such as 1gf or 5gf has to be used. However, in the case, it is also very difficult to find and measure the indentation mark within reasonable accuracy.

Therefore, the organic substrate hardness at high temperature is measured using a hand-made indenter as shown in Figure 4.9. The indenter tip is made of tungsten carbide and has an angle of 136° between two opposite edges as in Figure 4.9(b), following the tip geometry of the well-known Vickers hardness test. The indenter assembly is put into a convection oven set at high temperature as schematically shown in Figure 4.10(a). The indenter can maintain the vertical standing on the specimen due to the indenter support. Since the indenter is not constrained by the support, it can also move downward as the substrate softens at high temperature.

(a)   (b)
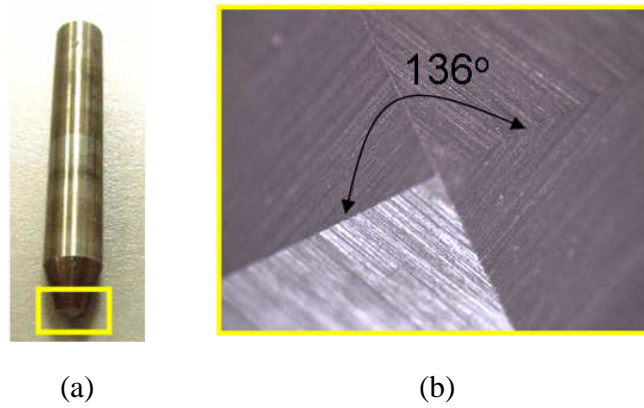
Figure 4.9 Hand-made Indenter
(a) Indenter (b) Indenter tip geometry

(a)   (b)
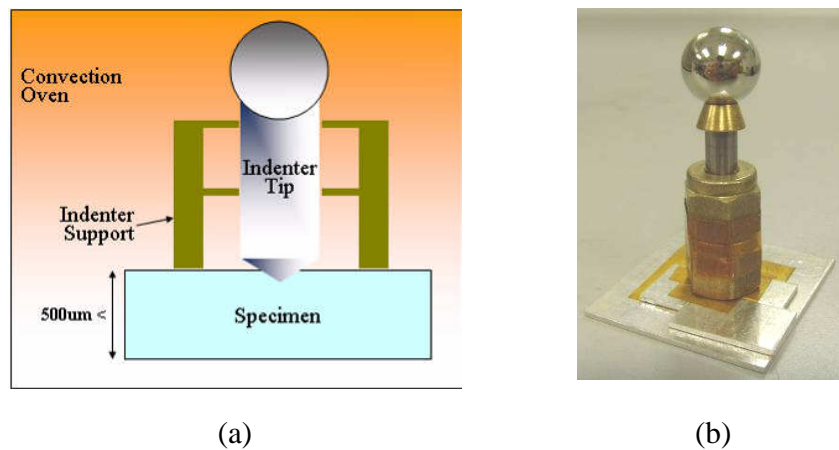
Figure 4.10 Hardness measurements at high temperature
(a) Schematic of high temperature indentation (b) Indenter Assembly

Hardness is not an intrinsic material property such as elastic modulus or yield strength; its value depends on the test method, indenter tip geometry, and indenter tip material. The hardness number obtained from this experiment may or may not be what is required in the van der Waals adhesion model, but the relative change should be reflected accurately. In this experiment, substrate hardness at different temperatures will be measured and the hardness effect on the NPS adhesion to an organic substrate will be qualitatively examined. The substrate hardness change with temperature is similar to the

elastic modulus change with temperature, which is the viscoelastic behavior of polymers with a glass transition temperature (Tg). In the pressure sensitive adhesives, adhesion increases greatly at temperatures slightly higher than the Tg of the polymer and decreases at still higher temperatures. This phenomenon has been known to be associated with a balance between adhesion energy and viscoelastic energy loss. In the adhesion between a zirconia particle with 10.6 um diameter and a cross-linked polyester film, the temperature change through Tg has a dramatic effect on the fracture energy due to the viscoelastic and plastic deformation involved in the particle adhesion and removal processes. Adhesion increases as large as 3 orders in magnitude above the Tg of polyester films are most likely explained by increases in the intimate contact caused by a decrease in the effective modulus of the polymer and by energy dissipation during particle detachment (Toikka, 2001).

The hardness in this experiment is calculated by dividing the applied load by surface area of indentation, following the general Vickers hardness measurement as in Equation (4.1). Figure 4.11 shows the Vickers pyramid indenter indentation mark and Figure 4.12 displays some examples of indentation.
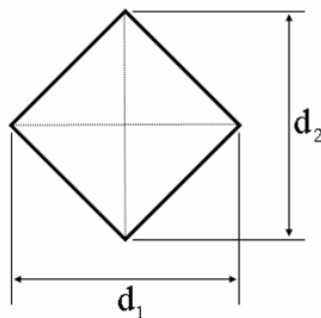
Figure 4.11 Vickers Indentation

$$\text{Measured Hardness [MPa]} = 1.854 \, \frac{F_L}{d^2} \tag{4.1}$$

where F_L is the indentation load in [N], d is the arithmetic mean of the two diagonals, d_1

and d_2 in [um].

63 um	278 um	68 um
(a)	(b)	(c)
244 um	485 um	388 um
(d)	(e)	(f)
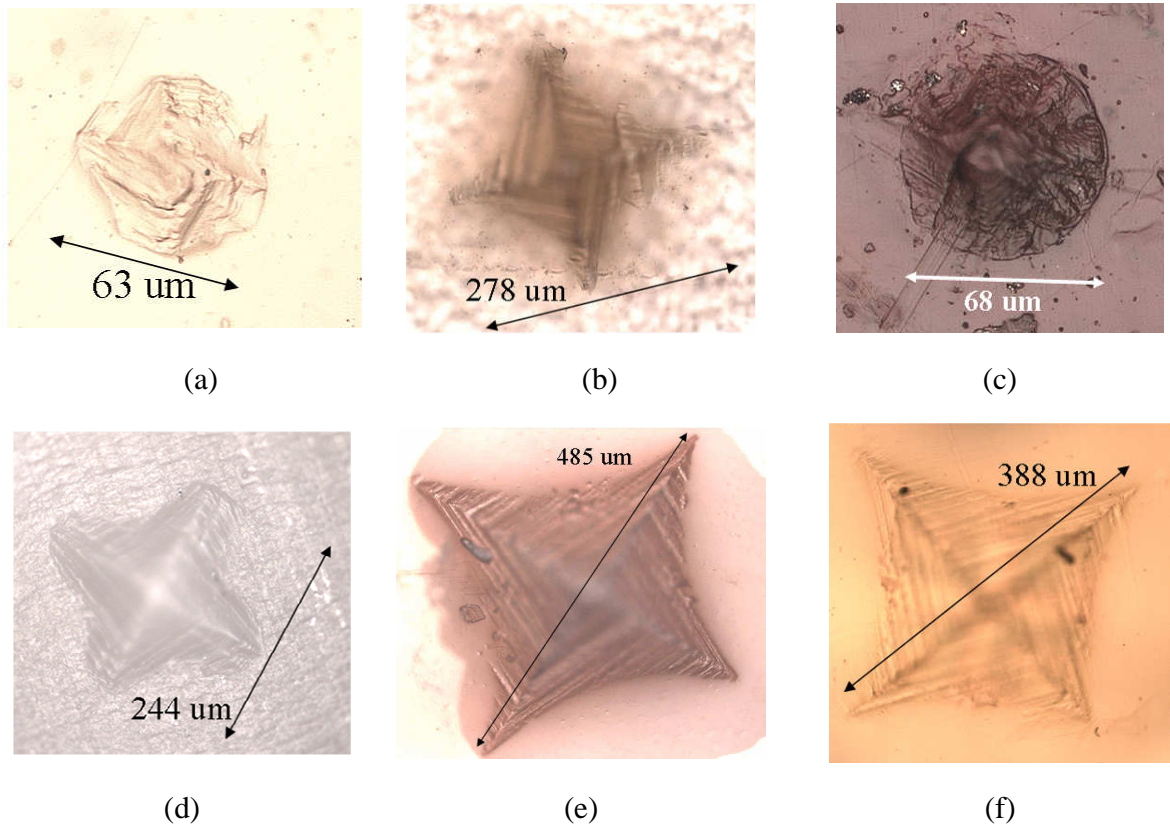
Figure 4.12 Indentation examples
(a) Kapton KJ at RT (b) SS415 at 182℃ (c) Kapton HN at 210℃ (d) LCP 315 at 210℃ (e) Kapton KJ at 230℃ (f) Teflon FEP at 230℃

As Table 4.3 and Figure 4.13 shows, the adhesion level increases as substrate hardness decreases. It seems that there is a certain level of hardness, about 7MPa from the hardness measurement, below which NPS adhesion level is 5B. The only exception is Teflon FEP, which is well known to have low surface energy. The surface energy effect of this material on the adhesion level will be evaluated in the next section.

Table 4.3 Organic substrate hardness and adhesion level

Materials	Temperature [℃]	Indentation Size [um]	Indentation load [gf]	Hardness [MPa]	Adhesion Level
Kapton HN	25	76	62.1688	198	0B
	182	60	17.5688	90.5	0B
	210	68	17.5688	70.4	0B
	230	76	17.5688	56.4	0B
Kapton KJ	25	63	31.5655	147.4	0B
	182	61	17.5688	87.5	0B
	210	133	17.5688	18.4	2B
	230	485	17.5688	1.4	5B
LCP 315	25	55	31.5655	194	0B
	182	170	17.5688	11.3	2B
	210	244	16.8078	5.5	5B
	230	263	17.5688	4.7	5B
SS415	25	78	31.5655	96.2	0B
	182	278	17.5688	4.2	5B
	210	1701	17.5688	0.1	5B
	230	>1701	17.5688	<0.1	5B
Teflon FEP	25	151	31.5655	25.6	0B
	182	255	17.5688	5.0	0B
	210	305	17.5688	3.5	0B
	230	388	17.5688	2.2	0B
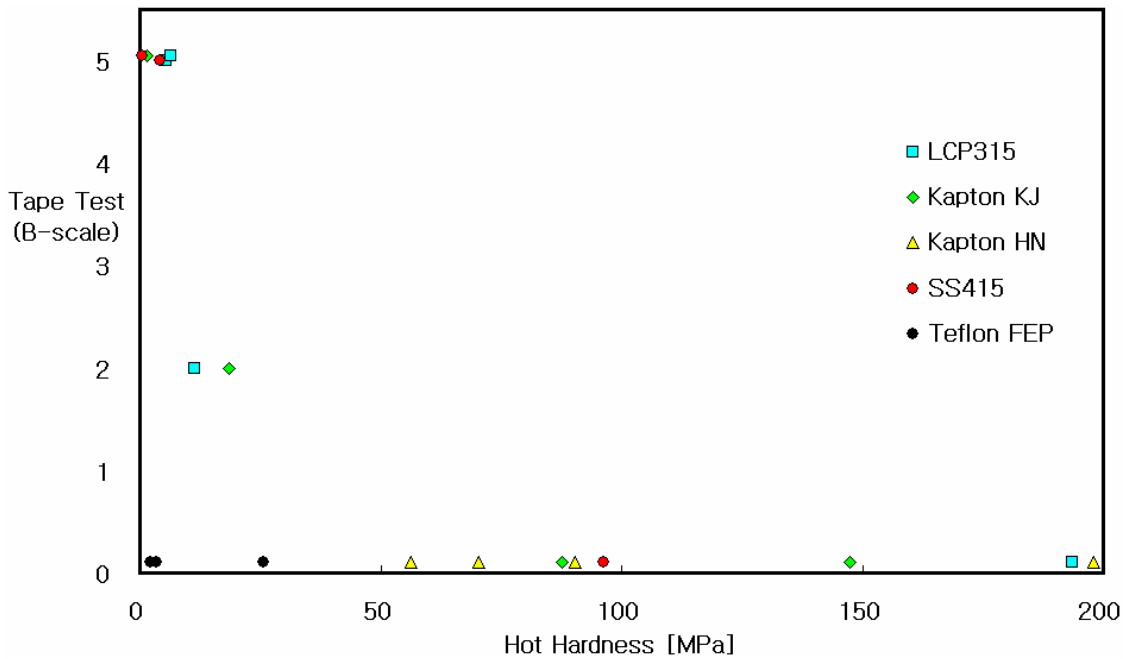
Figure 4.13 Effect of substrate hardness at different temperature on adhesion level

4.3.1.2 Inorganic substrates

Since inorganic substrates are generally harder than organic ones and thus, require higher load in indentation, the hand-made indenter is inapplicable to measure the hardness of the inorganic substrate at high temperature.

Fortunately, the hardness values of inorganic materials have been published, and they are cited in this study as in Table 4.4 (Murali, 2007). Also, the hardness at high temperature, which is also called hot hardness, has been found to follow the general relationship of Equation 4.2 and it is tabulated in the Table 4.4 for each material. (Wang, 1999)

$$H = H_o \exp(-S_o \times (T - T_o)) \tag{4.2}$$

where H is the hardness in MPa, T is temperature in ℃, Ho is the hardness in MPa at T= To=0℃, and S_o is the softening coefficient of hardness in $10^{-4}/℃$.

Table 4.4 Hardness of inorganic materials at NPS sintering temperature

Material	Vickers Hardness (H_o, MPa)	Softening Coefficient of Hardness (S_o, 10-4/^{o}C)	Hot Hardness @230℃ (H, Mpa)	Adhesion Level
Cu	680	12.3	512	5B
			545 (@180℃)	5B
Cu2O	1600	*12.3	1206	0B
Al	415	23.3	243	5B
			273 (@180℃)	5B
Al2O3	23000	7.85	19201	0B
Si3N4	19000	2.79	17819	0B

*assumed value

Using the tape test on the inorganic substrates shows that hardness is a significant factor for NPS adhesion to inorganic substrates, as shown in Figure 4.14.

From this figure, there seems to be a certain level of hardness below which the NPS adhesion level is 5B.
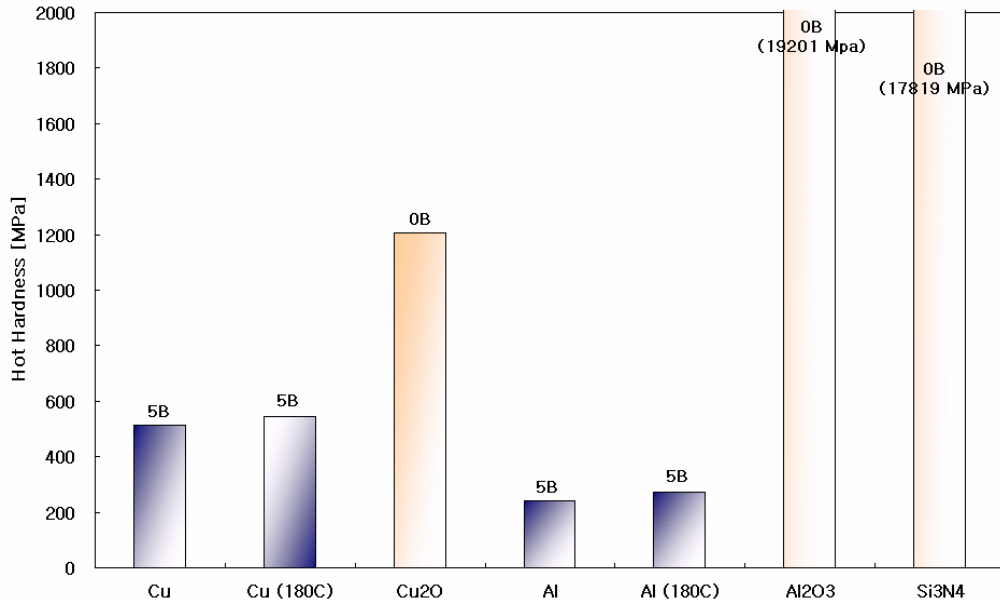
Figure 4.14 Effect of substrate hardness at different temperature on adhesion level

4.3.2 Surface Energy Change

The surface energy change between two solid materials after bonding can be calculated using Equation 4.3 (Yao, 2000).

$$\Delta\gamma = \gamma_1 + \gamma_2 - \gamma_{12}$$
$$= 2(\sqrt{\gamma_1^{LW}\gamma_2^{LW}} + \sqrt{\gamma_2^-\gamma_1^+} + \sqrt{\gamma_2^+\gamma_1^-})$$

(4.3)

where $\Delta\gamma$ is surface energy change, γ_1 and γ_2 are surface energies of material 1 and 2, respectively, before bonding, γ_{12} is surface energy between material 1 and 2 after bonding, LW means Lifshitz-van der Waals component, γ^+ is Lewis-acid parameter of surface free energy, and γ^- is Lewis-base parameter of surface free energy.

Once the surface energies, $\gamma^{LW}, \gamma^+,$ and γ^-, for each material are found, the surface energy change can be calculated.

The Young and Dupre equation, which relates contact angle and thermodynamic work of adhesion, $W_{t(SL)}$, between solid and liquid, is used for finding the surface energies, $\gamma_s^{LW}, \gamma_s^{+}$, and γ_s^{-}, of solid substrates as in Equation 4.4 (Yao, 2000).

$$
\begin{aligned}
W_{t(SL)} &= \gamma_L (1 + \cos\theta) \\
&= W_{SL}^{LW} + W_{SL}^{AB} = 2(\sqrt{\gamma_S^{LW}\, \gamma_L^{LW}} + \sqrt{\gamma_L^{-}\, \gamma_S^{+}} + \sqrt{\gamma_L^{+}\, \gamma_S^{-}})
\end{aligned}
\tag{4.4}
$$

where AB means Acid-Base component, γ_L is surface energy of liquid, and θ is contact angle.

Since the three unknowns, $\gamma_s^{LW}, \gamma_s^{+}$, and γ_s^{-}, need to be found, three liquids with known surface energies $\gamma_L, \gamma_L^{LW}, \gamma_L^{-}$, and γ_L^{+} are needed. In this study, water, glycerol, and diiodomethane are used as the contact angle measurement liquids, and their surface energies are tabulated in Table 4.5 (Yao, 2000).

Table 4.5 Surface energies of three liquids [mJ/m^2]

Liquids	γ_L	γ_L^{LW}	γ_L^{-}	γ_L^{+}
Water	72.80	21.80	25.50	25.50
Glycerol	64.00	34.00	3.92	57.40
Diiodomethane	50.80	50.80	0.00	0.00

Thus, using the Young and Dupre equation, equation (4), the surface energies of substrates can be found from Equation (4.5).

$$
\left.\begin{array}{l}
\gamma_w (1 + \cos\theta_{w/S}) = 2(\sqrt{\gamma_S^{LW}\, \gamma_w^{LW}} + \sqrt{\gamma_w^{-}\, \gamma_S^{+}} + \sqrt{\gamma_w^{+}\, \gamma_S^{-}}) \\
\gamma_G (1 + \cos\theta_{G/S}) = 2(\sqrt{\gamma_S^{LW}\, \gamma_G^{LW}} + \sqrt{\gamma_G^{-}\, \gamma_S^{+}} + \sqrt{\gamma_G^{+}\, \gamma_S^{-}}) \\
\gamma_D (1 + \cos\theta_{D/S}) = 2(\sqrt{\gamma_S^{LW}\, \gamma_D^{LW}} + \sqrt{\gamma_D^{-}\, \gamma_S^{+}} + \sqrt{\gamma_D^{+}\, \gamma_S^{-}})
\end{array}\right\}
\tag{4.5}
$$

where w is water, G glycerol, D diiodomethane, and S solid substrate.

4.3.2.1 Contact Angle Measurement

　　The contact angle is measured using Goniometer as shown in Figure 4.15. Contact angles of each single drop of liquid with substrates are measured and an average of 5 repetitions for each substrate is taken. The contact angle on NPS film is made after the NPS is sintered under the sintering conditions of 230℃ for 1 hr.

(a) Goniometer　　　　　　　　　　　　　　　(b) liquid drop
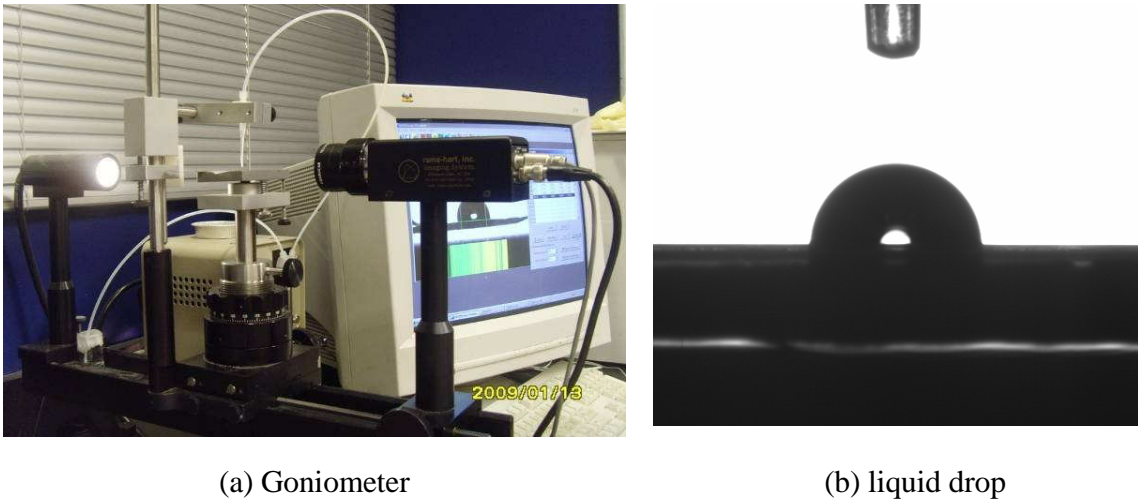
Figure 4.15 Contact Angle measurement

4.3.2.2 Results and Discussion

　　Average contact angles on each substrate with three different liquids are summarized in Table 4.6. The surface energy change for each substrate material after bonding to NPS film is calculated by using Equation (4.3). The detailed calculation for surface energy change using contact angle measurement is in Appendix C with an example of Kapton KJ and NPS film.

Table 4.6 Surface energy change and adhesion level

Materials	Contact Angle [mean±σ°]			Surface Energy Change [mean, mJ/m²]	Adhesion level
	water	Glycerol	Diiodomethane		
Kapton HN	70.5±4.6	67.3±3.7	25.9±2.9	88.7	0B
Kapton KJ	70.3±5.3	59.8±3.5	28.7±1.3	89.0	5B
LCP 315	72.7±3.7	71.2±4.1	36.9±5.4	84.2	5B
SS 415	69.8±2.5	80.4±0.8	23.4±2.7	90.2	5B
Teflon FEP	109.9±4.6	104.8±2.3	83.8±6.5	44.9	0B
Cu2O	86.4±1.3	84.6±3.8	53.6±1.2	74.4	0B
Cu (etched)	81.7±4.3	70.4±5.5	48.9±1.4	78.9	5B
Al2O3	90.4±2.4	73.6±0.6	48.5±0.7	78.9	0B
Si3N4	85.3±1.8	76.0±1.0	56.4±0.7	73.8	0B
Ag (NPS)	82.4±3.7	69.5±3.9	36.7±3.1	84.4	5B

As the adhesion test results show in Figure 4.16, a larger surface energy change alone does not always guarantee higher adhesion as in Kapton HN/NPS adhesion. The reason might be that NPS adhesion is associated with substrate hardness as well and Kapton HN has a large value of substrate hardness at the NPS sintering temperature. On the contrary, Teflon FEP showed very low adhesion to NPS despite its low hardness at NPS sintering temperature. The low adhesion of Teflon FEP can be due to the relatively small surface energy change, resulting in large adhesion distance, as we will discuss further in a later section.
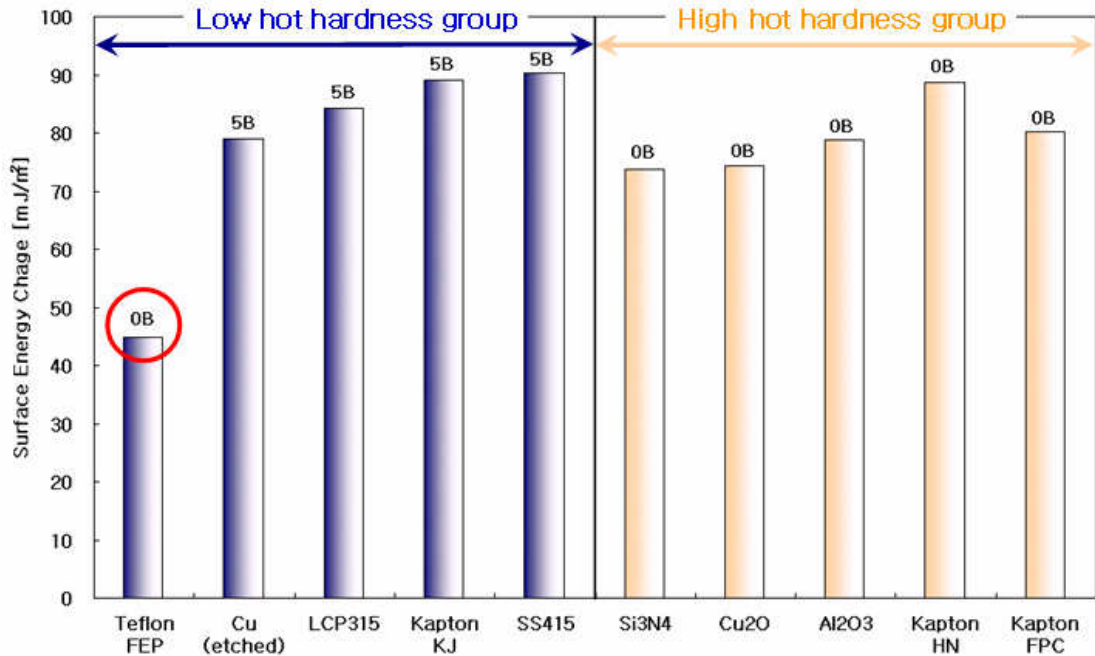
Figure 4.16 Effect of surface energy change on adhesion level

4.3.3 Chemical Bonding

4.3.3.1 Hydrogen Bonding

Surface interactions between particle and substrate via hydrogen bonding can occur because many solid surfaces contain potential hydrogen bond donors and acceptors, and hydrogen bond formation requires low activation energy. In fact, the existence of hydrogen bonds between spherical and flat fused SiO_2 surfaces has been identified (Peschel, 1970). Although the hydrogen bond is not a strong chemical bond, it may play an important role in the particles' adhesion to substrate surfaces because it is about 5 times stronger than the van der Waals adhesion (Pauling, 1960, Israelachvili, 1991). Moreover, hydrogen bonds have a dominant effect on the adhesion of both SiO_2 and Al_2O_3 with hydrophilic silicon surfaces (Wu, 1999). Since hydrogen bonds were found in the SiO_2-SiO_2 surface (Peschel, 1970) and Al_2O_3-SiO_2 surface adhesion (Wu, 1999), oxide substrates such as SiO_2, Cu_2O, and Al_2O_3 are used as test substrates in this study

for identifying hydrogen bonding in NPS adhesion. Figure 4.17 represents a possible interaction between hydrogen on SiO2 and oxygen in a silver nano particle surface.
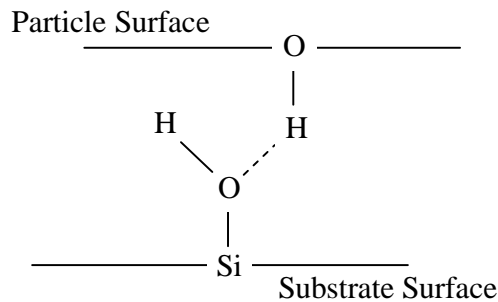
Figure 4.17 Hydrogen bonding model between nano particle silver and substrates

The tape test results for oxide surfaces as in Table 4.7 suggests that limited hydrogen bonds were formed because of the low adhesion level between NPS and all the oxide surfaces studied. The low adhesion might be because when NPS is heated to 230°C for 1 hr, the hydroxyl group, if any, may evaporate. Also, the silver oxide has been known to decompose at around 210C, which is another possible reason for the potential lack of hydrogen bonds.

Table 4.7 Tape test results for oxide surfaces (Sintering conditions: 230C, 1 hr)

Materials	Adhesion level
SiO2	0B
Al2O3	0B
O2 Plasma-treated Al2O3	0B
Cu2O	0B

4.3.3.2 Covalent & Ionic Bonding (Silane Coupling Agent)

A Silane coupling agent is used as a dispersion agent to prevent particles from agglomerating. Although the mechanisms of action are not fully understood, the silane treatment clearly decreases the surface energies of the object (Mealey, 2006).

It is also well known that the addition of silane coupling agent improves the adhesion between metallic fillers and the polymer matrix in electrically conductive adhesives (ECA). The dramatic improvement in conductivity of ECA with the addition of KH-570 silane coupling agent was due to the good adhesion between fillers and matrix resulting from minimizing the filler–filler and filler–matrix gaps (Tan, 2005). Also, surface modification of Ag nanoparticles (diameter: 70nm) using silane-based coupling agent, 3-aminopropyl triethoxysilane (3APTES), has improved the Ag filler-epoxy resin adhesion (Tee 2007). The 3APTES functions as a molecular bridge at the interface between Ag filler and epoxy resin, resulting in the ionic and covalent bond formation of – -Si-O-Ag and –Si...HN-C across the interface as shown in Figure 4.18.
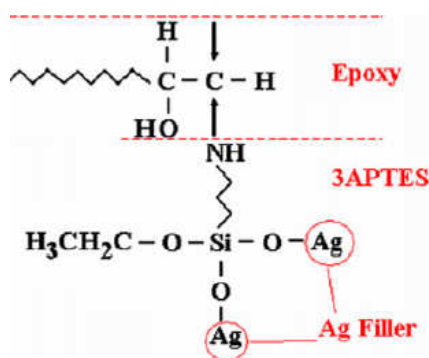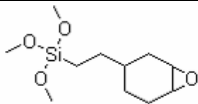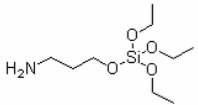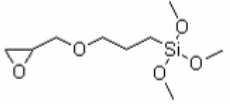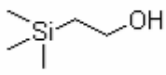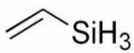
Figure 4.18 Amino-silane Bridge in Ag filler-epoxy resin adhesion
(Source: Tee, 2007)

To understand the influence of Silane on NPS adhesion, the nano particle silver inks are mixed with 1wt% of silane coupling agents and the inks are deposited and sintered on Kapton FPC, which showed 0B adhesion level with as-received NPS. The silane coupling agents used in this experiment are listed in Table 4.8 with each chemical structure and boiling point.

Table 4.8 Silane based coupling agent used in this study

Silane Coupling Agent	Molecular Structure	Molecular Formula
Epoxy (Ethyltrimethoxy silane)		$C_{11}H_{22}O_4Si$
Amino (Aminopropyltriethoxysilane)		$C_9H_{23}NO_3Si$
Glycidoxypropyltrimethoxysilane		$C_9H_{20}O_5Si$
Trimethylsilylethanol		$C_5H_{14}OSi$
Vinylsilane		C_2H_6Si

As Figure 4.19 shows, the Amino-silane coupling agent allows NPS to adhere strongly to Kapton FPC while vinyl-silane improves NPS adhesion up to the 4B level. The as-received NPS may contain some silane coupling agents, but their initial effects are negligible before adding Amino-silane coupling agents. Thus, although the NPS adhesion strength can be improved via covalent bonding using a Silane coupling agent, any ionic or covalent bonds between as-received NPS and Kapton FPC (or any other organic substrates) are negligible based on this study. The adhesion level increase from 0B to 5B in the ASTM tape test due to silane addition for Kapton HN substrate is shown in Figure 4.20.
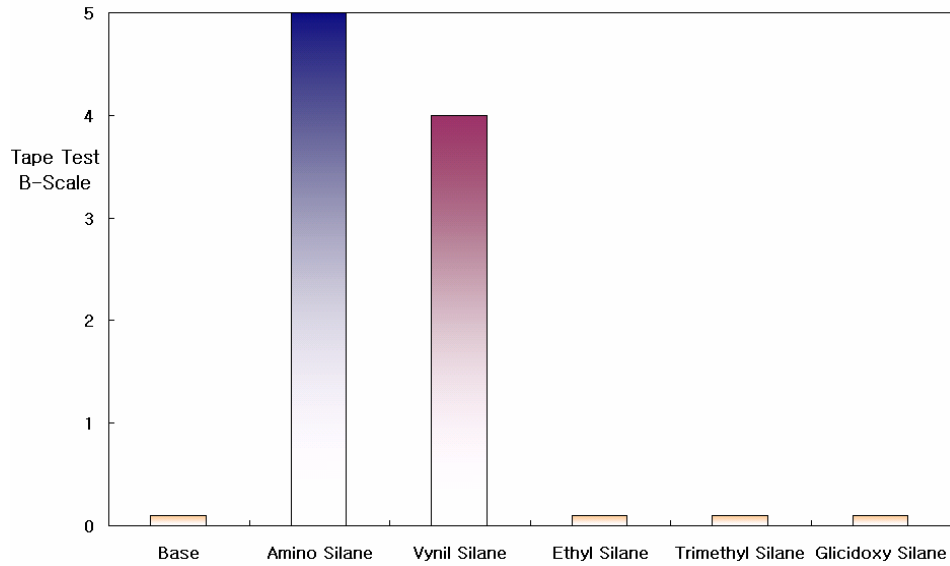
Figure 4.19 Tape test results for silane addition
(Sintering conditions: 230C, 1 hr)

(a)   (b)   (c)
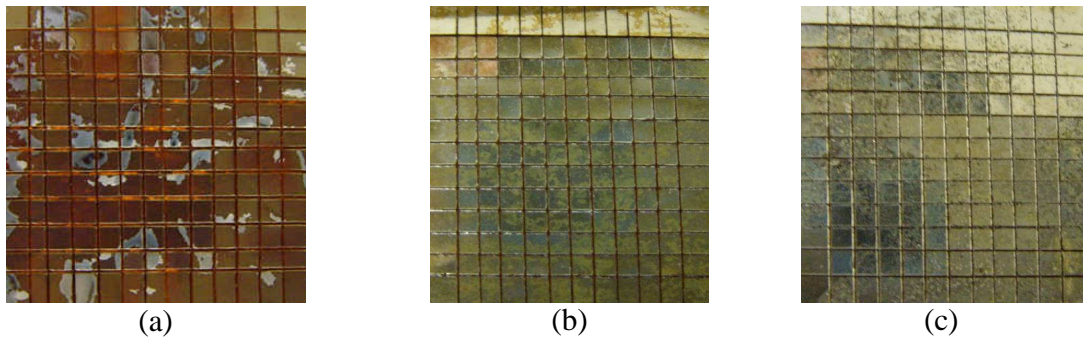
Figure 4.20 ASTM Tape test on NPS/Kapton HN adhesion (a) As-received NPS (0B)
(b) Amino-Silane addition (5B) (c) Vinyl-Silane addition (4B)

4.3.4 Surface Roughness

4.3.4.1 Surface Roughness Measurement

The surface roughness that is taken in this measurement is arithmetic average roughness (Ra), as opposed to root-mean-square average (Rq), which is defined as Equation (4.6) in conjunction with Figure 4.21 (Kalpakjian, 2007).
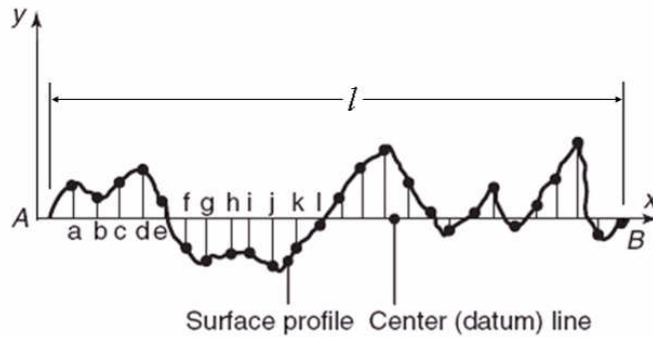
Figure 4.21 Surface profiles for surface roughness measurement
(Source: Kalpakjian, 2007)

$$R_a = \frac{y_a + y_b + y_c + \cdots + y_n}{n} = \frac{1}{n}\sum_{i=a}^{n} y_i = \frac{1}{l}\int_0^l |y|\,dx \qquad (4.6)$$

Surface roughness of substrates before bonding to NPS is measured using a Zygo surface profiler as displayed in Figure 4.22. The surface profiler has a resolution of less than 1 nm in the surface roughness measurement. The surface roughness of 10 spots on a substrate will be measured and their average will be taken as the nominal surface roughness of the substrate. Rough surface substrates are prepared by mechanically rubbing using 600P1200 SiC grinding paper, with particle size of 15.3-16 um, and then by washing with isoprophyl alcohol.

Figure 4.22 Zygo Surface Profiler

Some examples of the surface roughness measurement are displayed in Figure

4.23 with each intensity map and oblique plot. As the substrate surface is smooth, the interferometer fringes look parallel and continuous as in Figure 4.23(a).

(a)

(b)
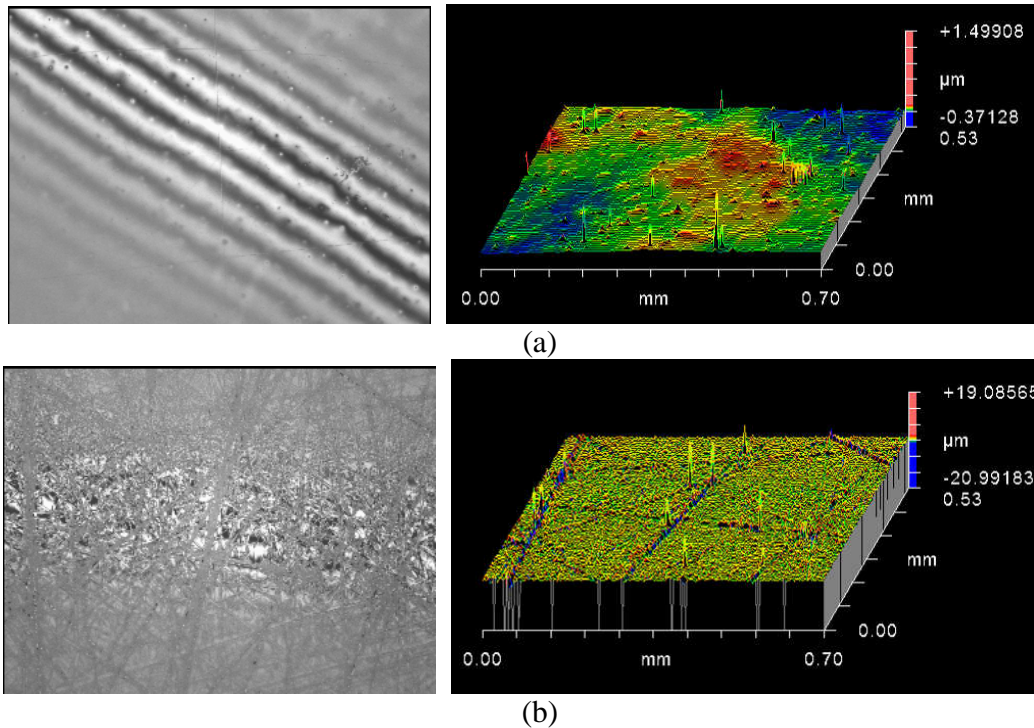
Figure 4.23 Examples of surface topography with oblique plot
(a) As-received Kapton KJ (Ra = 23nm) (b) Roughened Kapton HN (Ra = 350 nm)

4.3.4.2 Results and Discussion

The measured surface roughness values for as-received and roughened substrates are summarized in Table 4.9 and displayed in Figure 4.24 with each adhesion level with NPS film. As shown in Figure 4.24, the surface roughness effect seems to be negligible because the high adhesion materials such as LCP 315 and Kapton KJ still have high adhesion levels regardless of substrate surface roughness level. Likewise, the low adhesion materials, Kapton HN and Al2O3, show the same low adhesion level even after increasing surface roughness. The adhesion levels of 0B even after increasing the surface roughness from 33nm to 366nm for Kapton HN are shown in Figure 4.25.

Table 4.9 Surface roughness and adhesion level

Materials		Surface Roughness [mean±σ nm]	Adhesion Level
Kapton HN	As-received	33±7	0B
	Roughened	366±88	0B
LCP 315	As-received	79±11	5B
	Roughened	546±63	5B
Kapton KJ	As-received	27±21	5B
	Roughened	397±29	5B
Al2O3	As-received	41±10	0B
	Roughened	306±43	0B
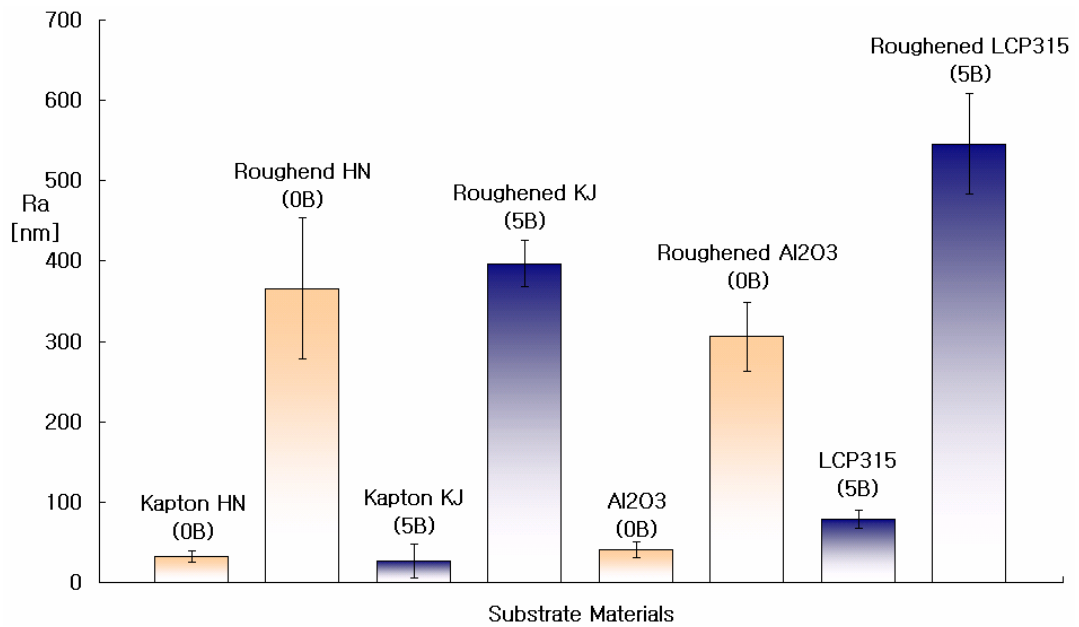
Figure 4.24 Surface roughness effects on NPS adhesion

(a)	(b)

Figure 4.25 ASTM Tape test on NPS/Kapton HN adhesion
(a) Ra=33nm (b) Ra=366nm

On the other hand, from the particle adhesion perspective, the surface roughness effect on adhesion can be distinguished by three cases as in Figure 4.26. First, Figure 4.26(a) indicates an ideally smooth surface. A spherical glass particle adhered to a fused glass surface can be an example of the ideally smooth surface. When the substrate has a roughness an order smaller than particle diameter as in Figure 4.26(b), the true particle-surface contact area can be smaller, and the adhesion force will be accordingly reduced. In the last case when the surface roughness is comparable with the particle dimensions, as in Figure 4.26(c), an increase in adhesion force is expected due to the increased contact area. However, all the measured surface roughness levels in Table 4.9 are an order of magnitude larger than the particle dimension of 8 nm so that the surface roughness change does not seem to be effective any more. Therefore, surface roughness may not have any significant effect on NPS adhesion to substrates from the particle adhesion standpoint.
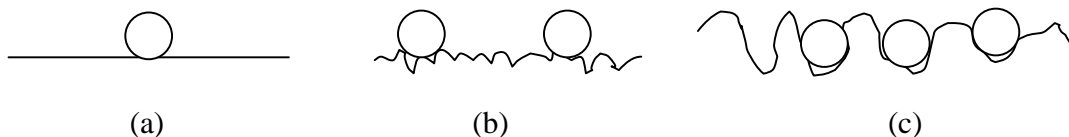
(a)	(b)	(c)

Figure 4.26 Surface roughness types associated with particle adhesion
(a) Ideally smooth surface (b) Smaller roughness than particle dimension (c) Comparable roughness with particle dimension

4.3.5 Diffusion & Metallic Bonding

Depth profiling experiment using Auger Electron Spectroscopy (AES) with sputtering is one of the best ways to examine the diffusion layer at the interface. In the depth profiling, ion sputtering, which usually uses Ar gas, removes a thin layer of the sample for a known time, thus making depth calculation possible. The residual surface is then analyzed by AES, giving the depth distribution of different species in the sample. Depth profiles are shown as Auger peak height vs. sputter time or atomic concentration (%) vs. sputter depth.

The depth profile of a NPS-Cu interface processed in the air is shown in Figure 4.27(a) as atomic concentration versus sputter time accompanied with the corresponding focused ion beam (FIB) etching cross-section sample in 4.27(b). As they show, a diffusion-like layer exists at the interface, and is about the same thickness as the oxidized layer. The oxidized layer identification becomes clearer when it is compared with a NPS-Cu interface processed in an inert gas (N2 and 4% H2) environment. As shown in Figure 4.28(a) and (b), the oxidized layer has disappeared, while a diffusion-like layer still exists. Thus, in NPS adhesion, diffusion or other interfacial reactions can occur between NPS and metal interface.

(a)

(b)
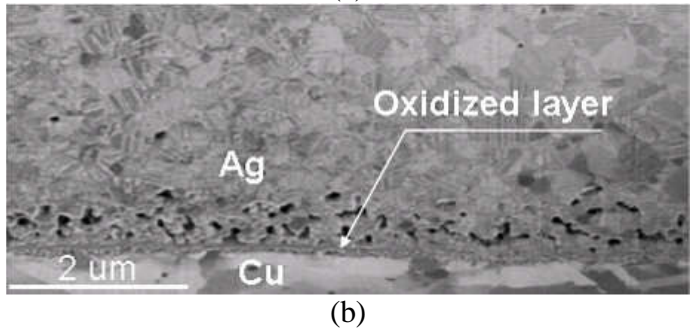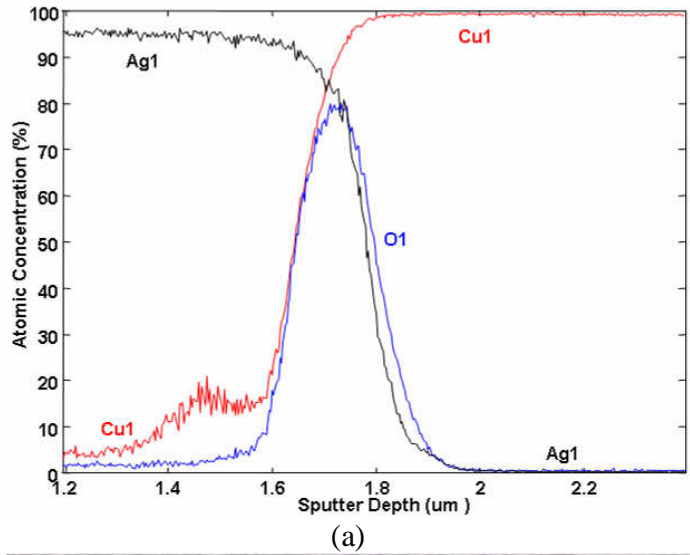
Figure 4.27 NPS-Cu interface processed in the air
(a) AES depth profile (b) FIB cross section sample (Data from NPS manufacturer)

(a)

(b)
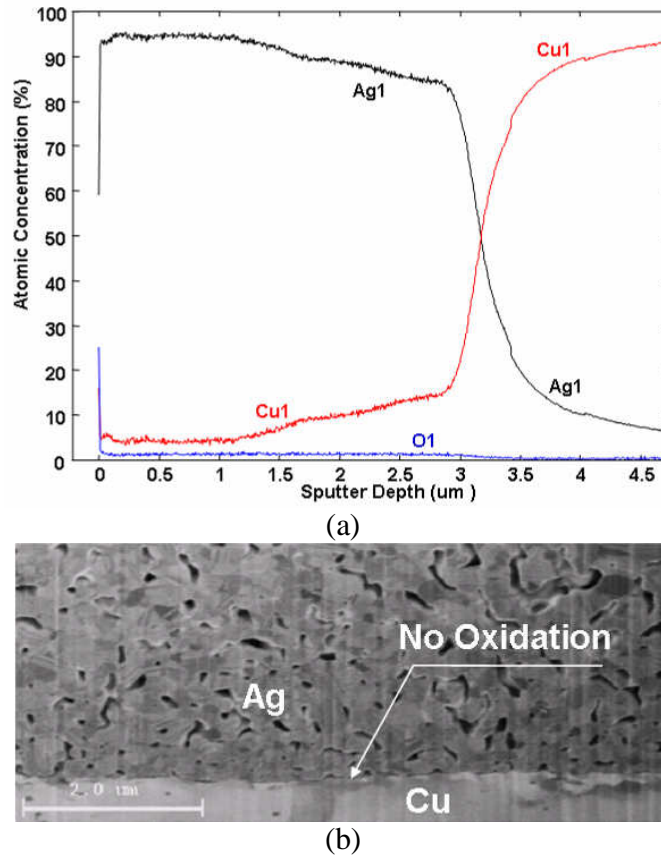
Figure 4.28 NPS-Cu interface processed in the N2+4%H2
(a) AES depth profile (b) FIB cross section sample (Data from NPS manufacturer)

4.4 Summary

NPS adhesion mechanisms are found to follow the general particle adhesion mechanisms in this study. In the organic substrates to NPS adhesion test, the adhesion level variations according to the sintering temperature are evidence of the particle adhesion mechanisms. Each organic substrate material has a certain temperature at which the substrate material gets softer just like a glass transition temperature (Tg) and NPS forms a strong adhesion with the substrate. The hardness value, at which NPS sticks to the substrate very well at the sintering temperature, seems to correspond to about 7MPa based on the Vickers hardness measurement in this study.

The substrate hardness effect on the NPS adhesion was also shown in experiments using the inorganic substrates. Removing the very hard oxide layers on the metal substrates such as Cu and Al increases the level of NPS adhesion to the metal substrate as expected from the particle adhesion mechanism.

The surface energy change calculated from the contact angle measurement shows some effects on the NPS adhesion because the low hardness but weak adhesion of Teflon FEP at the sintering temperature can be explained by the large adhesion distance due to the small surface energy change.

Hydrogen bonds between silver nano particles and substrates are negligible because all the oxide surfaces such as SiO_2, Al_2O_3, Cu_2O, and even O_2 Plasma-treated Al_2O_3 showed very weak adhesion levels. For the as-received NPS before adding Silane coupling agents, ionic and/or covalent bonds between silver and organic substrates are ignorable.

The surface roughness effect is also negligible because the high adhesion materials still have a high adhesion level and the low adhesion materials show the same low adhesion level even after increases in the surface roughness level. This result might be in accordance with the particle adhesion mechanism by which the surface roughness will not be effective any more once the surface roughness levels are beyond the particle dimension.

Diffusion or other interfacial reaction between NPS and copper seems to exist. Regardless of the oxide layer between silver and copper, a diffusion-like layer was always found at the interface of silver and copper based on the AES analysis. This result implies the possibility of diffusion or other interfacial reactions between NPS and metal substrates.

CHAPTER 5

QUANTITATIVE ADHESION STRENGTH MEASUREMENT

5.1 Conventional Adhesion Test Methods

Conventional adhesion test methods can be classified into three categories according to the measured quantities: Four-point bending, Bulge and Blister test, and Peel test such as T-Peel test and 90° Peel measure energy per unit area (J/m2), which is equivalent to force per unit length (N/m). Pull test provides force per unit area (N/m2) as a measured unit. Scratch test measures force (N).

It is well known that the relationship among the adhesion strengths measured from these different test methods is unclear (Mittal, 1987). Also, it should be noted that large scattering is an intrinsic problem in any adhesion test method (Akira, 1993). Large variation of adhesion strength is observed even in carefully prepared samples. This is attributed not only to measurement methods, but also to the non-uniformity of adhesion strength just as shown in the adhesion level of 1B or 2B in the ASTM tape test. In spite of the difficulty in evaluating adhesion, adhesion enhancement or improvement techniques have been developed based on the average adhesion strength value and are widely used in a variety of industries.

A four-point bending test has been used to measure the interfacial fracture energy between aluminum and epoxy underfill material (Yao, 2000). However, the four-point bending test is not applicable to NPS adhesion strength measurement because NPS film is too thin (~2 um) to provide flexural rigidity to resist bending. A Bulge and Blister test uses test samples with a free-standing window on the backside, which is fabricated using

a photolithography and wet etching process. It is very difficult to fabricate NPS test samples for Bulge and Blister testing because the NPS adhesion test needs a large number of samples with different substrate materials to examine various aspects of different adhesion factors. Making that number of samples using photolithography and wet etching is very time consuming, making it impractical of this research (Xiang, 2008). The difficulty in sample manufacturing is also encountered in a T-peel test sample. Since the NPS film is too thin to separate and peel off as the regular T-peel test (Yu, 2002), another film has to be attached to the NPS film using adhesive and to be peeled off. It is very hard to control adhesive thickness uniformly throughout the width and length of the flexible NPS-substrate specimen. The adhesive thickness variations cannot only result in the significant scattering and contamination of test results, but also present difficulty in interpreting the test results. A 90° peel-test presents an additional challenge to that of T-peel test: a special fixture moving the substrate at the same rate of peel. A pull-off test is not sufficiently repeatable because of the difficulty of achieving uni-axial tension loading. An off-axis pulling force due to a tilted sample or to unbalance in machine gripping can generate a bending moment at the interface, which results in much lower fracture strength than pure tensile strength and large scattering accordingly (Kinbara 1993, Valli 1986). A scratch test has been developed for measuring very thin film adhesion strength, but it is hard to find an appropriate scratch tip for the NPS film thickness and substrate materials. An additional challenge in the scratch test is not only the very expensive test equipment such as a nano-indenter and scanning electron microscope (SEM), but also the difficulty of interpreting the scratch test data (Valli 1986, Bull 2006).

Therefore, a new test method for measuring NPS adhesion strength was developed. Since the final goal of the test method is to examine the effects of adhesion factors on the NPS adhesion strength and to make it possible to produce reliable

electronics packages with NPS interconnects, quickly preparing samples and measuring adhesion strength is the most important factor to be considered. While all the conventional test methods aforementioned could be good ways to obtain data and they might be useful as future work for an additional level of data, a new adhesion test method is necessary to make and test very large numbers of samples with high time efficiency. The newly developed adhesion test method is called the Modified Button Shear Test (MBST) because it modifies the conventional button shear test (Sham 2003, Fan 2005) and also integrates the generally known die shear test (Shi 1999). The MBST is used for measuring the interfacial fracture energy of thin films including NPS interconnect material.

5.2 Modified Button Shear Test (MBST)

In order to prepare a MBST sample as shown in Figure 5.1, NPS film should be first formed on a substrate. Then, a $5 \times 10 mm^2$ silicon die, which is already cleaned by wiping with isopropyl alcohol, is attached to the NPS film using an epoxy adhesive. The epoxy adhesive is used for making an adhesive button with a controlled diameter and height. The adhesive button size is very important in the MBST sample for analyzing stresses at the fracture surface. To control the adhesive button height, spacers made of polyimide tape were used. Two pieces of polyimide tape are attached on the NPS film in parallel with 8 mm spacing. Also, for controlling the adhesive button diameter, one drop of liquid epoxy adhesive was dispensed on the center of the die surface under the dispensing pressure of 40psi for 2.7 seconds. Once the NPS film with spacers and the die with an epoxy adhesive are ready, pick and flip the die using tweezers, and then put the two edges of the die on the two spacers such that each edge length on the spacers is around 1mm. In case of fabricating a large number of samples on the same substrate, the distance between two dies should be also considered so that the shear tool can enter the

space between two dies, and apply force to the side surface of a die. To complete fabricating adhesive button, the die and substrate assembly, as shown in Figure 5.1(a), needs to be cured at 150°C for 30 min. After curing the epoxy adhesive and before MBST testing, the spacers should be removed using isopropyl alcohol, as shown in Figure 5.1(b), because, otherwise, the friction between die edge and spacers and the resulting deformation of spacers during MBST testing could affect the test results by increasing facture forces. The MBST is performed using a Dage 4000 series die shear tester as in Figure 5.1(c). The shear rate is selected as 1 mm/min to minimize the effect of shear speed on the test results. The shear height is chosen as 10 um to exert the applied force through the full side area of a die.

(a)

(c)

(b)
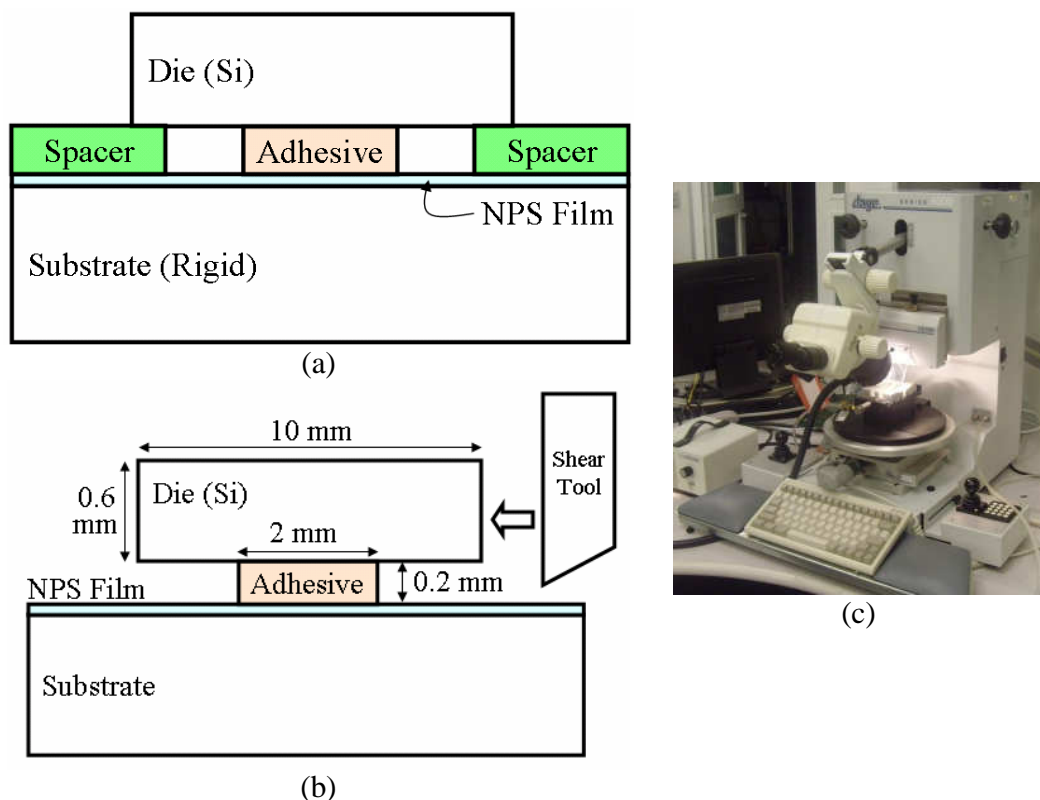
Figure 5.1 Modified Button Shear Test (a) MBST sample before removing spacers (b) Test specimen configuration (c) Dage 4000 Die Shear Tester

5.2.1 Loading Conditions

In order to generate interfacial fracture under different combinations of interfacial tension and shear stresses, three different loading configurations are used in this study. The test configuration in Figure 5.2(a) is denoted as Full Die Shear because the full side area of a die is under pressure from the applied force. By shifting half of the side length of a die, 2.5mm, Mid Die Shear and Large Die Shear are developed to be tested as in Figure 5.2(b) and 5.2(c). The Large Die MBST is used as an independent verification of the MBST test methodology.
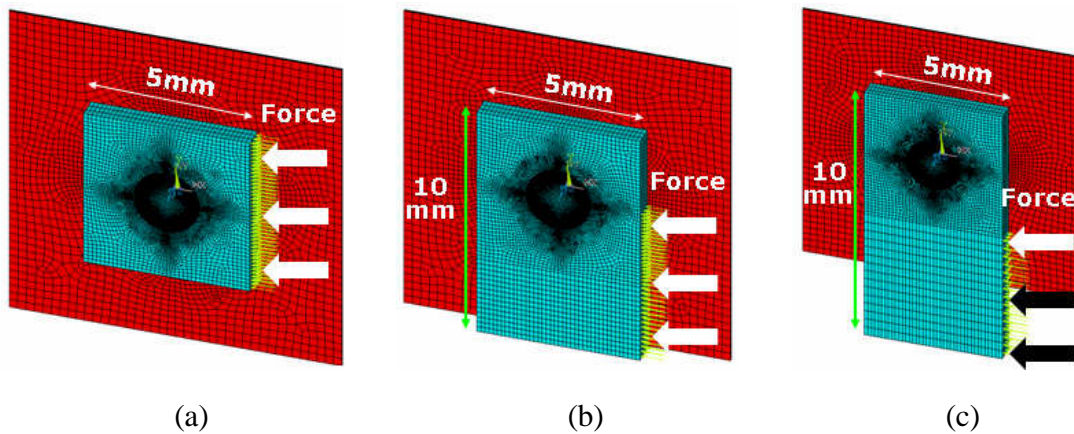
Figure 5.2 Three different loading conditions for MBST
(a) Full Die MBST (b) Mid Die MBST (c) Large Die MBST

5.2.2 Test Method Development

The overall sequence for finding the interfacial fracture energy using the MBST is shown in Figure 5.3. First, the MBST provides fracture forces as outputs for each test specimen. Then, adhesive height and diameter are simply measured by a microscope x, y & z scale, or an image processing technique can be used to measure adhesive diameter. Fracture force, adhesive diameter, and adhesive height are the inputs to a FEM simulation. The FEM simulation generates the average tensile stress and the average

shear stress at the fractured interface between the NPS and the polymer substrates. These average stresses are exploited for finding interfacial bond strength in tension (Z) using the interfacial fracture criterion. The Z is directly related to the interfacial fracture energy through Kendall's model, which will be discussed in detail in the next section. The interfacial fracture energy varies depending on the physical, mechanical, and chemical states of the interface as discussed. Thus, the MBST can be repeated for each adhesion factor that is varied, such as contact angle, surface roughness, and chemical species. The contribution of each adhesion factor to the interfacial fracture energy is expected to be identified using the MBST, and the guidelines for improving the adhesion strength of the NPS interconnect could be developed.
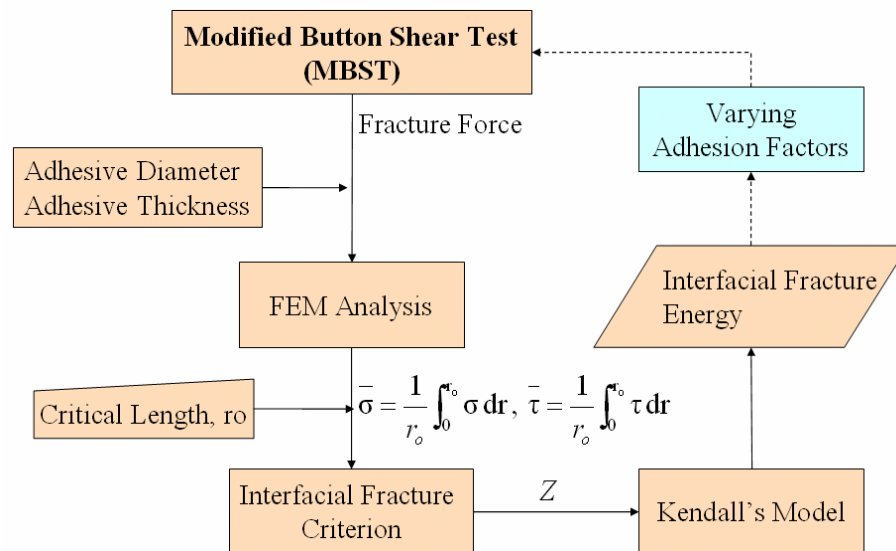
Figure 5.3 Flow Chart of Thin Film Interfacial Fracture Energy Measurement

5.2.3 Fracture Force

The free body diagram of Full Die MBST shown in Figure 5.4(a) suggests that the stress components at the fracture surface are composed of shear stress due to shear force (F_i) and normal stress due to bending moment (M_i). The NPS cohesive force (F_c)

needs to be analyzed. The NPS cohesive force would be approximately the product of the tensile strength of NPS and the cohesive fracture area. It is assumed that the tensile strength of pure bulk silver of 170MPa (Howatson, 1991)(Howatson, G. et al. 1991) can be used to estimate the maximum NPS cohesive force in this study. The maximum cohesive force is only 3.3% on an average of the total fracture force (F_f) for twenty LCP315 samples based on the calculation in Equation (5.1). Thus, the cohesive fracture force in NPS film can be concluded to be negligible from a magnitude perspective. The free body diagram of Mid Die and Large Die MBST can be drawn together as shown in Figure 5.4(b) because they are only different in the distance from the center of the epoxy button to that of the applied force, δ. When δ is equal to zero, it corresponds to the Full Die MBST.

(a)

$$M_i \approx F_f \times h$$

$$T_i \approx F_f \times \delta$$

(b)
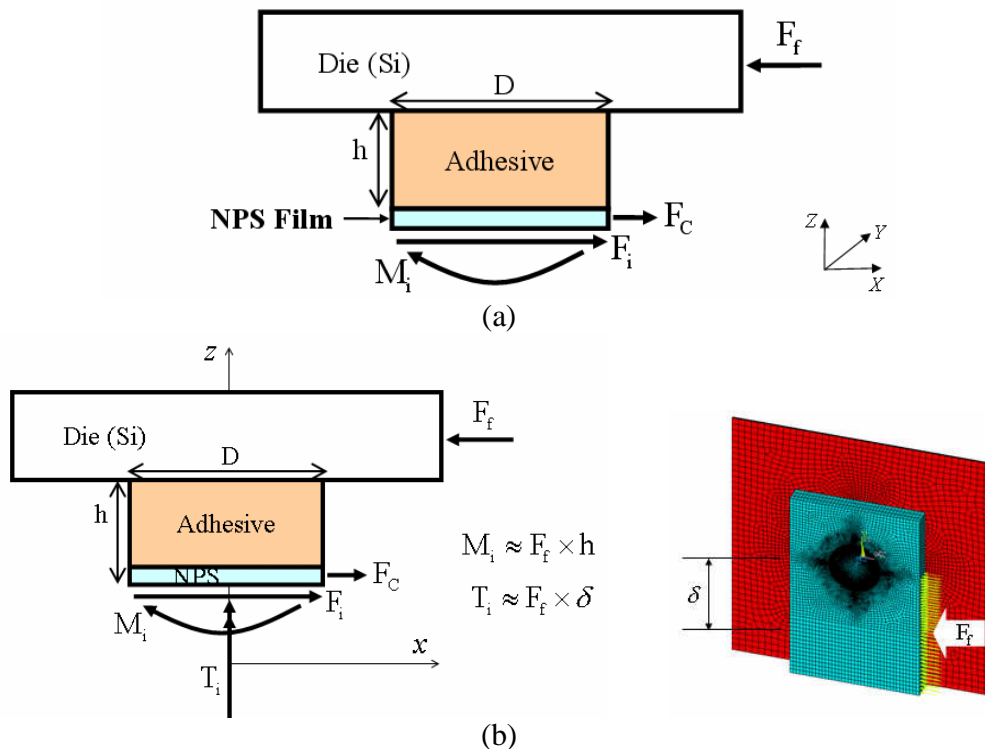
Figure 5.4 Free body diagram of MBST (a) Full Die MBST (b) Mid Die and Large Die MBST (D: Adhesive diameter, h: Adhesive height)

8 6

$$\frac{F_c(\text{max})}{F_f} = \frac{\sigma_{\text{UTS(Ag)}} \times t_{\text{film}} \times \pi \times D}{F_f} = \frac{170\text{MPa} \times 2\text{um} \times \pi \times D}{F_f} \sim N(3.3\%, 0.6^2\%) \qquad (5.1)$$

where F_c is NPS cohesive force in N, F_f is total fracture force in N, σ_{UTS} is ultimate tensile strength in MPa, t_{film} is film thickness in um, and D is adhesive diameter in um.

5.2.4 Button Dimensions

The fracture surface area after the MBST, as shown in Figure 5.5, is measured by the microscope x, y & z scale or the image processing function in Adobe Photoshop CS3. The exposed area of LCP315 is contoured by a mouse indicator as in Figure 5.5(c) and the number of pixels within the contour is measured. The counted number of pixels is compared with a reference area, whose number of pixels is known at the same resolution and magnification, and is then transformed into the area of the fracture surface. For example, the number of pixels within a contour is 135,564, and the reference area is 7.91mm^2 at 307,200 pixels with 50x magnification, then, the fracture area is calculated to be 3.49 mm^2, resulting in a diameter of 2.1mm.
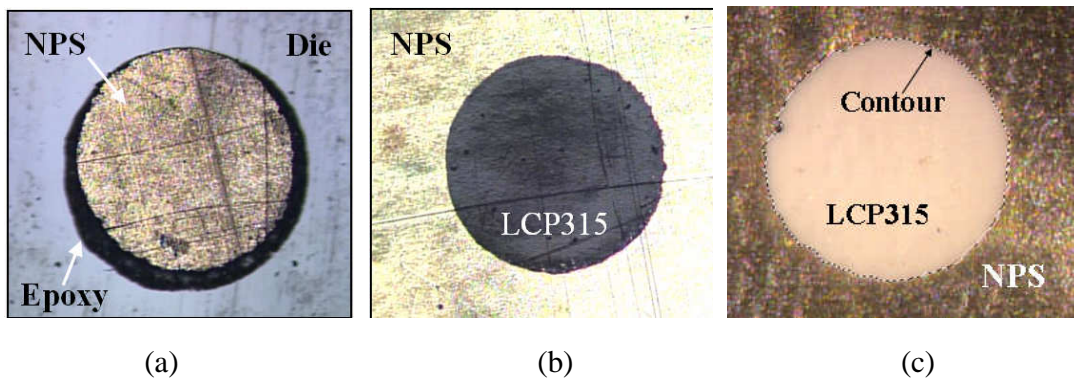
Figure 5.5 Fracture Surface: (a) NPS detached from LCP315 substrate (b) LCP315 surface exposure after interfacial fracture

5.2.5 FEM Analysis

The finite element method (FEM) is used to model the MBST and to find the average tensile and shear stresses as shown in Figure 5.6. Inset is the cross-section view of the real MBST specimen. The bottom surface of the metal substrate is fixed and all 6 degrees of freedom are assigned to be zero. All materials are assumed to be elastic and isotropic, and all material data are given in Table 5.1. The volume around the fracture area has a finer mesh, and the region far away from the center has a coarse mesh. Stress singularity takes place in the FEM analysis at the intersection of the interface and the free edge. The tensile stress value at this position significantly depends on mesh size. From a convergence study, 132,503 nodes and 130,581 elements are used in this analysis, as it provides converging tensile stress value as shown in Figure 5.7.
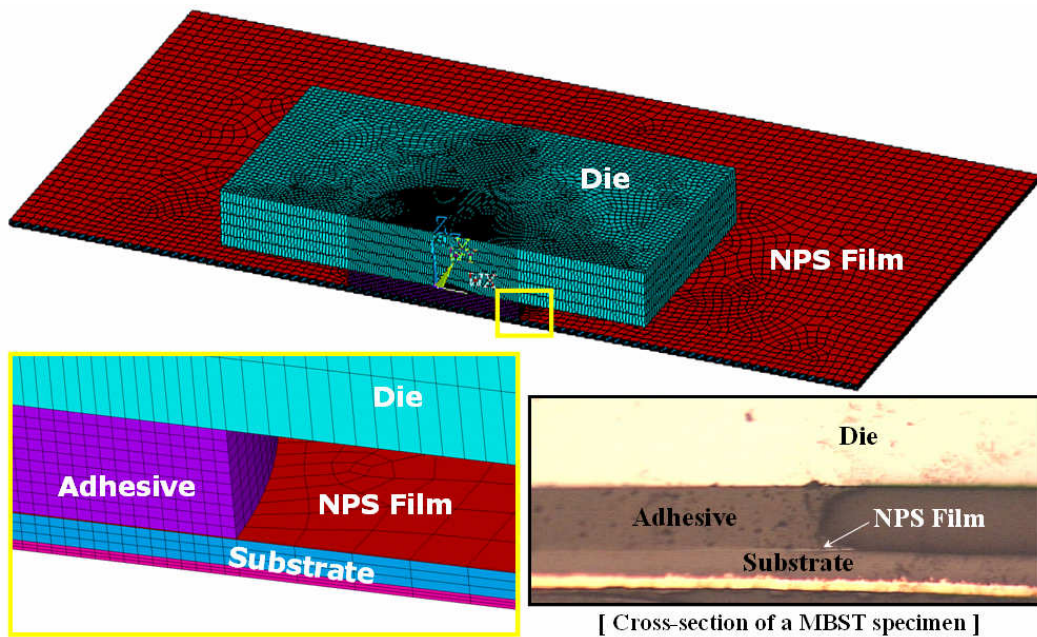
Figure 5.6 FEM modeling for MBST
(Real mesh is much denser.)
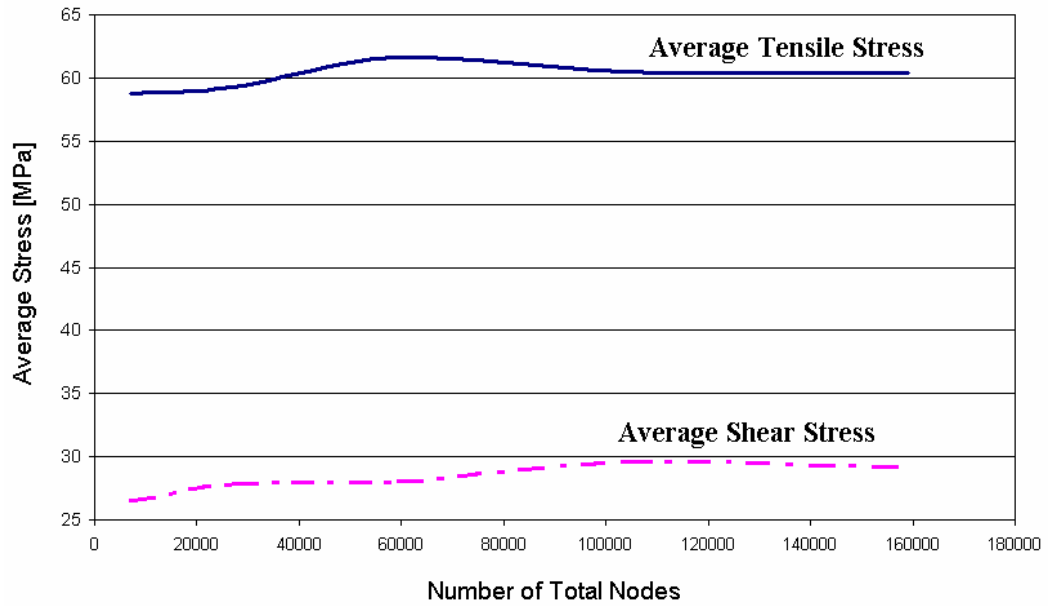
Figure 5.7 Convergence Study

Table 5.1 Data used in FEM calculations (Howatson, 1991)

Notation	Material	Material Property	Young's Modulus [GPa]	Poison's ratio	CTE [ppm/^{o}C]	Nominal Thickness [um]
Die	Silicon (100)	Elastic, isotropic	130	0.28	2.6(0°C) 3.22(127°C) 3.8(327°C)	675
Adhesive	Epoxy	Elastic, isotropic	4.2	0.34	62(25°C), 197(119°C)	200
Thin Film	Silver	Elastic, isotropic	83	0.37	19	2
Substrate	LCP315	Elastic, anisotropic	2.255	0.3	17(x, y) 150 (z)	50
	Kapton HN	Elastic, isotropic	2.8	0.34	20	125
	Copper	Elastic, isotropic	127	0.34	17	500
	Aluminum	Elastic, isotropic	70	0.35	23.1	500
	Si3N4	Elastic, isotropic	310	0.27	3.3	2.5

5.2.6 Interfacial Fracture Criterion

The number of stress components that contribute to interfacial fracture is only 3 as shown in Figure 5.8, while 6 components contribute to bulk material fracture. Moreover, it should be noted that compressive normal stress does not contribute to interfacial facture because it tends to close cracks. Thus, a conventional bulk material fracture criterion such as the Von Mises or the Tresca criterion cannot be used as an interfacial fracture criterion. The interfacial fracture criterion as in Equation (5.2), which was originated in composite laminate fracture, is used as the thin film interfacial fracture criterion in this study (Yi, 2000, Kim 1984, Hunt 1993, Fan 2005). The interfacial tensile bond strength, Z, is defined as the interfacial bond strength at which the interfacial fracture occurs when it is under the pure tensile loading condition. The interfacial shear bond strength, S, is also defined as the interfacial bond strength at which the interfacial fracture occurs when it is under the pure shear loading condition. In this criterion, the interfacial fracture initiates when the interface damage index (F) is equal to or larger than 1.
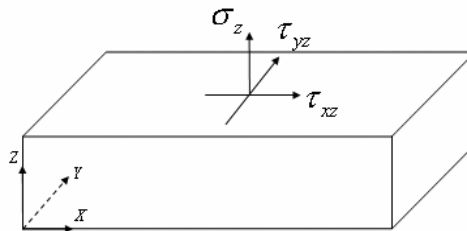
Figure 5.8 Interfacial Stress Components

$$F = \left(\frac{\bar{\sigma}}{Z}\right)^2 + \left(\frac{\bar{\tau}}{S}\right)^2 \geq 1.0 \qquad (5.2)$$

where F is interface damage index, $\bar{\sigma}$ is average tensile stress and equals $\bar{\sigma}_z$, $\bar{\tau}$ is average shear stress and equals $\sqrt{\tau_{xz}^2 + \tau_{yz}^2}$, Z is interfacial bond strength in tension, and S is interfacial bond strength in shear.

Using this criterion, the Z and S values can be found from two different loading conditions that generate two different sets of $\bar{\sigma}$ and $\bar{\tau}$. The $\bar{\sigma}$ and $\bar{\tau}$ are calculated from finite element stress analysis using Equation (5.3).

$$\bar{\sigma} = \frac{1}{r_o} \int_0^{r_o} \sigma \, dr \, , \quad \bar{\tau} = \frac{1}{r_o} \int_0^{r_o} \tau \, dr \tag{5.3}$$

where r_o is a critical length.

In order to take stress averaging, the critical length, r_o, needs to be determined. The critical length originates from the concept that the whole fracture area does not contribute to the delamination initiation and growth, but a certain area or length does, just as a critical distance contributes to delamination in a notched specimen. Thus, the critical length can be defined as the length over which the interface must be critically stressed in order to get a crack of sufficient size to initiate delamination (Sun, 1998). Many researchers have studied the critical length and they determined that 0.25mm from the edge provides the best fit (Yi, 2000, Kim 1984, Hunt 1993, Fan 2005).

5.2.7 Kendall Model

Once the interfacial bond strength in tensile, Z, is found from the interfacial fracture criterion, the Z can be used for estimating the fracture force in the pull-off test through Kendall model. Kendall developed an expression for the pull-off force required to detach a rigid cylinder bonded to a thin elastomeric coating on a stiff substrate (Kendall, 1971). The total energy, U_T, in the system is composed of three terms, the surface energy, U_S, the stored elastic energy, U_E, in the deformed material, and the

potential energy, U_P, in the applied load. The U_T for multiple coating is obtained by adding the energy terms, U_E+U_P, for each layer, which results in Equation (5.4) (Kohl, 1999):

$$U_T = -\pi a^2 G_a - \sum_i \frac{P^2 t_i}{2\pi K_i a^2} \qquad (5.4)$$

where P is normal force in N, ti is the thickness of each elastomeric layer in um, Ga is interfacial fracture energy at the fracture interface in J, K_i is the bulk modulus in MPa, and a is contact radius in um.

Under the assumption of linear elastic fracture mechanics, Griffith failure criterion, Equation (5.5), can be applied to Equation (5.4), which results in Equation (5.6).

$$\frac{dU_T}{da} \geq 0 \qquad (5.5)$$

$$P = \pi a^2 \sqrt{2 G_a / \sum_i \frac{t_i}{K_i}} \qquad (5.6)$$

where K is bulk modulus in MPa and equals $E/3(1-2\nu)$.

The normal force P can be obtained using FEM analysis for the Kendall model configuration as shown in Figure 5.9 by finding the force that generates the average tensile stress of Z at the fracture interface. In order to find the normal force P, first apply a unit load (1N) and calculate the average tensile stress (Z_1) under the unit load. Then, P will be obtained by simply calculating the ratio Z/Z_1. For example, for the button dimension of D=1963um and h=224um, the average tensile stress Z_1 was calculated as 0.349MPa for NPS-LCP315 adhesion under the unit load 1N. From the interfacial tensile bond strength of 48.5 MPa for the NPS-LCP315 adhesion, the normal force P can be obtained by the ratio of Z/Z_1 x 1N=48.5/0.349=139 N. Note that Z is very close to $P/\pi a^2$, but is not exactly the same. When the normal force is calculated

from $Z \times \pi a^2$, the P will be $48.5 \times 3.14 \times (1.963/2)^\wedge 2 = 146N$. Finally, through the Kendall model, the Z, thus P, is used to find the interfacial fracture energy, Ga, which is the energy required to separate the two materials bonded.

$$P = Z \cdot \pi a^2$$

Die (Rigid)

NPS Film | Adhesive

Substrate (Rigid)

Force

(a)   (b)
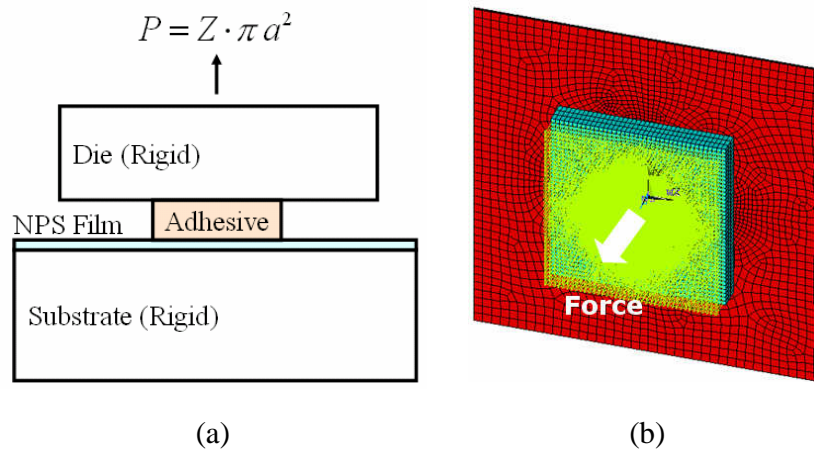
Figure 5.9 Kendall Model: (a) Kendall model configuration (b) FEM model

5.3 Results and Discussion

5.3.1 Stress Distributions

Figure 5.10 shows a representative normalized mechanical tensile and shear stress distribution of a Full Die MBST along the center line of LCP315 and NPS interface from the edge. Mechanical force equilibrium can be used to demonstrate in part that the critical length of 0.25mm has been selected appropriately. From the free body diagram of Figure 5.4(a), the relationship between the average shear stress ($\bar{\tau}$) and the fracture force divided by fracture area should satisfy the force balance in the x-direction as in Equation (5.7). Considering that the cohesive fracture force corresponds to about 3.3% of fracture force as discussed in section 5.2.3, the relationship of Equation (5.7) can be developed. Table 5.2 shows the statistics of the calculated average mechanical shear stress ($\bar{\tau}$) from FEM and the measured fracture force divided by fracture area for twenty samples. The

two values are very close to each other, which partly assures that the critical length 0.25mm is appropriate.
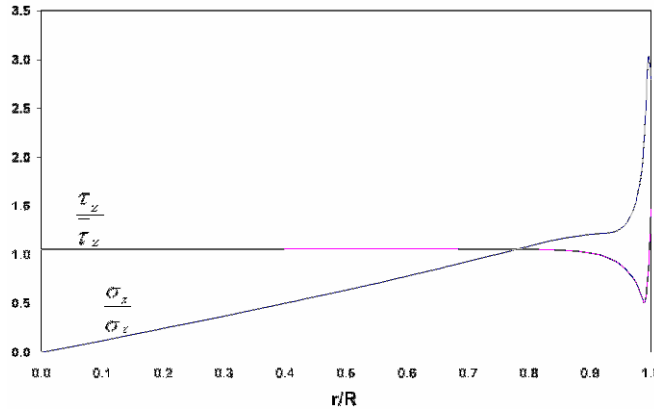
Figure 5.10 Representative Mechanical Stress Distributions for Full Die Shear

$$\sum F_x = 0 \; ; \; F_i + F_C = F_f$$

$$\Rightarrow \; \frac{F_i}{A} + \frac{F_C}{A} = \frac{F_f}{A} \; \Rightarrow \overline{\tau} + \frac{F_f \times 3.3\%}{A} = \frac{F_f}{A} \Rightarrow \overline{\tau} = \frac{F_f}{A} \times 96.7\% \quad (5.7)$$

Table 5.2 Average Mechanical Shear Stress and Fracture Force divided Fracture Area

	Calculated Average Mechanical Shear Stress	Measured Fracture Force divided by Fracture Area × 96.7%
Mean [MPa]	20.3	21.5
Standard deviation [MPa]	2.6	2.7

5.3.2 Thermal Residual Stress Distributions

In addition to mechanical stresses, thermally induced residual stresses due to cooling down after sintering NPS and epoxy curing are calculated. Figure 5.10 shows the residual stress distribution at the NPS-LCP315 interface for 10x10 mm^2 NPS film after sintering and before epoxy curing. The temperature change of -205℃ is applied in this analysis because of the actual difference between 230℃ and room temperature (25℃).

As shown, the central area, where the test specimens are made from, has negligible normal stress (<0.1 KPa) and shear stress (<0.1 MPa).

However, the residual stresses generated after epoxy curing process are not negligible. Figure 5.12 shows a representative residual stress distribution at the fracture interface between LCP315 and NPS. The magnitudes of normal stress and shear stress within the critical length of 0.25mm from the edge and at the NPS-LCP315 interface are about -3.8 MPa and 11.1 MPa, respectively, for this particular case. It should be noted that the residual normal stress is compressive, which suggests that average normal stress value will be larger unless the thermal residual stresses are considered.

5.3.3 Fracture Initiation Location

Among the three loading configurations, only the full die shear has a clear fracture initiation location, which is the right front edge of the applied force location, because the maximum tensile stress location coincides with the maximum shear stress location at the fracture interface as shown in Figure 5.13. However, for the other two loading configurations, the maximum shear stress location is different from the maximum tensile stress location as indicated in Figure 5.14 and 5.15. In these figures, all compressive normal stress components were taken as zero because compressive normal stress does not contribute to interfacial fracture. Finding the fracture initiation location for Mid Die and Large Die Shear configuration is necessary in order to take an average stress within the critical length of 0.25mm from each fracture initiation location. According to the interfacial fracture criterion, the fracture initiation location depends on Z and S, which are unknown at present, but not at the maximum tensile or shear stress location. This means that the relative magnitude between $\bar{\sigma}$ and $\bar{\tau}$ does not determine where fracture is likely to initiate.
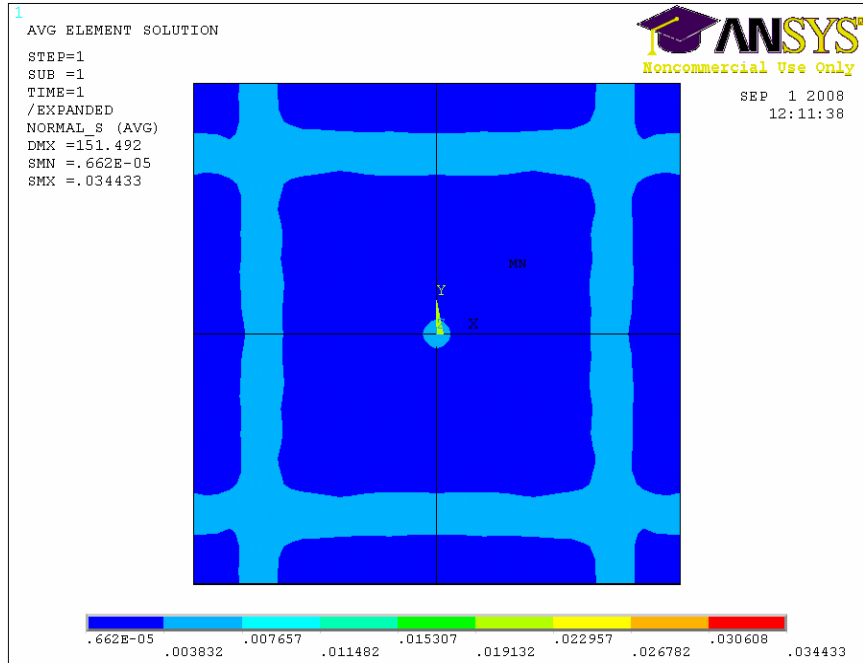
(a)
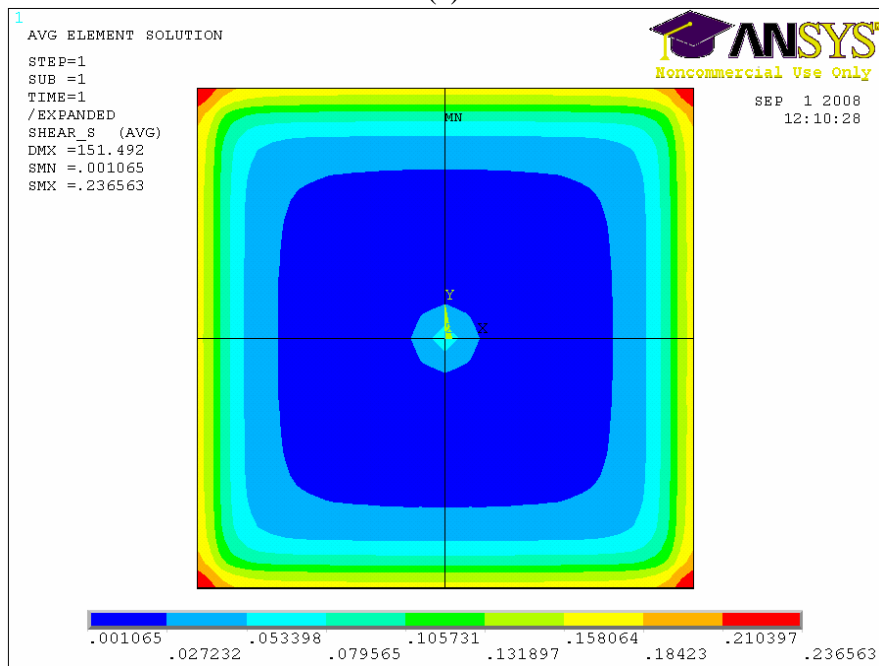
(b)

Figure 5.11 Residual stress distributions at the LCP315/NPS interface after NPS sintering without die attach (a) Normal Stress (b) Shear Stress
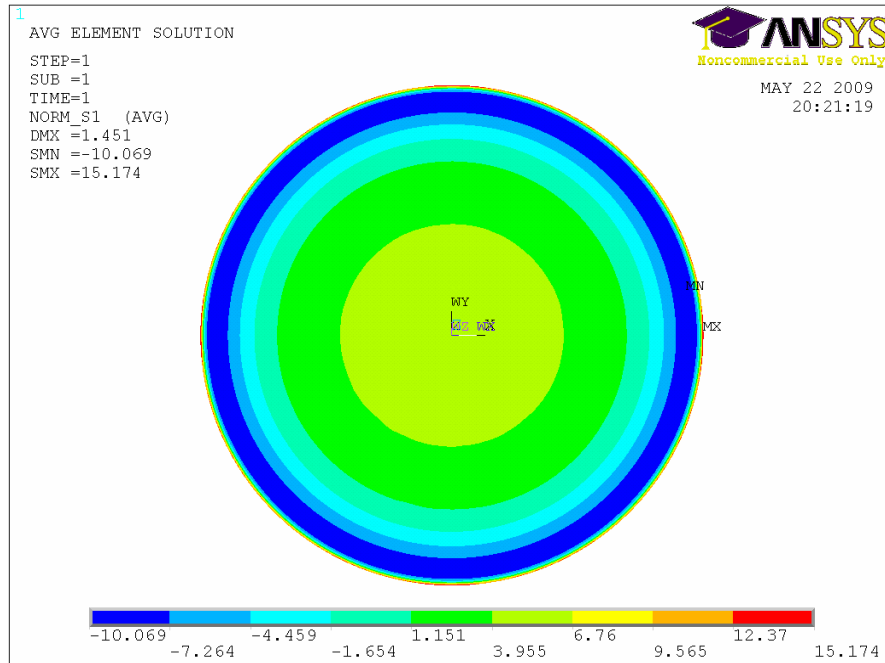
(a)
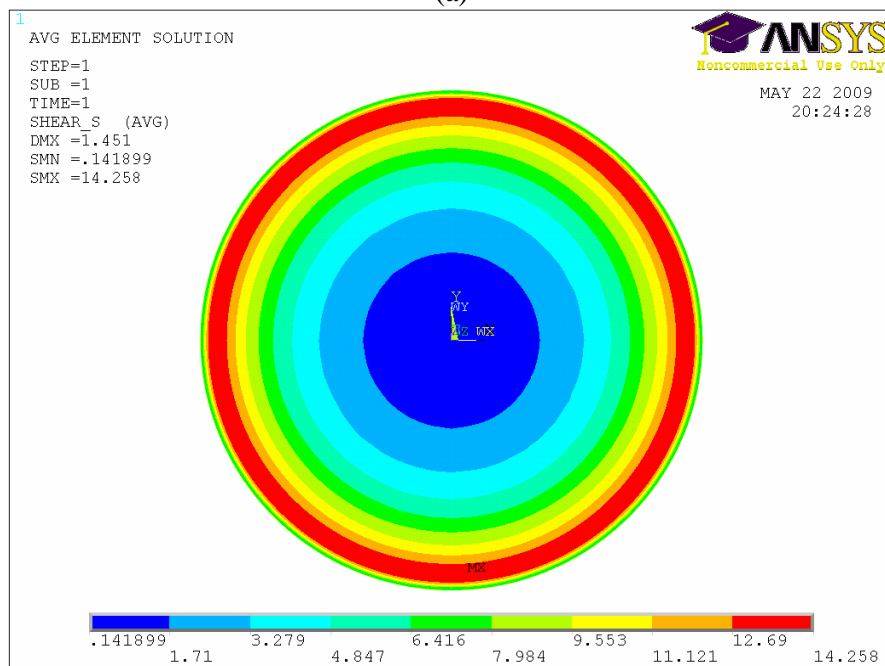
(b)

Figure 5.12 Residual stress distributions over the adhesive area only at the LCP315/NPS
interface after epoxy cure (D=1866 um, h=210 um) (a) Normal Stress (b) Shear Stress
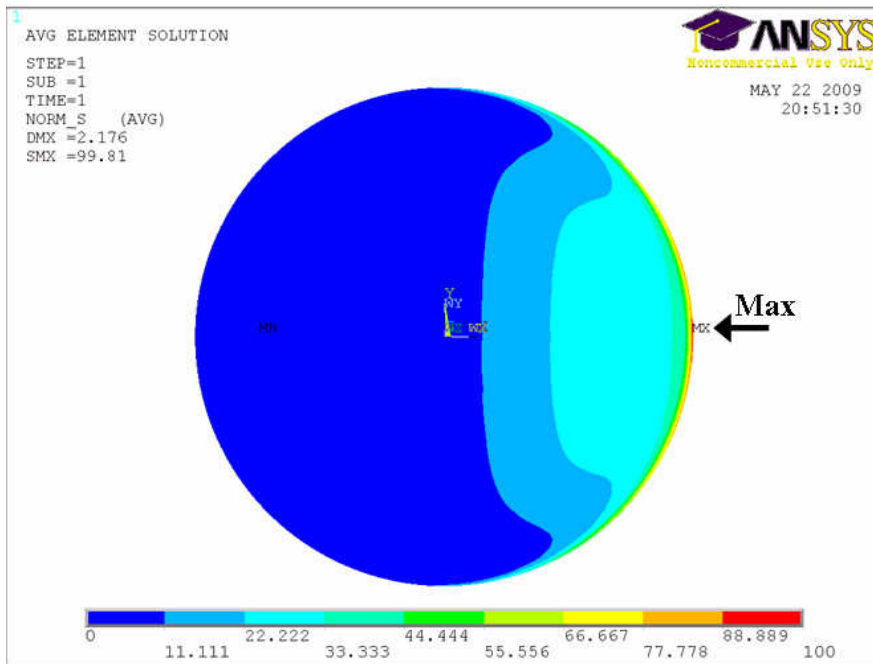
(a)
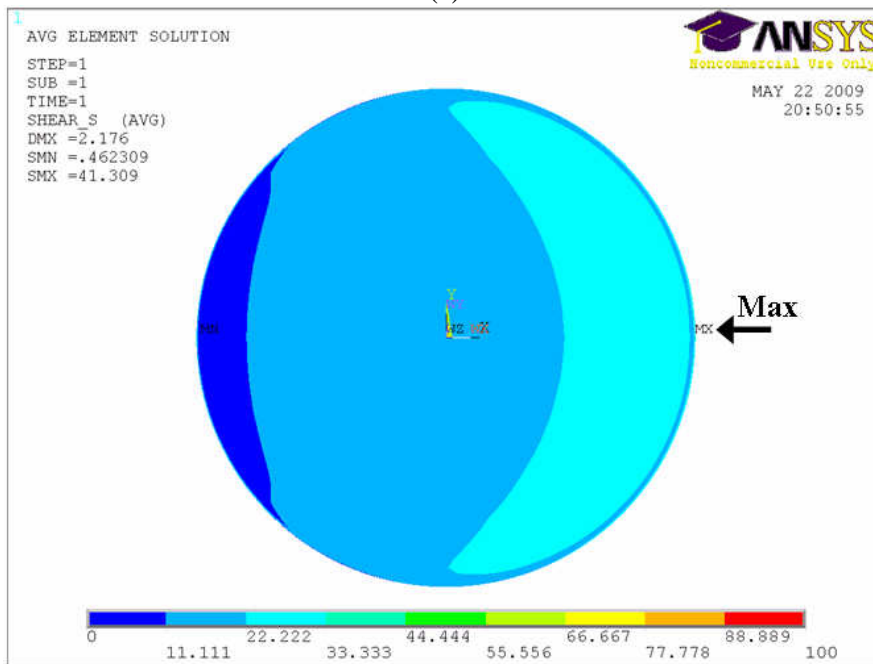
(b)

Figure 5.13 Resultant Stress Distribution over the adhesive area only for Full Die Shear
(D=1866 um, h=210 um, F_f =57.9N) (a) Normal Stress (Compression is regarded as zero)
(b) Shear Stress
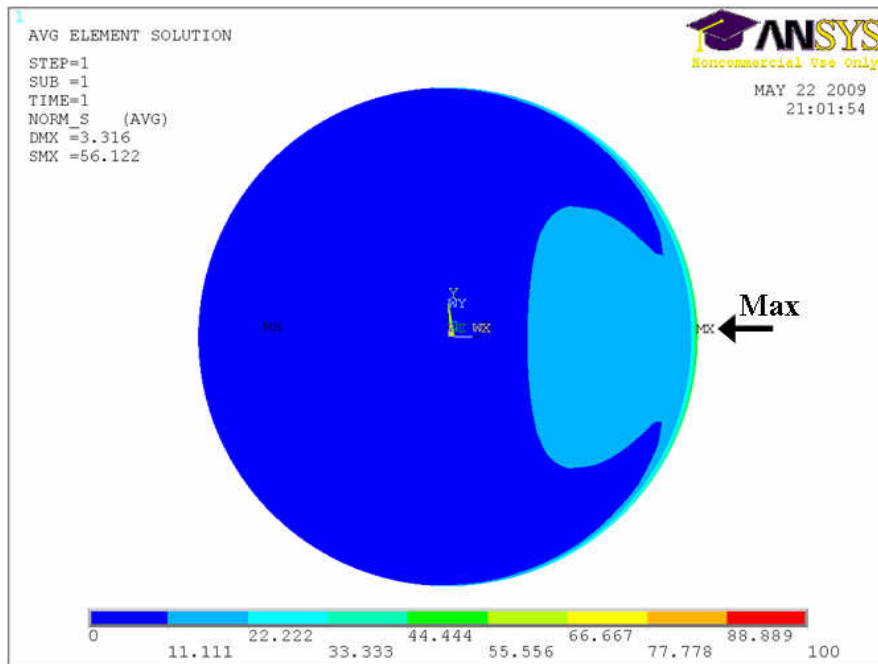
(a)
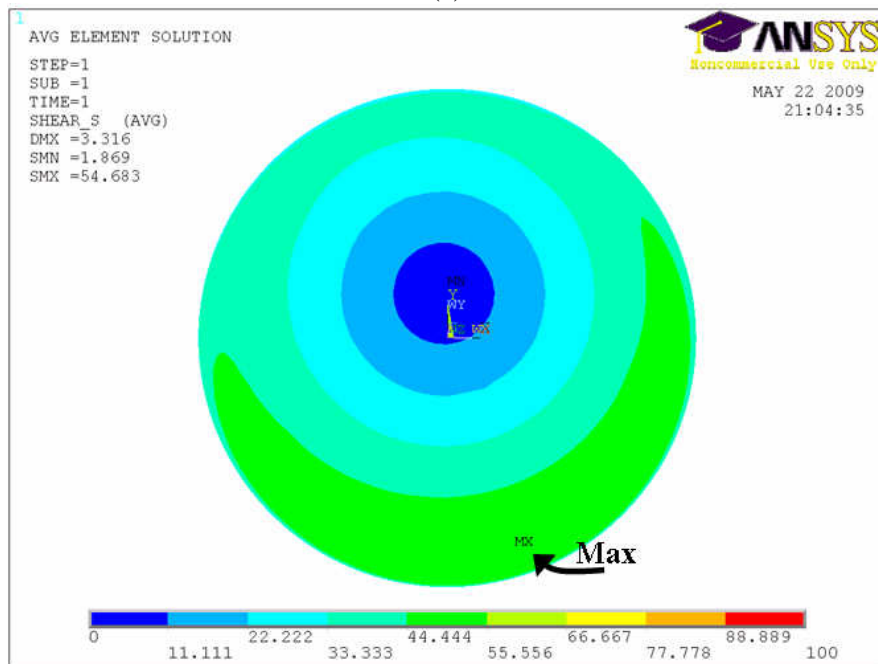
(b)

Figure 5.14 Resultant Stress Distribution over the adhesive area only for Mid Die Shear (D=1854 um, h=202 um, F_f =28.9 N) (a) Normal Stress (Compression is regarded as zero) (b) Shear Stress
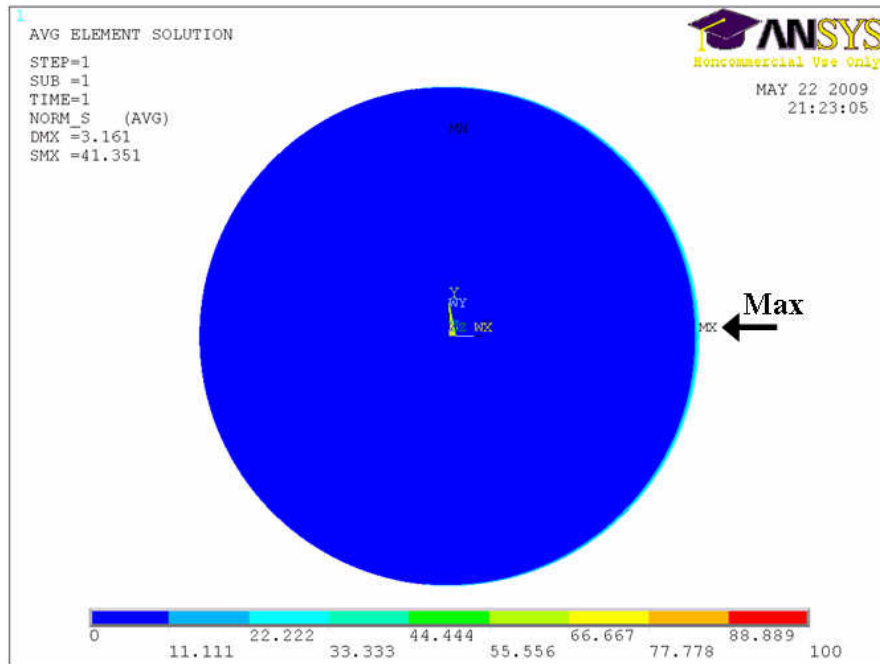
(a)
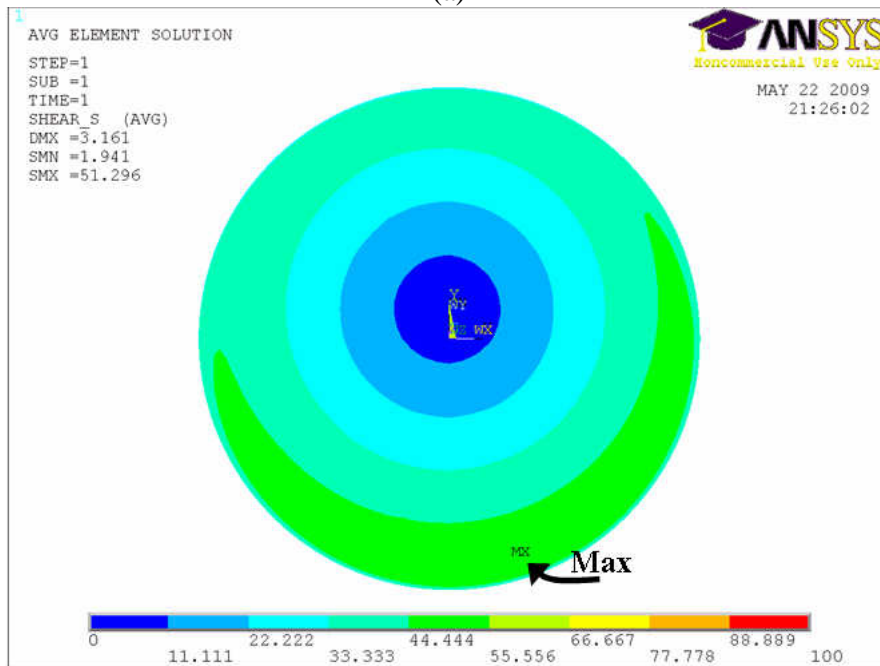
(b)

Figure 5.15 Resultant Stress Distribution over the adhesive area only for Large Die Shear
(D=2391 um, h=229 um, F_f=29.3 N) (a) Normal stress (Compression is regarded as zero)
(b) Shear Stress

Figure 5.16(a) describes the sequence for finding the fracture initiation location. First, take the average tensile and shear stresses at an angle of 0° according to the angle convention in the Figure 5.16(b). Then, calculate $Z_0{}^o$ and $S_0{}^o$ in conjunction with the data from the Full Die Shear test, in which the fracture initiation location is known. Take the average tensile and shear stresses at all angles from 0° to 90° and calculate interface damage index using $Z_0{}^o$ and $S_0{}^o$ for all angles. Then, repeat this procedure to find $Z_k{}^o$ and $S_k{}^o$ for all angles from 0° to 90°. The angle where the maximum value of F is generated will be the fracture initiation location. Repeating this sequence for all other samples will provide each fracture initiation angle.
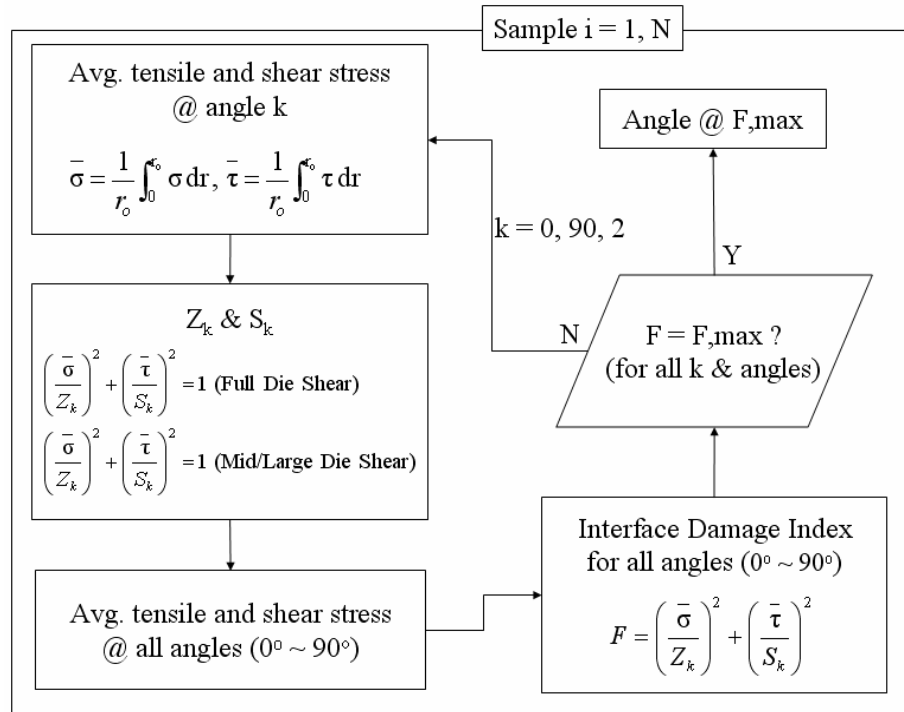
(a)
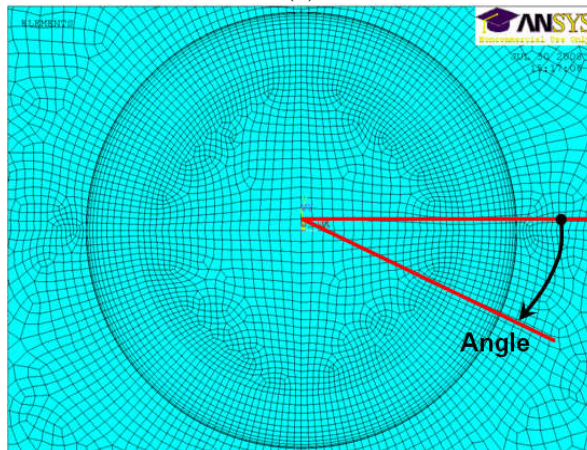
(b)

Figure 5.16 Procedure for finding fracture initiation location for Mid and Large Die Configuration (a) Flow Chart (b) Angle Convention

The comparison of S and Z between three different angles as summarized in Table 5.3 shows that there is no significant difference in S and Z between the three

different locations. For consistency, the average angle where fracture is likely to initiate for Mid Die (30°) and Large Die (72°) will be taken in this study.

Table 5.3 Comparison of S and Z from different angles [MPa]

Angle	Die Shear Configuration	$\bar{\sigma}$	$\bar{\tau}$	S	Z
0°	Full Die	38.7	30.1	45.4	51.4
	Mid Die	20.0	41.8		
	Large Die	5.6	45.1		
Each Max. Angle	Full Die	38.7	30.1	48.7	47.4
	Mid Die	17.4	45.3		
	Large Die	0.5	48.7		
Avg. Max. Angle	Full Die	38.7	30.1	48.4	48.1
	Mid Die (30°)	17.7	45.0		
	Large Die (72°)	0.0	48.4		

5.3.4 Interfacial Bond Strength

Table 5.4 shows the calculated average tensile and shear stresses for the three different loading conditions. By plotting these stresses on the average tensile-shear stress graph as shown in Figure 5.17, the interfacial bond strength in tension and in shear can be found. The interfacial bond strengths in tension (Z) and in shear (S) for LCP and NPS adhesion interface are 48.5 MPa and 48.4 MPa, respectively. It should be noted that the Z in this plot is the mean interfacial bond strength in tension, Z_{50}, which means the interfacial bond strength in tension at which 50% of samples will be fractured. The two outer lines in Figure 5.17 form an interfacial fracture band that covers 95% of the samples. It should be emphasized that Z and S are characteristic interfacial properties, and thus, are independent of specimen geometry.

Table 5.4 Average Tensile and Shear Stresses and their standard deviations [MPa]

	Full Die MBST		Mid Die MBST		Large Die MBST	
	$\bar{\sigma}$	$\bar{\tau}$	$\bar{\sigma}$	$\bar{\tau}$	$\bar{\sigma}$	$\bar{\tau}$
Average	38.7	30.1	17.7	45.0	0.0	48.4
Standard deviation	4.9	2.1	2.5	2.8	0.0	4.5
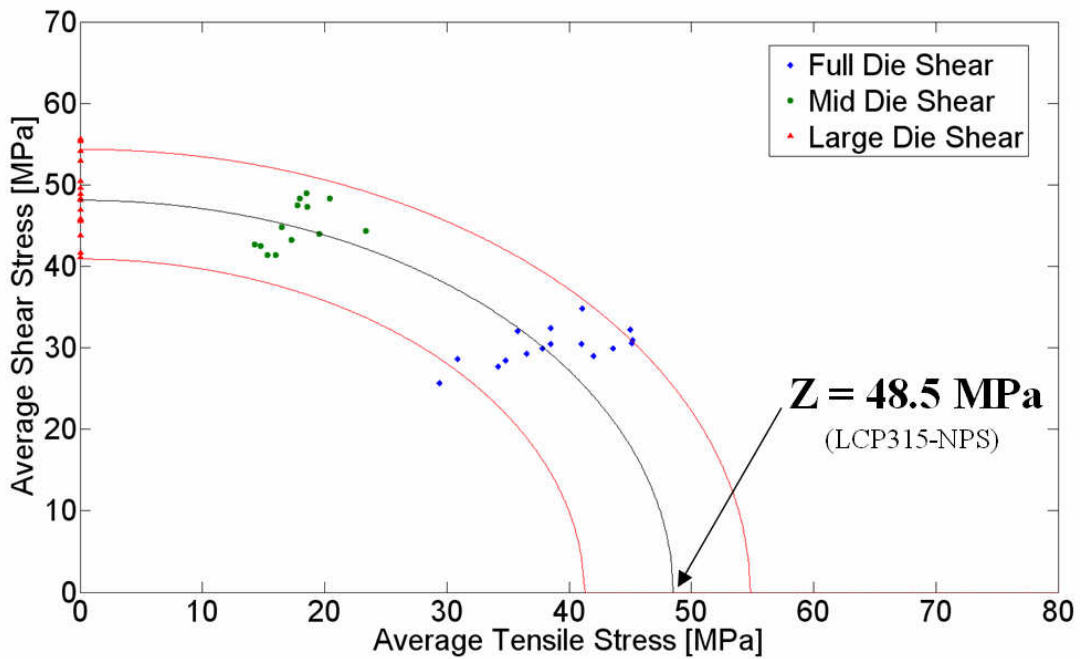
Figure 5.17 Average tensile - shear stress plot for LCP315-NPS adhesion

5.3.5 Adhesion Strengths for test materials

Using the MBST, the interfacial bond strengths in tension for all the test materials are measured and summarized in Tables 5.5 and 5.6. Among the organic materials, Kapton KJ, SS 415, and Teflon FEP are not included because their fracture did not take place at the interface between NPS and substrate. Kapton KJ and SS 415 showed their fracture modes at the interface of epoxy adhesive and NPS film. The Teflon FEP specimen for adhesion strength measurement using MBST was not available because the NPS film was not formed on the Teflon FEP surface. Due to the low surface energy of

Teflon FEP, NPS does not spread well on the surface, resulting in NPS islands rather than NPS film as shown in Figure 5.18.
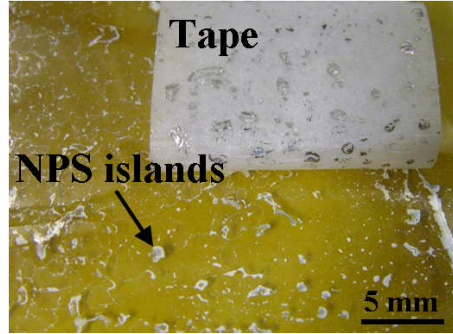
Figure 5.18 NPS islands on Teflon FEP

In these tables, the measured values are represented by mean ± standard deviation (mean ± σ), which corresponds to 68.3% (±1σ) confidence interval. Since the Z and S are derived quantities from the measured stress values for Full Die and Mid Die test conditions, the uncertainties of these quantities are needed to be computed. For the calculation of the uncertainty, Δg, of the quantity g, which is a function of n measured quantities x_i, g=f(x_1, x_2, x_3,...,x_n), a widely used approach as in Equation (5.8) is used.

$$\Delta g = \sqrt{\sum_{i=1}^{n}\left(\frac{\partial f}{\partial x_i}\Delta x_i\right)^2} \tag{5.8}$$

where $\dfrac{\partial f}{\partial x_i}$ is the partial derivative of function f with respect to x_i and Δx_i is the uncertainty in the measured quantity x_i.

From the interfacial fracture criterion, Equation (5.2), two different sets of tensile and shear stresses from two different loading conditions should satisfy Equation (5.9).

$$\left(\frac{\overline{\sigma_1}}{Z}\right)^2 + \left(\frac{\overline{\tau_1}}{S}\right)^2 = 1 \;\; \& \;\; \left(\frac{\overline{\sigma_2}}{Z}\right)^2 + \left(\frac{\overline{\tau_2}}{S}\right)^2 = 1 \tag{5.9}$$

where $\bar{\sigma}_i$, $\bar{\tau}_i$ are the average tensile and shear stress of loading condition i, respectively.

The interfacial tensile bond stress and the interfacial shear bond strength can be written as a function of the average stress components as Equation (5.10).

$$S = \sqrt{\frac{\bar{\sigma}_1^2 \bar{\tau}_2^2 - \bar{\sigma}_2^2 \bar{\tau}_1^2}{\bar{\sigma}_1^2 - \bar{\sigma}_2^2}} \quad \& \quad Z = \sqrt{\frac{\bar{\sigma}_1^2 S^2}{S^2 - \bar{\tau}_1^2}} \tag{5.10}$$

Thus, the uncertainties in the S and Z can be defined as Equation (5.11) with a 68.3% confidence level. The partial derivatives in Equation (5.11) are calculated using Matlab, and they are summarized in Appendix B. All the calculations in Equation (5.11) were performed using Matlab.

$$\Delta S = \sqrt{\left(\frac{\partial S}{\partial \bar{\sigma}_1}\Delta\bar{\sigma}_1\right)^2 + \left(\frac{\partial S}{\partial \bar{\tau}_1}\Delta\bar{\tau}_1\right)^2 + \left(\frac{\partial S}{\partial \bar{\sigma}_2}\Delta\bar{\sigma}_2\right)^2 + \left(\frac{\partial S}{\partial \bar{\tau}_2}\Delta\bar{\tau}_2\right)^2}$$
$$\Delta Z = \sqrt{\left(\frac{\partial Z}{\partial \bar{\sigma}_1}\Delta\bar{\sigma}_1\right)^2 + \left(\frac{\partial Z}{\partial \bar{\tau}_1}\Delta\bar{\tau}_1\right)^2 + \left(\frac{\partial Z}{\partial S}\Delta S\right)^2} \tag{5.11}$$

Table 5.5 Interfacial adhesion strengths (mean ± σ) for organic substrate materials

Substrates	Die Configuration	$\bar{\sigma}$	$\bar{\tau}$	S	Z	Fracture Mode
Kapton HN	Full Die	14.2±2.3	4.0±1.6	9.3±2.8	15.7±3.1	Interface
	Mid Die	4.4±1.0	9.0±2.6			
LCP 315	Full Die	38.7±4.4	30.1±3.9	48.1±4.9	48.5±8.4	Interface
	Mid Die	17.7±2.2	45.0±4.0			
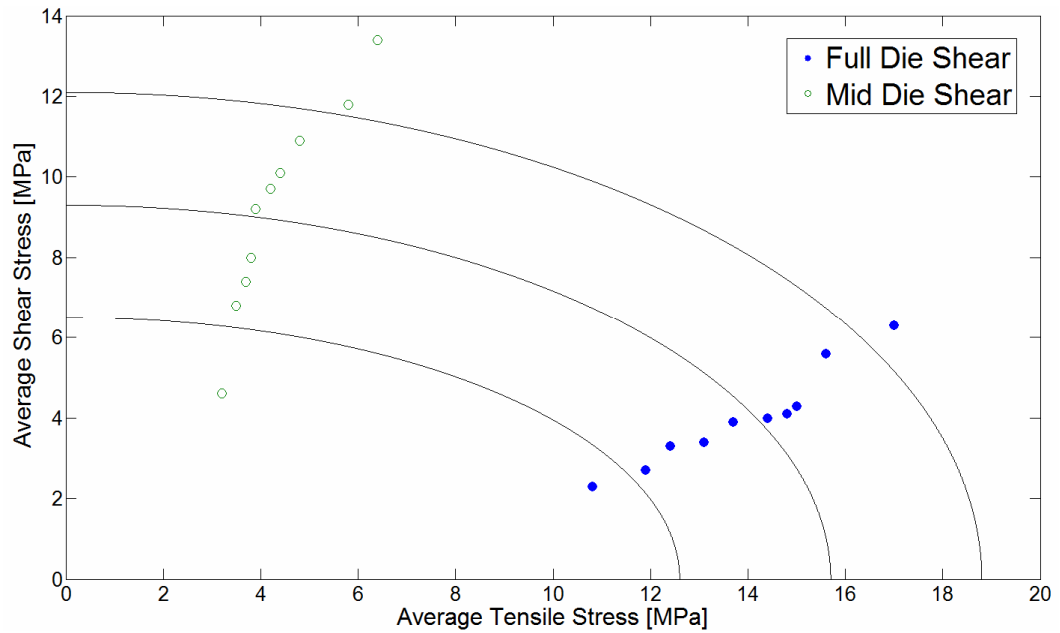
Figure 5.19 Average tensile - shear stress plot for HN-NPS adhesion

Table 5.6 Interfacial adhesion strengths (mean ± σ) for inorganic substrate materials

Substrates	Die Configuration	$\bar{\sigma}$	$\bar{\tau}$	S	Z	Fracture Mode
Cu2O	Full Die	10.0±3.1	5.6±2.5	11.1±4.3	11.6±4.4	Interface
	Mid Die	3.8±1.7	10.5±3.8			
Al2O3	Full Die	9.6±2.3	4.9±2.4	18.8±5.5	9.9±2.5	Interface
	Mid Die	5.5±1.9	15.6±3.4			
Si3N4	Full Die	9.8±2.8	4.7±2.6	16.5±4.7	10.2±3.1	Interface
	Mid Die	5.4±1.8	14.0±3.0			
(etched) Al	Full Die	54.3±9.4	30.8±5.1	66.3±8.3	61.3±11.6	Interface
	Mid Die	22.0±3.0	61.9±7.1			
(etched) Cu	Full Die	67.5±9.0	36.5±6.5	91.0±11.4	73.7±10.7	Epoxy/NPS
	Mid Die	29.2±3.7	83.5±9.7			

(a) Cu2O-NPS
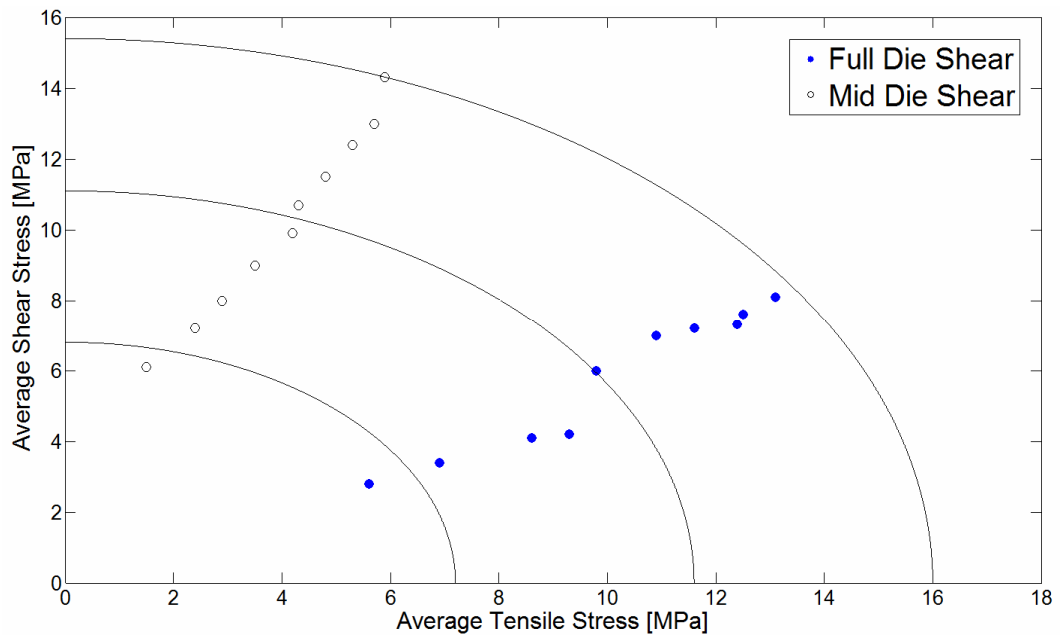
(b) Al2O3-NPS
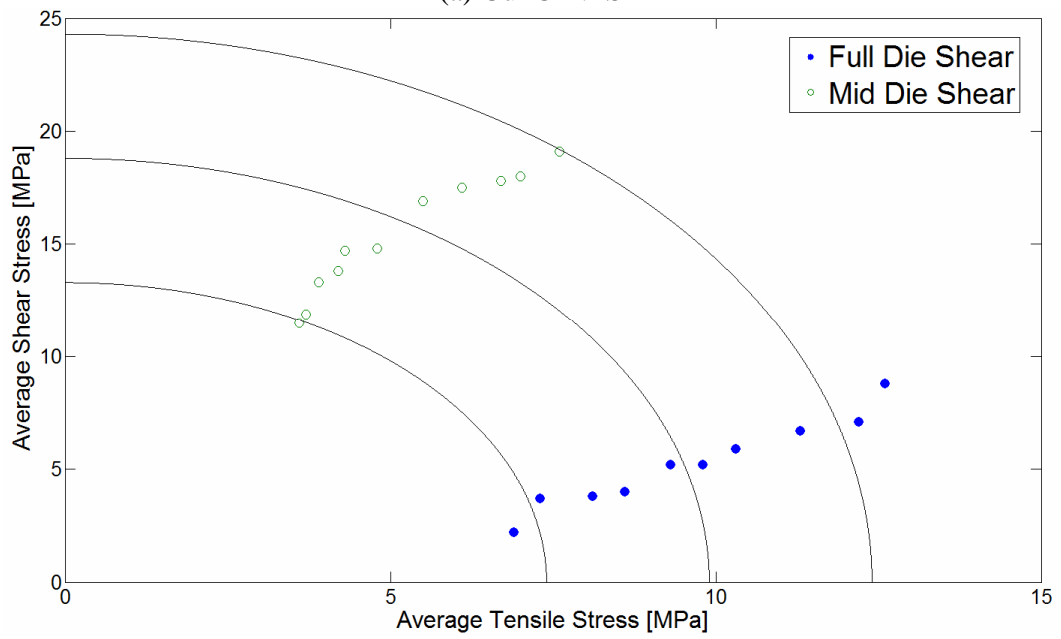
(c) Si3N4-NPS
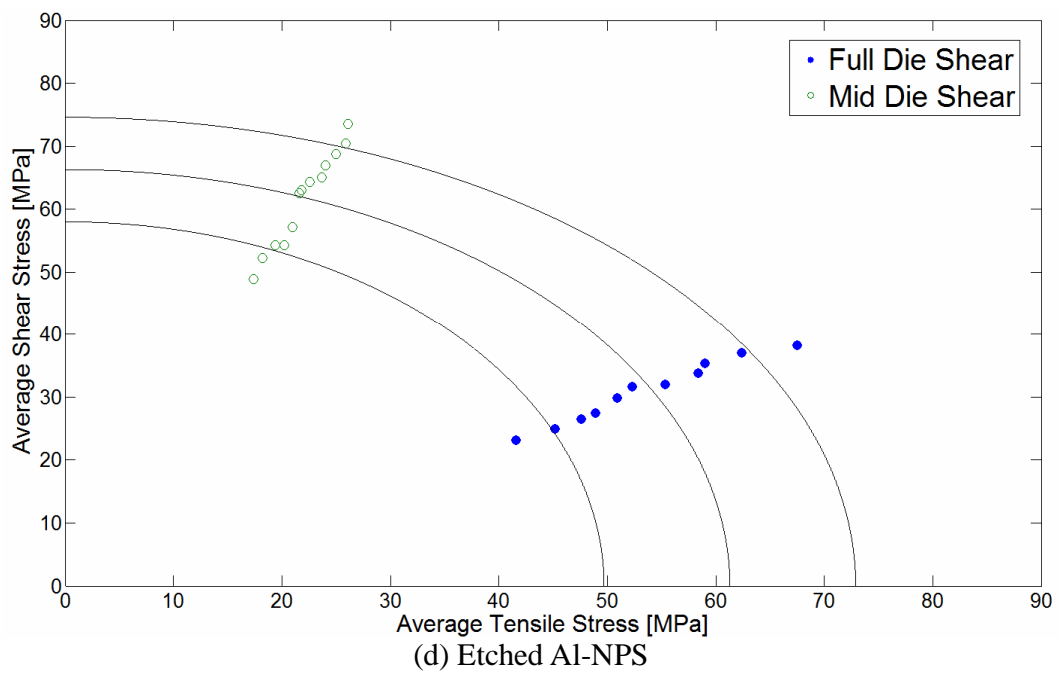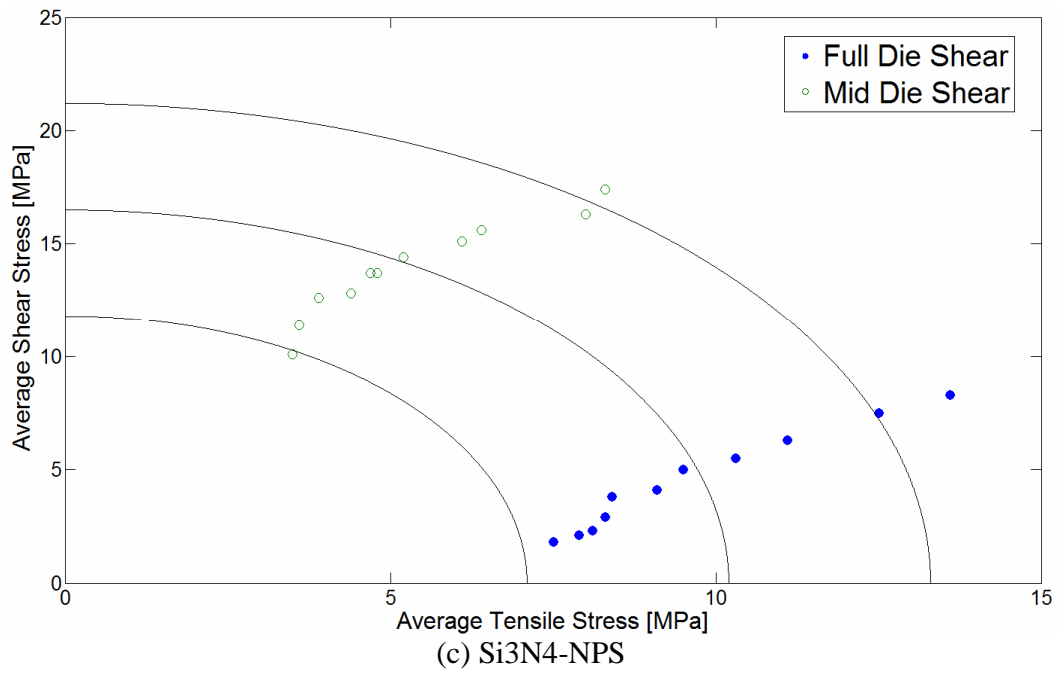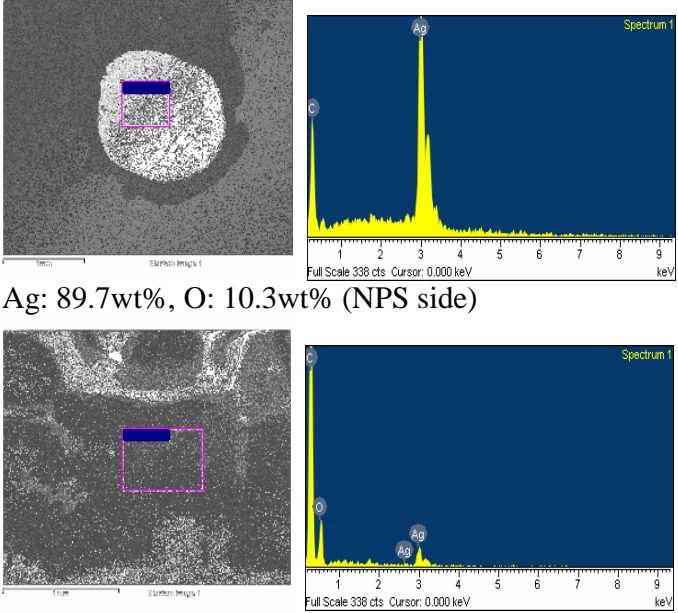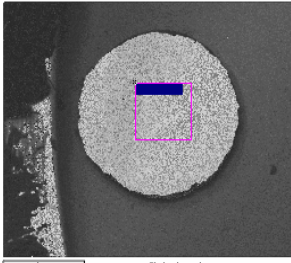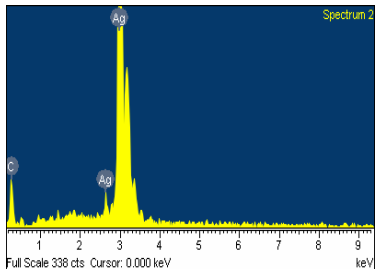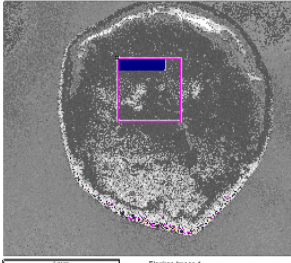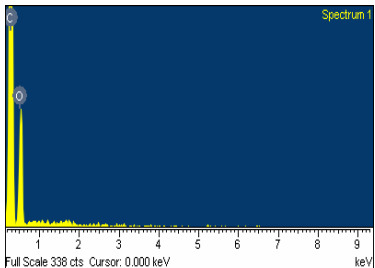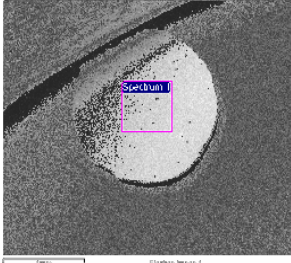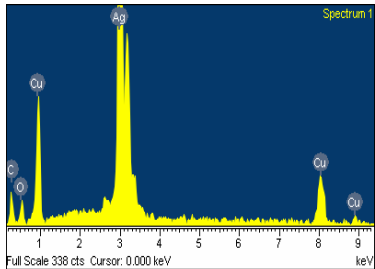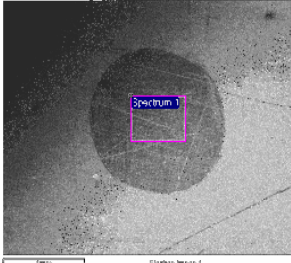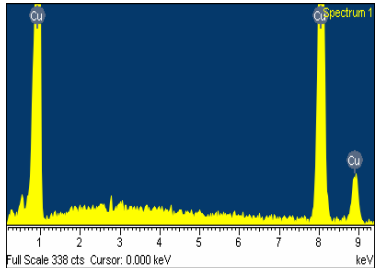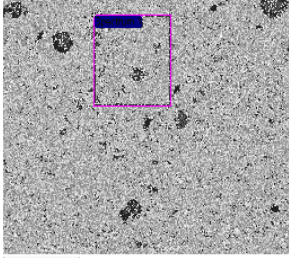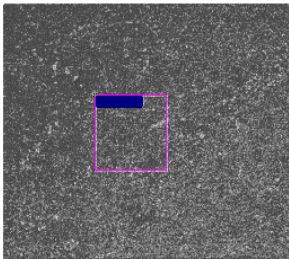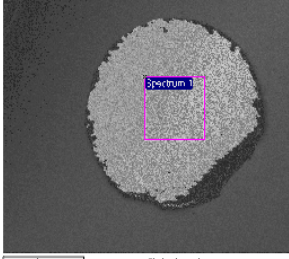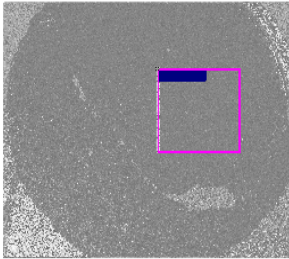
(d) Etched Al-NPS

Figure 5.20 Average tensile - shear stress plot for (a) Cu2O-NPS (b) Al2O3-NPS
(c) Si3N4-NPS (d) Etched Al-NPS adhesion
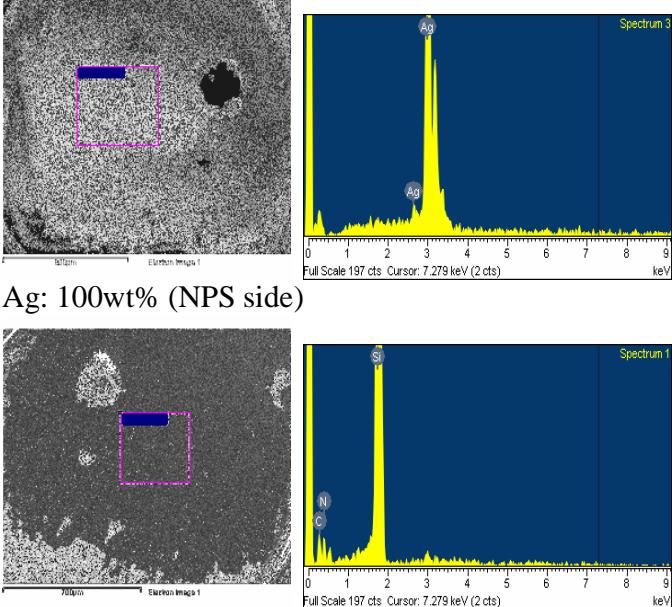
The fracture modes of NPS-substrates fracture are investigated using energy dispersive X-ray spectroscopy (EDX). MBST fracture samples were prepared, and they were air brushed before entering into the EDX chamber to remove any debris or dusts on the fracture surfaces of both NPS and substrate sides. The accelerating voltage of 10kV was used to take EDX data from the top surface to within about 1 um depth although this scanning depth varies with the materials tested. For the samples with severe surface charging, carbon coating using carbon coater was used. The carbon coating in sample preparation should not affect the EDX analysis, so carbon was excluded in the chemical composition analysis. The EDX test results for fracture mode analysis are summarized in Table 5.7.

Table 5.7 Fracture mode analysis

Substrate (Z)	Fracture Mode	EDX Analysis
Kapton HN (15.7 MPa)	Mostly NPS/HN interface	Ag: 89.7wt%, O: 10.3wt% (NPS side) O: 87.6wt%, Ag: 12.4wt% (Substrate side)

LCP 315 (48.5 MPa)	NPS/LCP315 interface	 Ag: 100wt% (NPS side) O:100wt% (Substrate side)
Cu2O (8.9)	Mostly NPS/Cu Interface	 Ag: 67.4wt%, Cu: 19.5wt%, O: 11.3wt% (NPS side) Cu: 100wt% (Substrate side)

Al2O3 (9.9 MPa)	Mostly NPS/Al interface	 Ag: 91.9wt%, O: 8.1wt% (NPS side) Al: 83.7wt%, O: 8.8wt%, Ag: 7.6wt% (Substrate side)
Etched Al (61.3 MPa)	NPS/Al interface	 Ag: 100wt% (NPS side) Al: 100wt% (Substrate side)

Si3N4 (10.2 MPa)	NPS/Si3N4 interface	 Ag: 100wt% (NPS side) Si: 70wt%, N:30wt% (Substrate side)

5.3.6 Interfacial Fracture Energy

The interfacial fracture energy of NPS/LCP315 interface can now be estimated based on the MBST test results. From Equation (5.6), the interfacial fracture energy can be written as in Equation (5.12) by assuming $Z \approx P/\pi a^2$ from Figure 5.9(a). The relative error introduced by this assumption is about 5.0% based on the calculation in section 5.2.7.

$$G_a \approx \frac{1}{2}Z^2 \sum_i \frac{t_i}{K_i} \tag{5.12}$$

where K is bulk modulus and equals $E/3(1-2\nu)$.

Using the measured interfacial tensile bond strength, Z, and the thickness and the bulk modulus of each materials used in MBST, the interfacial fracture energy of NPS and LCP315 interface can be calculated as summarized in Table 5.8. In this calculation, the approach in computing the error propagation was the same as that in section 5.3.5.

Table 5.8 Interfacial Fracture Energy of NPS/LCP315 interface

Materials	E [Mpa]	v	K [MPa]	t [um]	t/K [um/MPa]
Die	130000	0.28	98485	675.00	0.007
NPS	83000	0.37	106410	2.0	0.000
Epoxy	4200	0.34	4375	224±22	0.051±0.005
LCP315	2255	0.30	1879	50.0	0.027
				$\sum_i \dfrac{t_i}{K_i}$	0.085±0.005
Z [MPa]		48.5±8.4	Ga [J/m²]	99.8±35.1	

The interfacial fracture energy, Ga, 99.8±35.1 J/m², of NPS and LCP315 interface is comparable to those of other adhesion interfaces. The interfacial fracture energy of a very smooth ($R_a \sim 0.05$um) aluminum/epoxy interface was measured as 12 J/m² by Yao (2000). Gent (1990) measured the interfacial fracture energy of natural rubber molded in contact with a smooth aluminum plate and obtained a value of 35 J/m². Lee (2003) found that the interfacial fracture energy of EMC/Cu leadframe interface after oxidizing the copper surface was 80 ~ 100 J/m². Yu (2002) measured the interfacial fracture energy of Cu/Cr/Kapton H Polyimide system after using Ar^+ based RF plasma pretreated Polyimide to be almost 500 J/m².

Likewise, the interfacial fracture energy between NPS and all other substrate materials can be calculated, and they are tabulated in Tables 5.9-13. In these tables, Die and NPS data are omitted, but they are included in the calculation by assuming that they are the same as those in Table 5.8.

Table 5.9 Interfacial Fracture Energy of NPS/Kapton HN interface

Materials	E [Mpa]	v	K [MPa]	t [um]	t/K [um/MPa]
Epoxy	4200	0.34	4375	243±27	0.056±0.006
Kapton HN	2800	0.34	2917	125	0.043
				$\sum_i \dfrac{t_i}{K_i}$	0.105±0.006
Z [MPa]		15.7±3.1	Ga [J/m²]	13.0±5.16	

Table 5.10 Interfacial Fracture Energy of NPS/Aluminum interface

Materials	E [Mpa]	v	K [MPa]	t [um]	t/K [um/MPa]
Epoxy	4200	0.34	4375	222±13	0.051±0.003
Aluminum	70000	0.35	77778	500	0.006
				$\sum_i \dfrac{t_i}{K_i}$	0.058±0.003
Z [MPa]		61.3±11.6	Ga [J/m^2]	109.0±41.6	

Table 5.11 Interfacial Fracture Energy of NPS/Al2O3 interface

Materials	E [Mpa]	v	K [MPa]	t [um]	t/K [um/MPa]
Epoxy	4200	0.34	4375	224±22	0.051±0.003
Al2O3	*70000	0.35	77778	*500	0.006
				$\sum_i \dfrac{t_i}{K_i}$	0.065±0.003
Z [MPa]		9.9±2.5	Ga [J/m^2]	3.2±1.6	

*assumed to be the same as that of aluminum due to the very thin layer of about 4nm

Table 5.12 Interfacial Fracture Energy of NPS/Cu2O interface

Materials	E [Mpa]	v	K [MPa]	t [um]	t/K [um/MPa]
Epoxy	4200	0.34	4375	230±17	0.053±0.004
Cu2O	*127000	0.34	132292	*500	0.004
				$\sum_i \dfrac{t_i}{K_i}$	0.063±0.004
Z [MPa]		11.6±4.4	Ga [J/m^2]	4.2±3.2	

*assumed to be the same as that of copper due to the thin layer

Table 5.13 Interfacial Fracture Energy of NPS/Si3N4 interface

Materials	E [Mpa]	v	K [MPa]	t [um]	t/K [um/MPa]
Epoxy	4200	0.34	4375	222±21	0.051±0.005
Si3N4	310000	0.27	322917	675	0.002
				$\sum_i \dfrac{t_i}{K_i}$	0.060±0.005
Z [MPa]		10.2±3.1	Ga [J/m^2]	3.1±1.9	

CHAPTER 6

ADHESION PREDICTION MODEL

6.1 Particle Adhesion Model

As mentioned in chapter 3, the adhesion of nano-sized particles is dominated by van der Waals forces. The van der Waals forces refer to forces between molecules having dipoles caused by the spontaneous polarizations of the atoms and molecules in the material. This also includes induced instantaneous dipoles. The nonpolar van der Waals forces are also referred to as London dispersion forces since London dealt with spontaneous polarizations as the cause of optical dispersion (London, 1930).

The spontaneous polarization mechanism can be explained by quantum theory. In quantum theory, the electrons of an electrically neutral solid do not occupy fixed states of a sharply defined minimum energy, but vary quickly with time, generating electric and magnetic polarizations (Krupp, 1967). As atoms and molecules are polarized, solids can bear local electric fields even at absolute zero temperature. Above zero degrees, thermal excitations of the atoms and molecules can make additional contributions to the electric fields.

There are many particle adhesion models, including JKR model (Johnson-Kendall-Roberts, 1971), DMT model (Deryaguin-Muller-Toporov, 1975), MB model (Maugis and Barquins, 1978), Dahneke Model (Dahneke, 1972), MP model (Maugis and Pollock, 1984), Hiestand model (Hiestand, 1999), and Krupp model (Krupp, 1967). These models can be divided by two groups, that is, hardness and elastic modulus model and hardness model. In this section, these particle adhesion models will be introduced and examined to find the most appropriate model as NPS adhesion model.

6.1.1 Hardness & Elastic Modulus Model

Johnson, Kendall, and Roberts (JKR, 1971) derived the adhesion force required to pull apart two adhering spheres as Equation (6.1). In the derivation, it was assumed that that the two spheres in contact are perfectly elastic with radius R1 and R2, their surfaces are smooth, and all surface interactions occur only within the region of contact.

$$F_{JKR} = \frac{3}{2} \pi R^* \Delta\gamma \tag{6.1}$$

where $\Delta\gamma$ is the surface energy change and R^* is the harmonic mean radius of the spheres, which is equal to $R_1 R_2 / (R_1 + R_2)$.

Deryaguin, Muller, and Toporov (DMT, 1975) calculated the adhesion force of an elastic sphere adhered to a rigid plane surface by considering that the major part of the adhesion force is due to surface forces outside the region of contact. The force needed to detach the sphere from the surface considering a point contact only is equal to Equation (6.2).

$$F_{DMT} = 2 \pi R^* \Delta\gamma \tag{6.2}$$

Assuming that particles are comparatively hard so that they can deform the opposite surface at the contact point under an external load, Podczeck (1995) calculated the adhesion force between the particle and the contact surface. By defining indentation hardness, H, of the surface as Equation (6.3), the harmonic mean radius as Equation (6.4), and the reduced elastic modulus at the contact point as Equation (6.5), the adhesion force can be calculated as Equation (6.6).

$$H = \frac{F_{vdw}}{\pi a_o^2} \tag{6.3}$$

$$R^* = \frac{4E^* F_{vdw}^{1/2}}{3(\pi H)^{3/2}} \tag{6.4}$$

$$\frac{1}{E^*} = \frac{1 - v_1^2}{E_1} + \frac{1 - v_2^2}{E_2} \qquad (6.5)$$

where E_1 and E_2 are the elastic modulus and v_1 and v_2 are the poisson's ratio of the spheres.

$$F_{particle} = T' \Delta\gamma \frac{E^* F_{vdW}^{1/2}}{H^{3/2}} \qquad (6.6)$$

where T'=1.128 (JKR model), and T'=1.505 (DMT model).

Maugis and Pollock (1984) extended the JKR model and described the adhesion force during separation between a particle and a surface using a fracture mechanics approach. They also described the separation mechanism by three modes of adherence as ductile rupture, brittle separation at a contact radius formed applying an external load, and brittle separation at a contact radius smaller than that formed applying an external load. The MP model can be written as Equation (6.7).

$$F_{MP} = 0.64 \, \Delta\gamma \frac{E^* F_{vdW}^{1/2}}{H^{3/2}} \qquad (6.7)$$

Maugis and Barquins (1971) also suggested that the force necessary to pull two viscoelastic spheres apart is equal to Equation (6.8), which is equivalent to JKR model and DMT model except the coefficient of the equation.

$$F_{MB} = 0.627 \, \Delta\gamma \frac{E^* F_{vdW}^{1/2}}{H^{3/2}} \qquad (6.8)$$

Hiestand Model (1999), Equation (6.9), describes sphere to sphere contact with viscoelastic deformation assuming that the two spheres are identical materials.

$$F_{Hiestand} = \frac{E_o^*}{E_t^*} 1.128 \Delta\gamma \frac{E^* (2hd)^{1/2}}{H^{3/2}} \qquad (6.9)$$

6.1.2 Hardness Model

While the previous models are dependent of both the reduced elastic modulus

and the substrate hardness, the Krupp model (Krupp, 1967) reflects solely the substrate hardness effect as in Equation (6.10), which was supported later by Bowling (Bowling, 1985).

$$F_{Krupp} = 12.8 \times 10^{-10} \frac{h}{\pi \, d \, z_o^2} (1 + 6.4 \times 10^{-9} \frac{h}{z_o^3 \pi \, H}) \qquad (6.10)$$

where h is the van der Waals constant in eV, d is the particle diameter in um, z_o is the adhesion distance in Å.

In order to find an appropriate model for NPS adhesion model, Dynamic Mechanical Analysis (DMA) has been performed because elastic modulus is expected to change as temperature changes just as hardness changes. Figure 6.1 shows how the elastic modulus changes as temperature increases up to 260℃ from DMA, and Table 6.1 summarizes the elastic modulus of each material before and after Tg. Since the Tg of Kapton HN is above 260℃, the elastic modulus of Kapton HN was not measurable.
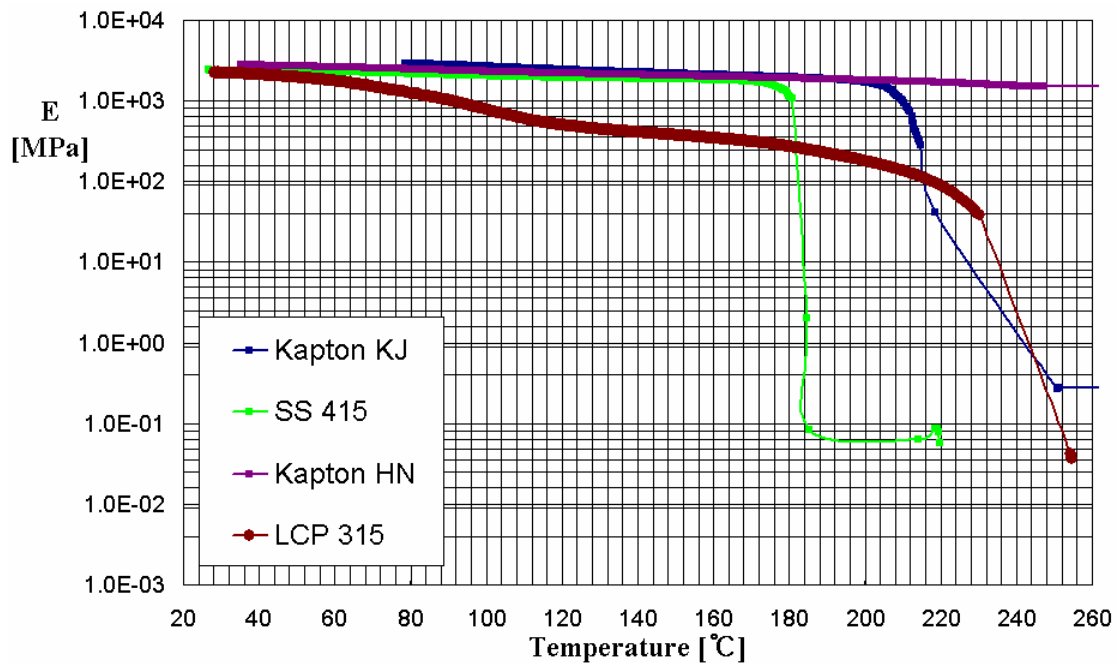
Figure 6.1 Dynamic Mechanical Analysis (DMA) data

Table 6.1 Summary of DMA data

Material	*Tg [℃]	E[GPa] < Tg	E[GPa] > Tg
Kapton KJ	220	2.0-2.9	~0.0001
SS 415	180-185	1.8-2.4	~0.00005
Kapton HN	360-410	1.5-2.8	N/A
LCP315	**190	0.1-2.4	~0.00004

*From manufacturer's data **Relative Thermal Index (Mechanical)

Table 6.2 shows that ASTM tape test results are consistent with the hardness-only model as the adhesion level increases as hardness decreases independent of the change in elastic modulus. Thus, it can be concluded from this experiment that the hardness-only dependent model is appropriate as NPS adhesion model. As a hardness-only model, Krupp model will be further examined in the next section as a NPS adhesion model.

Table 6.2 Particle force dependence on elastic modulus and hardness

	H @230C [Mpa]	E @230C [Mpa]	ν	E*	$F(\frac{E^*}{H^{3/2}})$	$F(\frac{1}{H})$	Tape Test
Kapton HN	56.4	1618.2	0.34	1788	F(4.2)	F(0.2)	0B
LCP 315	6.3	38.1	0.3	42	F(2.6)	F(1.6)	5B
Kapton KJ	1.4	0.1	0.3	0.1	F(0.1)	F(7.1)	5B
SS415	< 0.1	< 0.05	0.34	0.1	F(1.8)	F(100)	5B
NPS	484	*67 GPa	0.37	-	-	-	-

*Estimated from Hot hardness equation, Equation (4.2)

6.2 Krupp Model

In the Krupp model, the omnipresent van der Waals forces are assumed to be additive for assemblies of atoms and molecules and can be used for calculating the attraction between larger bodies as an integration over all pairs of atoms and molecules. The resulting equation for the van der Waals force is written as Equation 6.11.

$$F_{vdw} = 3.2 \times 10^{-15} \frac{h\,d}{z_o^2} \quad [N] \qquad (6.11)$$

where h is the van der Waals constant in eV, d is the particle diameter in um, z_o is the adhesion distance in Å.

The van der Waals constant, h, depends on the two materials to be joined, h_1 and h_2, and is calculated by the geometric mean of individual values (Visser, 1995) as Equation (6.12).

$$h = \sqrt{h_1^2 + h_2^2} \qquad (6.12)$$

Where h is the van der Waals constant, and h_1 and h_2 are the van der Waals constants for material 1 and 2, respectively.

As mentioned before, the van der Waals force is large enough for particles or surfaces to be deformed. From a 1um diameter particle with a van der Waals constant of 0.6 eV to a 100 um diameter particle with a constant of 9.0 eV, the van der Waals force per unit area can range from about 20MPa to 300MPa. These tremendous pressures deform the substrates and increase the contact area, which enhances the van der Waals force.

The additional van der Waals force due to deformation is a function of the increased contact area caused by the deformation and is given by Equation (6.13)

$$F_{vdw\,deform} = 6.4 \times 10^{-15} \frac{h\,a_o^2}{z_o^3} \quad [N] \qquad (6.13)$$

where a_o is the radius of the adhesive contact area in um.

In the NPS adhesion study, any capillary forces are excluded, assuming that all liquids are evaporated at the sintering temperature of 230C. Also, silver nano particles are assumed to be comparatively hard, so they can deform the opposite surface at the contact point (Zimon, 1982, Podczeck, 1996).

Therefore, the total adhesion force due to the van der Waals force and the additional van der Waals force caused by deformation can be written as in Equation (6.14).

$$F_{total\ vdw} = F_{vdw} + F_{vdw\ deform} \qquad (6.14)$$

In addition to the bond formation due to the van der Waals forces, there can be additional interfacial reactions during the NPS sintering process at 230℃. These include sintering effects, diffusive mixing, mutual dissolution and alloying at the interface. Although their concepts are not strictly separated, these effects are believed to contribute to interface formation and growth. While these reactions are specified separately according to the usual nomenclature, the actual bonds at the interfaces formed by these interactions are the same as those of the van der Waals force (Krupp, 1967).

Among the additional interfacial reactions, sintering between two solid materials is a growth of their adhesive area at a temperature about 25% above the lowest melting temperature of the reactants. The sintering mechanisms are reported to be very complicated, and include grain boundary diffusion, bulk diffusion, surface diffusion, evaporation, and condensation, which are simultaneously involved. More details on sintering can be found in chapter 3. Diffusive mixing of solid polymer materials have been investigated under elevated temperatures and special conditions (Voyutskii, 1963), but it was assumed to be negligible for metal-polymer adhesion as explained in chapter 3. Mutual dissolution of atoms of one metal in the surface layers of the other metal can occur at the interface between two metals when they are held at an elevated activation temperature. Depending on the two adherent materials, alloy formation may occur at such temperature.

However, these interfacial reactions are, for now, excluded in the NPS adhesion prediction model, which is solely based on the particle adhesion analysis and associated van der Waals force.

6.3 Model Fitting

Particle adhesion strength based on the particle adhesion theory is obtained by dividing the total van der Waals force by the projection area of the particle as in Equation (6.15), resulting in Equation (6.16).

$$\sigma_{particle\ adhesion} = \frac{F_{total\ vdw}}{A} = F_{totoal\ vdw}\frac{4}{\pi d^2} \tag{6.15}$$

where A is the projection area of the particle.

$$\sigma_{particle\ adhesion} = (3.2\times10^{-15}\frac{h\,d}{z_o^2} + 6.4\times10^{-15}\frac{h\,a_o^2}{z_o^3})\frac{4}{\pi d^2} \tag{6.16}$$

The particle adhesion strength model includes the effect of van der Waals constant (h), adhesion distance (z_o), particle size (d), and radius of contact area (a_o). As schematically described in Figure 6.2, the adhesive contact area radius (a_o) is related to the indentation hardness of the substrate.
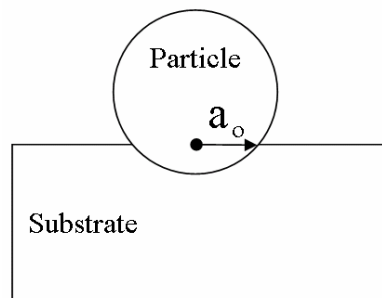
Figure 6.2 Radius of contact area

In particle adhesion, the hardness can be defined as Equation (6.17) because hardness refers to the substrate resistance to indentation due to van der Waals force

(Podczeck, 1996).

$$H = \frac{F_{total\_vdw}}{\pi a_o^2} \qquad (6.17)$$

As mentioned in Chapter 4, hardness value depends on the test method, indenter tip geometry, and indentation tip material. This means that the hardness values obtained from the method described in Chapter 4 may need to be adjusted to obtain the value that is required in the particle adhesion model using Equation (6.18).

$$H = C_a \times H_{measured} \qquad (6.18)$$

where C_a is the adjusting constant, and $H_{measured}$ is the measured substrate hardness in Pa by Vickers-like hardness test described in section 4.3.1.

Physically, when C_a is larger than 1, the required hardness (H) can be achieved using a narrower indentation tip, and vice versa, as schematically shown in Figure 6.3. However, if narrower tip needs to be used, resulting in greater indentation depth, a thicker specimen has to be prepared, which is very difficult for polymer film substrates.
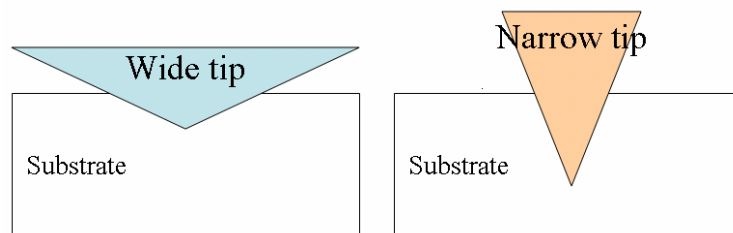
Figure 6.3 Tip geometry dependency of Hardness value

In this study, another constraint will be assigned in the hardness adjustment. Since the driving force for indentation is the internal attraction force due to van der Waals force, not any external pressure, the radius of contact is assumed not to be larger than the particle radius as illustrated in Figure 6.4.
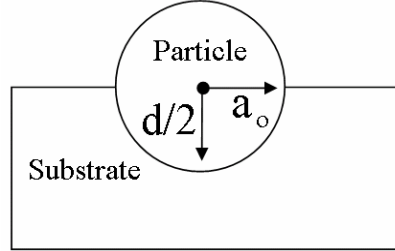
Figure 6.4 Maximum radius of contact area due to van der Waals force

Thus, all the measured hardness values will be adjusted not only by constraining the maximum radius of contact area to values below the silver nano particle radius, 4nm, but also by scaling down proportionally to the required hardness numbers in the adhesion model. Although the particle size distribution can result in a variation of the particle adhesion strength, the fracture area, over which adhesion strength is measured using MBST, will be large enough to take the adhesion strength based on the average particle size.

By substituting a_o^2 in Equation (6.17) with Equation (6.16),

$$\sigma_{particle\ adhesion} = (3.2 \times 10^{-15} \frac{h\,d}{z_o^2} + 6.4 \times 10^{-15} \frac{h\,F_{total\ vdw}}{z_o^3 \pi H}) \frac{4}{\pi d^2} \qquad (6.19)$$

Since the first term on the right side corresponds to $F_{total\ vdw}$, Equation (6.19) can be rewritten as Equation (6.20).

$$\sigma_{particle\ adhesion} = 3.2 \times 10^{-15} \frac{h\,d}{z_o^2} (1 + 6.4 \times 10^{-15} \frac{h}{z_o^3 \pi H}) \frac{4}{\pi d^2} \qquad (6.20)$$

Substituting H in Equation (6.20) with Equation (6.18) gives Equation (6.21).

$$\sigma_{particle\ adhesion} = 3.2 \times 10^{-15} \frac{h\,d}{z_o^2} (1 + 6.4 \times 10^{-15} \frac{h}{z_o^3 \pi\,C_a H_{measured}}) \frac{4}{\pi d^2} \qquad (6.21)$$

Finally, the particle adhesion prediction model can be rewritten as Equation (6.22).

$$\sigma_{\text{particle adhesion}} = 12.8 \times 10^{-10} \frac{h}{\pi\, d\, z_o^2} (1 + 6.4 \times 10^{-9} \frac{h}{C_a\, z_o^3\, \pi\, H_{\text{measured}}}) \qquad (6.22)$$

In the adhesion model, the adhesion distance, z_o, can be estimated from the surface energy change and the van der Waals constant using Equation (6.23) (Yu, 2004).

$$z_o\,[\,\text{um}\,] = 0.87 \left(\frac{h}{\Delta\gamma} \right)^{1/2} \times 10^{-3} \qquad (6.23)$$

where $\Delta\gamma$ is the surface energy change in mJ/m^2.

In order to develop the NPS adhesion strength prediction model, the particle adhesion model, Equation (6.22), may need to be fitted into the experimental data for a particular case of silver nano particles. Thus, by introducing a fitting constant to relate the adhesion model to experimental data, the NPS adhesion prediction model can be written as Equation (6.24).

$$\sigma_{\text{NPS adhesion}} = C_f \times 12.8 \times 10^{-10} \frac{h}{\pi\, d\, z_o^2} (1 + 6.4 \times 10^{-9} \frac{h}{C_a\, z_o^3\, \pi\, H_{\text{measured}}}) \qquad (6.24)$$

where C_f is a fitting constant, h is the van der Waals constant in eV, d is the particle diameter in um, z_o is the adhesion distance in Å, C_a is an adjusting constant, and H_{measured} is the measured substrate hardness in Pa by Vickers-like hardness test described in section 4.3.1.

The adhesion parameters in the NPS adhesion model are particle diameter, substrate hardness, adhesion distance, and van der Waals constant. The particle diameter of silver nano particles can be said to be nominally equal to 8 nm, and the van der Waals constant can be found in literatures (Bowling, 1985). Therefore, the tensile adhesion strength of NPS adhesion to the substrate can be predicted once the remaining two adhesion parameters, substrate hardness and adhesion distance, are measured. The effect of the particle size distribution can be incorporated into the measured adhesion strength

using physical adhesion test methods such as MBST, because the fracture area is large enough to takes the average particle adhesion strength based on the average particle size.

To evaluate the proposed model with the experimental data, the modified button shear test described in chapter 5 has been conducted for organic and inorganic materials. Once the best C_f and C_a for each material group are found by model fitting, the fitted modeling constants will be verified using different materials in Chapter 7.

6.4 NPS-Organic Adhesion Model

For the five organic materials, Kapton HN, Kapton KJ, LCP 315, SS415, and Teflon EFP, substrate hardness and contact angles were measured. The measured contact angles are converted to surface energy change using the approach explained in Appendix C. The calculated surface energy change is used for obtaining adhesion distance between silver nano particle and the organic substrate using Equation (6.23).

Assuming that the van der Waals constant, h, between all organic materials and NPS film is 2.6eV (Bowling, 1985), all the adhesion parameters measured and calculated for the five organic materials are summarized and tabulated in Table 6.2 before model fitting.

Table 6.1 NPS-organic adhesion parameters before model fitting

Material	$\Delta\gamma$ $[mJ/m^2]$	z_o $[\mathring{A}]$	$H_{measured}$ [Pa]	a_o [nm]	F_{vdw} [N]	$F_{vdw\ deform}$ [N]	$\sigma_{NPS\ adhesion}$ [MPa]	Z [MPa]	Tape Test
Kapton HN	88.7	1.49	5.6E+07	4.1	3.0E-09	8.6E-08	360.6	15.7	0B
Kapton KJ	89.0	1.49	1.4E+06	26.2	3.0E-09	3.5E-06	14082.5	>44.4*	5B
LCP 315	84.2	1.53	4.7E+06	13.9	2.8E-09	9.0E-07	3660.5	48.5	5B
SS 415	90.2	1.48	1.0E+05	98.6	3.1E-09	5.0E-05	203875.0	>43.7*	5B
Teflon FEP	44.9	2.09	2.2E+06	14.8	1.5E-09	4.0E-07	1625.3	**N/A	0B

*Beyond the Limit of MBST capability, **N/A: Not Available test specimen

As this table shows, the predicted tensile adhesion strength, $\sigma_{NPS\ adhesion}$, is an order of magnitude larger than the measured tensile bond strength using MBST, Z, before model fitting. For Kapton KJ and SS415, MBST fracture occurs between the epoxy adhesive and the NPS interface, which means that the adhesion strength between NPS and the substrate is higher than the MBST test capability. The Teflon FEP specimen for adhesion strength measurement using MBST was not available (N/A) because the NPS film was not formed on the Teflon FEP surface. Due to the low surface energy of Teflon FEP, NPS does not wet the surface, resulting in NPS islands rather than NPS film as shown in Figure 5.18.

Thus, Kapton HN and LCP315 that are measured for their interfacial tensile bond strengths will be used for fitting the adhesion prediction equation to these experimental data. In this fitting step, it was found that C_a=100 and C_f=1/4.9 provided the best fitting within the first decimal digit for the NPS adhesion strength to Kapton HN and LCP 315 as in Table 6.3. By constraining the maximum contact area radius to 4 nm, which is the radius of silver nano particle, it is assumed that the measured hardness value less than 0.6 MPa corresponds to the 4 nm of contact area radius.

Table 6.2 NPS-organic adhesion model fitting using C_f=1/4.9 and C_a=100

Material	$\Delta\gamma$ [mJ/m^2]	z_o [$\overset{o}{A}$]	H [MPa]	a_o [nm]	F_{vdw} [N]	$F_{vdw\ deform}$ [N]	$\sigma_{NPS\ adhesion}$ [MPa]	Z [MPa]	Error [MPa]	Tape Test
Kapton HN	88.7	1.49	5.6E+09	0.4	3.0E-09	8.6E-10	15.7	15.7	0	0B
Kapton KJ	89.0	1.49	1.4E+08	2.6	3.0E-09	3.5E-08	152.9	>44.4*	N/A	5B
LCP 315	84.2	1.53	4.7E+08	1.4	2.8E-09	9.0E-09	48.1	48.5	0.4	5B
SS 415	90.2	1.48	1.0E+07	4.0	3.1E-09	8.3E-08	348.1	>43.7*	N/A	5B
Teflon FEP	44.9	2.09	2.2E+08	1.5	1.5E-09	4.0E-09	22.4	**N/A	N/A	0B

*Beyond the Limit of MBST capability, **N/A: Not Available test specimen

6.5 NPS-Inorganic Adhesion Model

The adhesion parameters for inorganic materials before model fitting are summarized in Table 6.4. Since aluminum oxidizes easily with exposure to air, making it very difficult to measure aluminum contact angles with three different liquids, the surface energy change of etched aluminum is assumed to be the same as that of aluminum oxide. All the other contact angles are measured and all the substrate hardnesses are estimated from a reference for all the inorganic materials in consideration, Cu2O, Al2O3, Si3N4, etched Cu, and etched Al (Wang, 1999). The measured adhesion strength of NPS-etched Cu substrate is far away from the predicted adhesion strength. In fact, the etched Cu has a very strong adhesion to NPS, with a value larger than 73.7 MPa at the minimum because the fracture occurs between epoxy adhesive and NPS in the NPS-etched Cu system. Thus, there might be an additional factor that contributed to the NPS-etched Cu adhesion. This will be investigated in Chapter 7.

Table 6.3 NPS-inorganic adhesion parameters before model fitting

Material	h [eV]	$\Delta\gamma$ [mJ/m^2]	z_o [Å]	$H_{estimated}$ [MPa]	a_o [nm]	F_{vdw} [N]	$F_{vdw\ deform}$ [N]	$\sigma_{NPS\ adhesion}$ [MPa]	Z [MPa]	Tape Test
Cu2O	8.7	74.4	2.98	1.2E+09	0.815	2.5E-09	1.4E-09	13.4	11.6	0B
Al2O3	6.0	78.9	2.40	1.9E+10	0.210	2.7E-09	1.2E-10	9.6	9.9	0B
Si3N4	7.9	73.8	2.85	7.8E+09	0.319	2.5E-09	2.2E-10	9.3	10.2	0B
(etched) Cu	8.7	78.9	2.89	5.1E+08	1.289	2.7E-09	3.8E-09	22.3	>73.7*	5B
(etched) Al	6.0	**78.9	2.40	2.4E+08	1.870	2.7E-09	9.7E-09	42.5	61.3	5B

*Beyond the Limit of MBST capability, ** surface energy of alumina is used.

Except the etched Cu, the predicted tensile adhesion strength, $\sigma_{NPS\ adhesion}$, is almost the same as the measured tensile bond strength using MBST, Z, even before model fitting in Table 6.4. However, to get better model fitting, two cases of Al2O3 and etched Al are selected and the adhesion model is better fitted into the experimental data

as in Table 6.5. In the inorganic-NPS adhesion, the fitting constants are C_a=0.6 and C_f =6.0.

Table 6.4 NPS-inorganic adhesion model fitting using C_f =1/6.0 and C_a=0.6

Material	h [eV]	$\Delta\gamma$ [mJ/m^2]	z_o [$\overset{o}{A}$]	H [MPa]	a_o [nm]	F_{vdw} [N]	$F_{vdw\ deform}$ [N]	σ_{NPS} [MPa]	Z [MPa]	Error [MPa]	Tape Test
Cu2O	8.7	74.4	2.98	7.2E8	1.052	2.5E-9	2.3E-9	16.1	11.6	4.5	0B
Al2O3	6.0	78.9	2.40	1.2E10	0.272	2.7E-9	2.0E-10	9.5	9.9	0.4	0B
Si3N4	7.9	73.8	2.85	4.7E9	0.412	2.5E-9	3.7E-10	9.5	10.2	0.7	0B
Cu	8.7	78.9	2.89	3.1E8	1.664	2.7E-9	6.4E-9	30.1	>73.7*	N/A	5B
Al	6.0	**78.9	2.40	1.5E8	2.414	2.7E-9	1.6E-8	62.6	61.3	1.3	5B

*Beyond the Limit of MBST capability, ** surface energy of alumina is used.

6.6 Summary

Based on the study in Chapter 6, the adhesion prediction models for NPS-organic substrates and NPS-inorganic substrates are proposed as Equation (6.25) and Equation (6.26), respectively.

$$\sigma_{NPS\ adhesion} = \frac{1}{4.9} \times 12.8 \times 10^{-10} \frac{h}{\pi\, d\, z_o^2} (1 + 6.4 \times 10^{-9} \frac{h}{100 \times z_o^3 \pi\, H_{measured}}) \quad (6.25)$$

$$\sigma_{NPS\ adhesion} = \frac{1}{6.0} \times 12.8 \times 10^{-10} \frac{h}{\pi\, d\, z_o^2} (1 + 6.4 \times 10^{-9} \frac{h}{0.6 \times z_o^3 \pi\, H_{estimated}}) \quad (6.26)$$

where h is the van der Waals constant in eV, d is the particle diameter in um, z_o is the adhesion distance in $\overset{o}{A}$, and $H_{measured}$ is the measured substrate hardness in Pa by Vickers-like hardness test described in section 4.3.1.

In Chapter 7, these proposed adhesion models will be verified as NPS adhesion models using different sets of organic and inorganic materials.

CHAPTER 7

VERIFICATION AND ADHESION IMPROVEMENT

7.1 Test Materials

All the substrate materials used for the adhesion model verification purpose are summarized in Table 7.1 with their typical properties. The organic substrate materials used in the verification step for the proposed adhesion prediction model include Kapton FPC, LCP 290, Pyralux FR, and BCB. Their chemical structures are also shown in Figure 7.1. The Kapton FPC is another type of thermosetting polyimide film supplied by Dupont. LCP 290 is a liquid crystal material with melting point of 290℃ supplied by Rogers Corp. Pyralux FR is an acrylic-based thermoplastic material supplied by Dupont. Finally, BCB stands for BenzocycloButene, which is a widely used dielectric material in the electronics packaging industry. The BCB substrate was prepared by using spin-coating BCB liquids on a silicon wafer and then curing the liquids, resulting in BCB thin film of around 5 um. The BCB is a thermosetting polymer with glass transition temperature (Tg) of greater than 350℃.

Table 7.1 Substrate Materials used for verification of adhesion model

Category	Material	Supplier	Thick-ness [um]	Tg [℃]	Tm [℃]	UTS [MPa]	CTE@25℃ [ppm/℃]
Organic	Kapton FPC	Dupont	125	360-410	N/A	231	20
	LCP 290	Rogers Corp.	50	190**	290	216	17(x,y) 150(z)
	Pyralux FR	Dupont	50	N/A	N/A	N/A	60
	BCB	Dow	50	>360	N/A	87	42
Inorganic	Au (ENIG)	McMaster Carr	0.1	N/A	1064	100	14.2
	Ni (ENIG)	(Au removal from ENIG)	5	N/A	1453	168	13.4
	SiO2	SVM*	675	N/A	1650	110	0.5
	Ag	(NPS film)	2	N/A	961	170	18.9

*Silicon Valley Microelectronics, Inc. **Relative Thermal Index (Mechanical)

Inorganic materials include gold, nickel, silicon dioxide (SiO2), and silver. The outermost surface layer of electroless nickel immersion gold (ENIG) plate is used as gold's substrate material, which is about 0.1 um thickness. A nickel substrate is prepared by rubbing off the gold layer from ENIG plate, which is about 3-6 um thick. A silicon dioxide wafer is used as the SiO2 substrate. Sintered NPS film will be used as a silver substrate for NPS adhesion testing to silver. (It is known that AgO is transformed into Ag_2O at around 100-200C, and the complete thermal decomposition of Ag_2O into Ag and O_2 occurs at 400C. (Waterhouse, 2001)
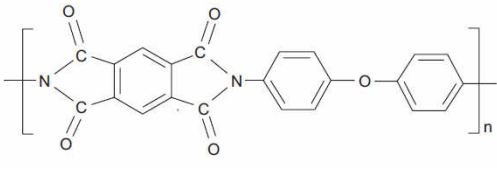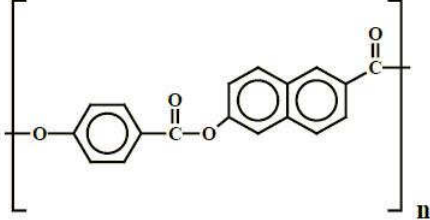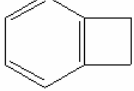
(a) Kapton FPC	(b) LCP290
Proprietary (Acrylic-based adhesive)	
(c) Pyralux FR	(d) BCB (Benzocyclobutene, C_8H_8)

Figure 7.1 Chemical Structure of organic substrate materials

7.2 NPS-Organic Adhesion Model Verification

The adhesion prediction model for NPS-organic materials, Equation (6.25), will be verified as an appropriate adhesion model in this section.

$$\sigma_{NPS\ adhesion} = \frac{1}{4.9} \times 12.8 \times 10^{-10} \frac{h}{\pi d\, z_o^2}(1 + 6.4 \times 10^{-9} \frac{h}{100 \times z_o^3 \pi H_{measured}}) \quad (6.25)$$

The predicted adhesion strength between NPS and the organic substrates is calculated from Equation (6.25) under the assumption that the van der Waals constant for polymers and NPS is 2.6eV. After contact angles are measured, surface energy changes are calculated using the approach explained in Appendix C, whose results are tabulated in Table 7.2.

Table 7.2 Contact angle and surface energy change

Materials	Contact Angle [mean ± σ °]			Surface Energy Change [mJ/m^2]
	water	Glycerol	Diiodomethane	
Kapton FPC	73.6±3.8	72.8±2.0	44.6±0.9	80.2
LCP 290	70.2±3.7	82.4±4.1	42.0±5.4	82.4
Pyralux FR	76.8±4.8	86.6±3.0	62.3±1.5	69.4
BCB	35.1±4.4	50.9±6.6	45.3±4.0	82.9

The interfacial bond strengths in tension for the NPS-organic materials used for model verification are measured from MBST except BCB materials and summarized in Table 7.3. Pyralux FR forms a very strong adhesion bond to NPS sintered at 230℃ and it is not fractured at the Pyralux FR-NPS interface, but at the NPS-epoxy interface. By reducing the sintering temperature to 182℃, Pyralux FR was fractured at the interface between Pyralux FR and NPS film. Also, LCP 290 was fractured at the LCP cohesive. Thus, LCP 315 with NPS sintering temperature of 190℃ is used as verification of the model since it is fractured at the interface between LCP315 and NPS film. BCB-NPS was evaluated using the ASTM tape test due to insufficient materials, and it showed 0B. The default process condition for NPS sintering is at 230℃ for 1 hr.

Table 7.3 MBST results for organic materials

| Substrates @ Sintering Temperature	Die Configuration	$\overline{\sigma}$	$\overline{\tau}$	S	Z	Fracture Mode
Kapton FPC @230℃	Full Die	16.2±2.9	5.2±0.7	10.4±2.7	18.6±3.9	Interface
	Mid Die	4.6±1.0	10.0±2.6			
LCP 315 @190℃	Full Die	26.4±5.9	22.8±2.5	32.4±4.9	37.1±6.9	Interface
	Mid Die	7.3±2.1	31.8±4.6			
Pyralux FR @182℃	Full Die	43.9±5.4	36.3±1.5	56.0±7.9	57.7±9.6	Interface
	Mid Die	13.4±6.5	54.4±7.2			
LCP 290 @230℃	Full Die	21.6±2.7	23.7±1.9	43.7±4.9	25.7±3.8	LCP cohesive
	Mid Die	9.9±2.2	40.3±3.8			
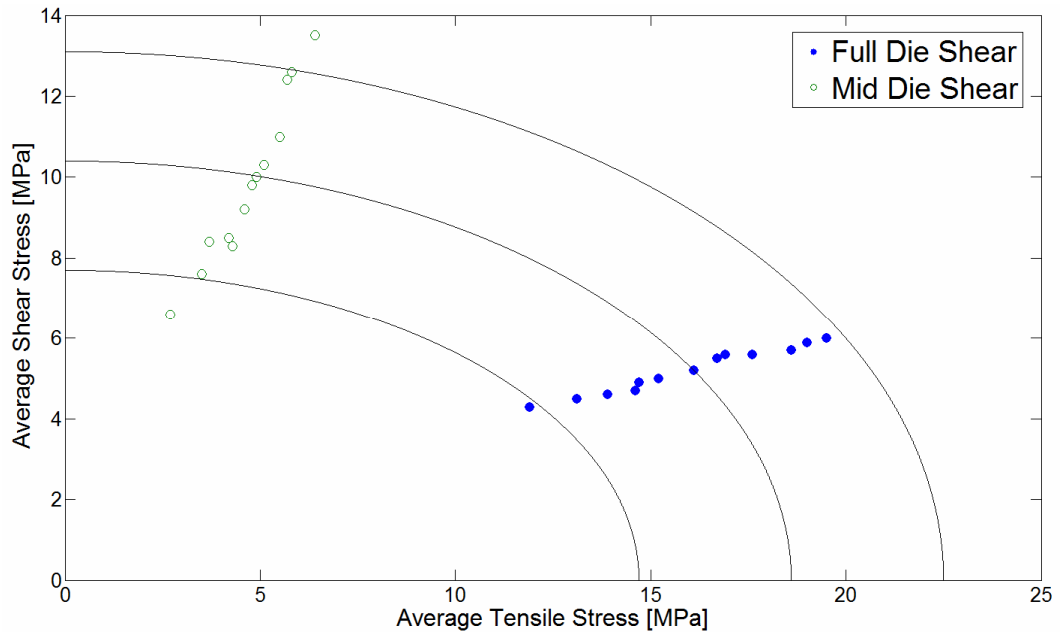
(a) **Kapton FPC-NPS**
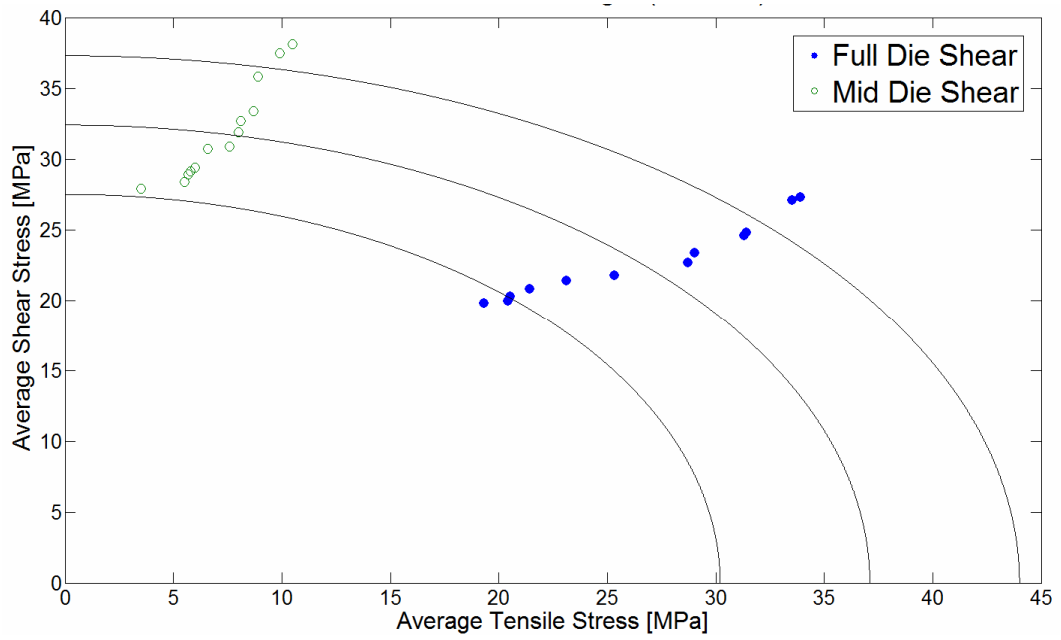
(b)
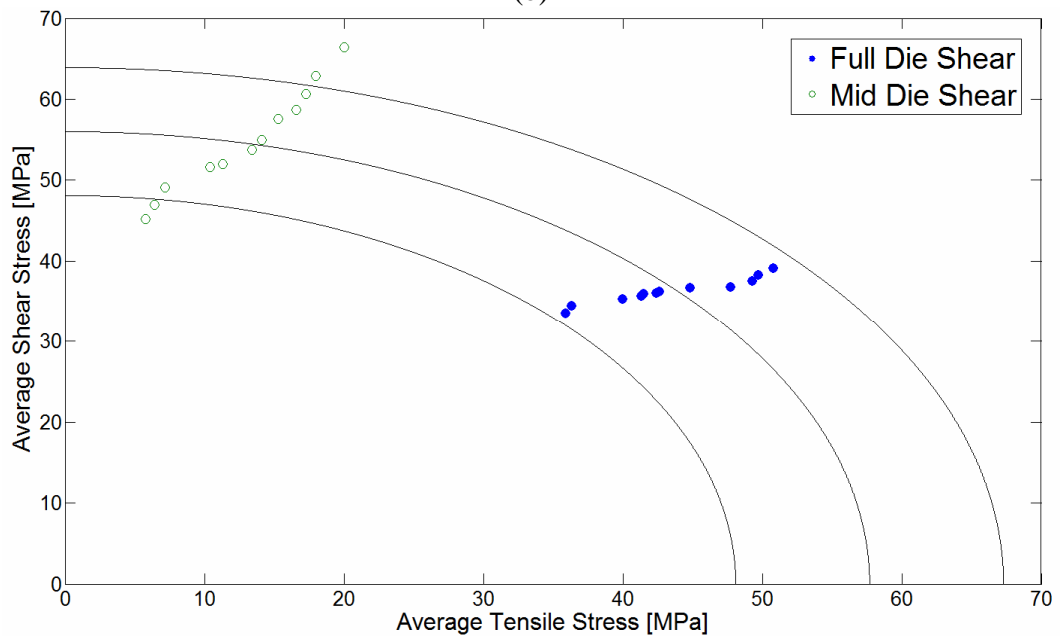
(c)

Figure 7.2 Average tensile - shear stress plot for (a) Kapton FPC-NPS (b)
LCP315@190℃-NPS (c) Pyralux FR@182℃-NPS adhesion

All the measurements of inorganic substrate hardness, adhesion distance, as well
as other calculated values are listed in Table 7.4. The error in Table 7.4 is the difference

between the measured adhesion strength, Z, and the predicted adhesion strength, $\sigma_{NPS\ adhesion}$. It could be said that this error indicates the accuracy of the MBST based on the theoretical NPS adhesion prediction model.

For BCB substrate, it was very difficult to measure the hot hardness at the NPS sintering temperature of 230℃ because the BCB film thickness (~5um) is far smaller than the required indentation depth in the hand-made hot hardness tester. Fortunately, it is reported that the hardness behavior of polymers with temperature is very similar and proportional to that of elastic modulus (Darlix, 1986) before and after glass transition temperature (Tg). Thus, the BCB hot hardness level can be estimated from a similar material, which has the same level of glass transition temperature and tensile modulus at room temperature. The tensile modulus and Tg of BCB are reported as 2.9GPa and minimum 350℃, respectively (Patel, 1998, Dow, 2009). Similarly, Kapton FPC has a tensile modulus and Tg of 2.8GPa and minimum 360℃, respectively (Megusar, 1997, Dupont, 2009). Thus, for the purpose of estimation, the hot hardness of BCB at 230℃ is assumed to be equal to that of Kapton FPC. Since the predicted adhesion strength of NPS-BCB is the same level as that of NPS-Kapton FPC, the tape test results are 0B as expected.

The LCP 290-NPS system shows lower adhesion strength than the predicted one. The lower strength might be due to the fracture initiation at the LCP290 cohesive and then propagation through the bulk of LCP290. The fracture mode analyses for test materials including the NPS-LCP290 interface are summarized in Table 7.5.

Table 7.4 NPS adhesion model verification for organic substrate

Material	$\Delta\gamma$ [mJ/m^2]	z_o [Å]	H [MPa]	a_o [nm]	F_{vdw} [N]	$F_{vdw\,deform}$ [N]	$\sigma_{NPS\,adhesion}$ [MPa]	Z [MPa]	Error [MPa]	Tape Test
Kapton FPC	80.2	1.57	2.6E+09	0.6	2.7E-09	1.5E-09	17.0	18.6	1.6	0B
LCP 315 @190C	84.2	1.53	7.5E+08	1.1	2.8E-09	5.6E-09	34.4	37.1	2.7	4B
Pyralux FR @182C	69.4	1.68	2.5E+08	1.7	2.3E-09	1.0E-08	51.8	57.7	5.9	5B
LCP 290	82.4	1.55	2.5E+08	1.9	2.8E-09	1.6E-08	76.3	>25.7*	N/A	5B
BCB	82.9	1.54	**2.6E+09	0.6	2.8E-09	1.6E-09	17.9	N/A	N/A	0B

*LCP290 cohesive fracture, **Hot hardness of Kapton FPC is adopted

Figure 7.3 displays the predicted and the measured adhesion strength for organic materials in the interfacial bond strength in tension versus H plot. The adhesion strength of Kapton FPC, Kapton HN, LCP 315, and Pyralux FR are well predicted from the adhesion prediction model. Therefore, the NPS adhesion model can be said to well predict the actual adhesion strength between NPS and organic materials.
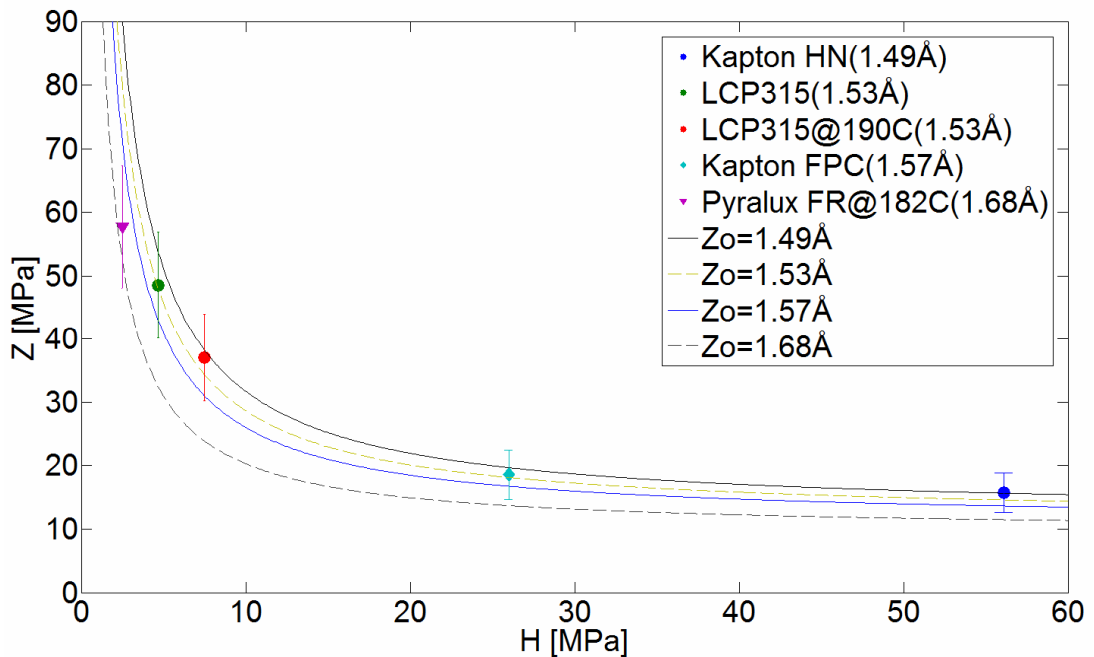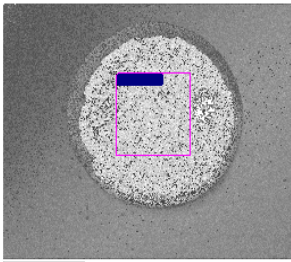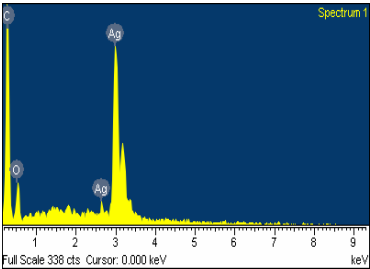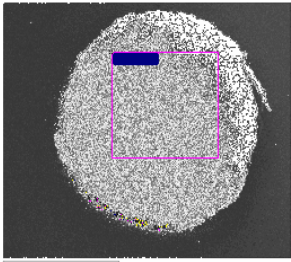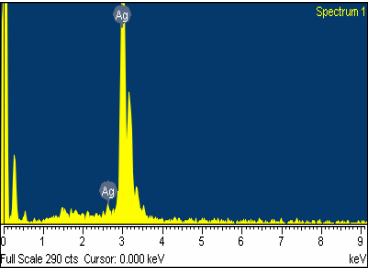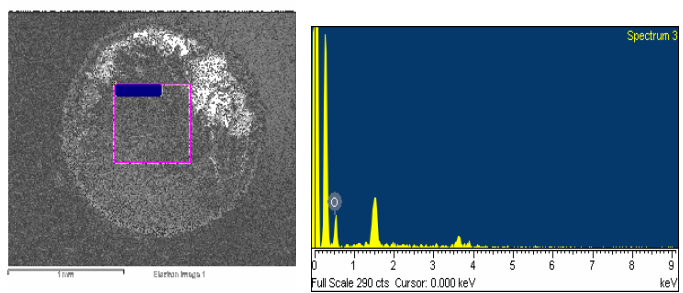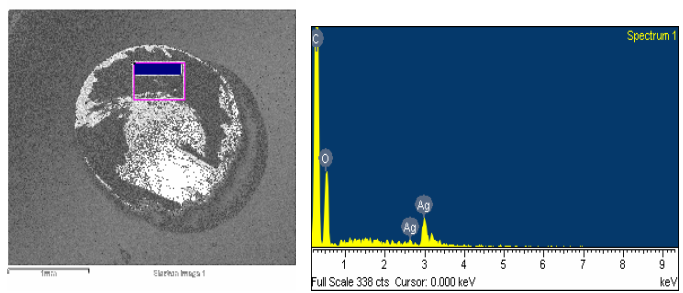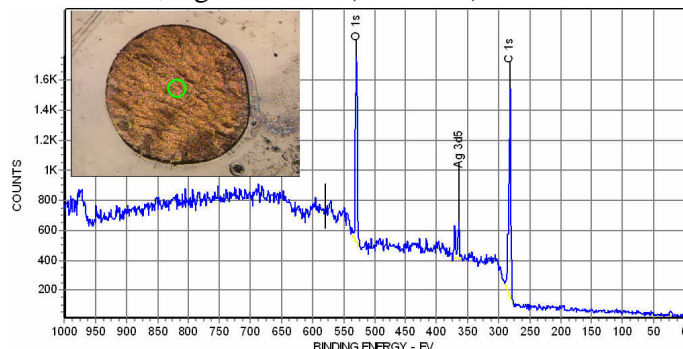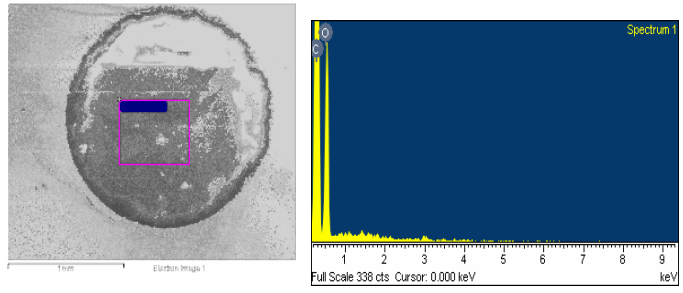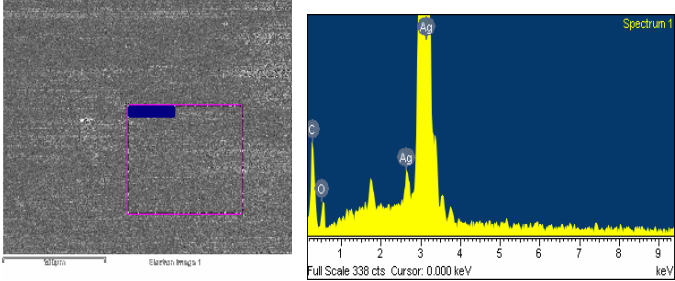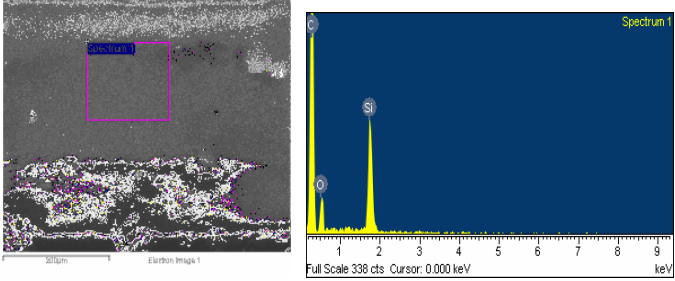

Figure 7.3 Interfacial Tensile Bond Strength Plot for Organic-NPS adhesion

As shown in Figure 7.3, substrate hot hardness is the primary adhesion factors in the NPS adhesion prediction model. The NPS adhesion strength varies significantly depending on the hot hardness of the substrate. Besides, the variation of NPS adhesion strength with substrate hot hardness is dependent on the adhesion distance. Especially in the low hardness range, even a small adhesion distance change can significantly affect the NPS adhesion strength.

Table 7.5 Facture Mode analysis for organic materials

Substrate (Z)	Fracture Mode	EDX Analysis
Kapton FPC (18.6 MPa)	Mostly NPS/FPC interface	Ag: 89.2wt%, O:10.8wt% (NPS side) O: 83.7%, Ag: 16.3% (Substrate side)
Pyralux FR (65.3MPa at 182℃)	Interface	Ag: 100wt% (NPS side)

		O: 100wt% (Substrate side)	
LCP290 (24.4 MPa)	LCP cohesive & NPS/LCP290 interface	O: 56.0wt%, Ag: 44.0wt% (NPS side) XPS analysis (O: 71.4wt%, Ag: 28.6wt%: NPS side) O: 100wt% (Substrate side)	

BCB	NPS/BCB interface	 Ag: 88.1wt%, O: 11.9wt% (NPS side magnified) O: 43wt%, Si:57wt% (Substrate side magnified)

7.3 NPS-Inorganic Adhesion Model Verification

The adhesion prediction model for NPS-inorganic materials that will be verified in this section is Equation (6.26).

$$\sigma_{\text{NPS adhesion}} = \frac{1}{6.0} \times 12.8 \times 10^{-10} \frac{h}{\pi \, d \, z_o^2} (1 + 6.4 \times 10^{-9} \frac{h}{0.6 \times z_o^3 \pi \, H_{\text{measured}}}) \quad (6.26)$$

The interfacial tensile bond strengths of inorganic materials used for model verification are measured by MBST and summarized with the fracture mode analysis in Table 7.6 and 7.7. The fracture of NPS-Au occurred at the NPS-Au interface. The Ni detected is due to the larger the interaction volume of SEM than the Au layer thickness of 0.1um in the ENIG substrate). Ni shows very weak adhesion to NPS, and it is fractured at the Ni-NPS interface. SiO2 shows slightly higher adhesion strength than Ni, but it is still in the 0B level at the ASTM tape test. Sintered Ag film as the silver substrate was prepared on an etched Cu substrate, to which NPS forms a strong adhesion, so that silver substrate is not separated from the base Cu substrate. The Ag film forms a strong

adhesion with NPS, as it is not fractured at the NPS-Ag interface, but at the NPS-epoxy interface even at the fracture strength of 73.7 MPa.

Table 7.6 MBST results for inorganic materials

Substrates	Die Configuration	$\bar{\sigma}$	$\bar{\tau}$	S	Z	Fracture Mode
Au (ENIG)	Full Die	39.3±5.3	21.2±4.2	65.3±9.9	41.6±5.9	Interface
	Mid Die	19.6±3.9	57.6±7.5			
NiO	Full Die	7.6±2.2	3.8±0.9	10.6±1.7	8.2±2.5	Interface
	Mid Die	3.9±0.4	9.3±1.1			
SiO2	Full Die	12.8±2.1	4.9±1.4	12.9±5.2	13.8±2.6	Interface
	Mid Die	6.0±2.9	11.7±4.3			
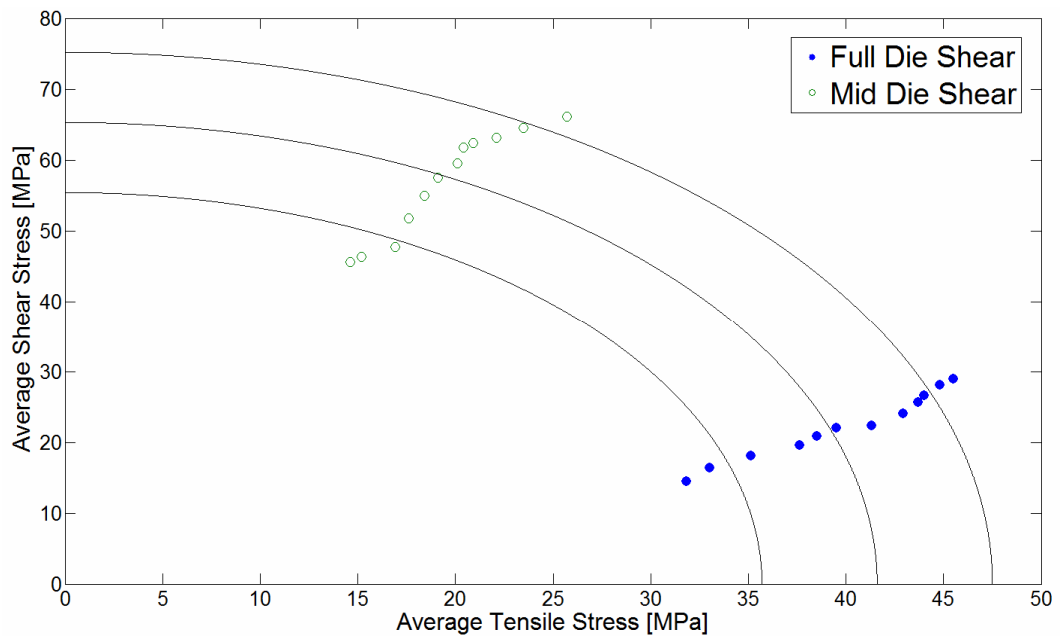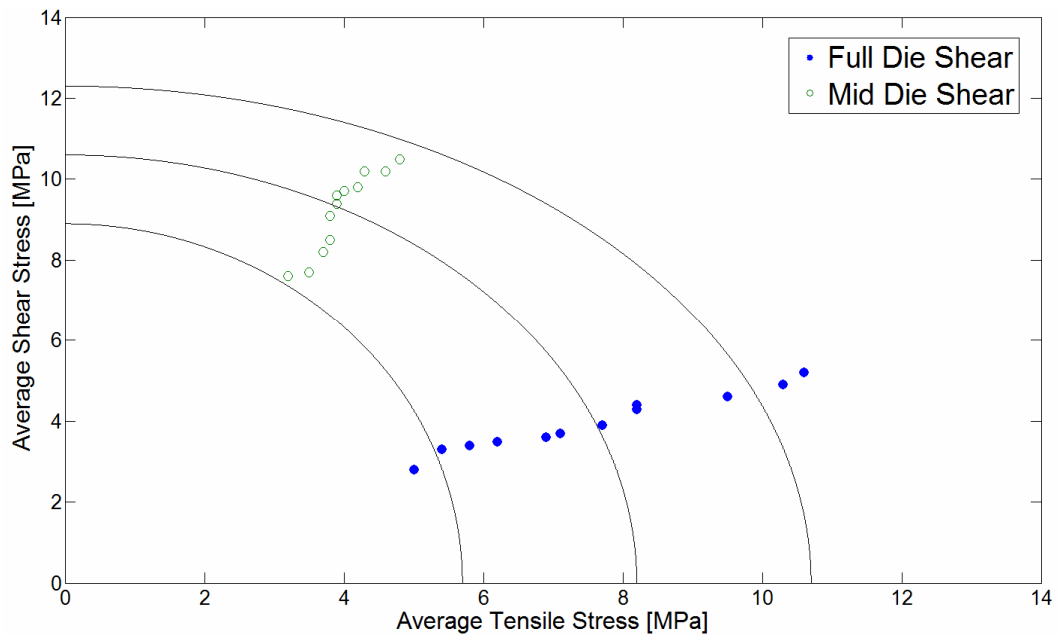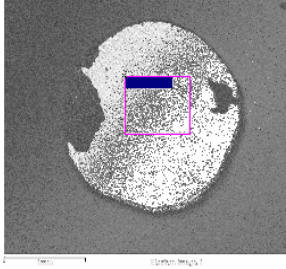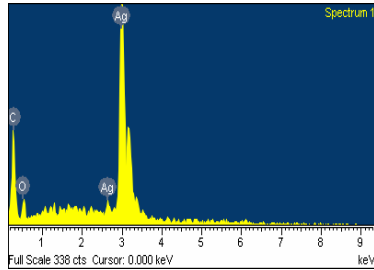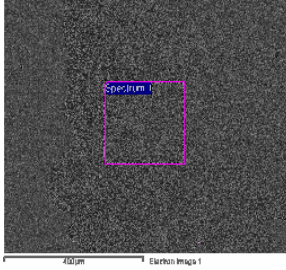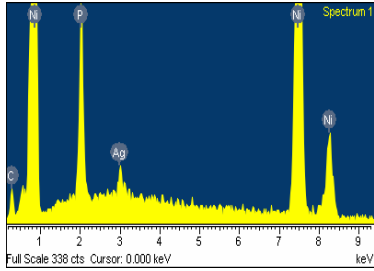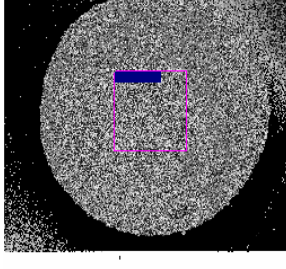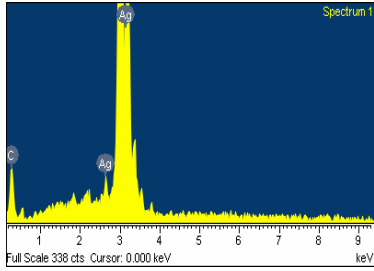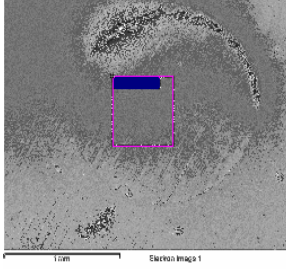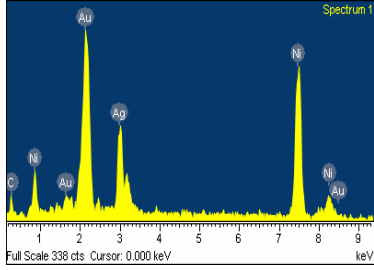
(a) Au-NPS

(b)
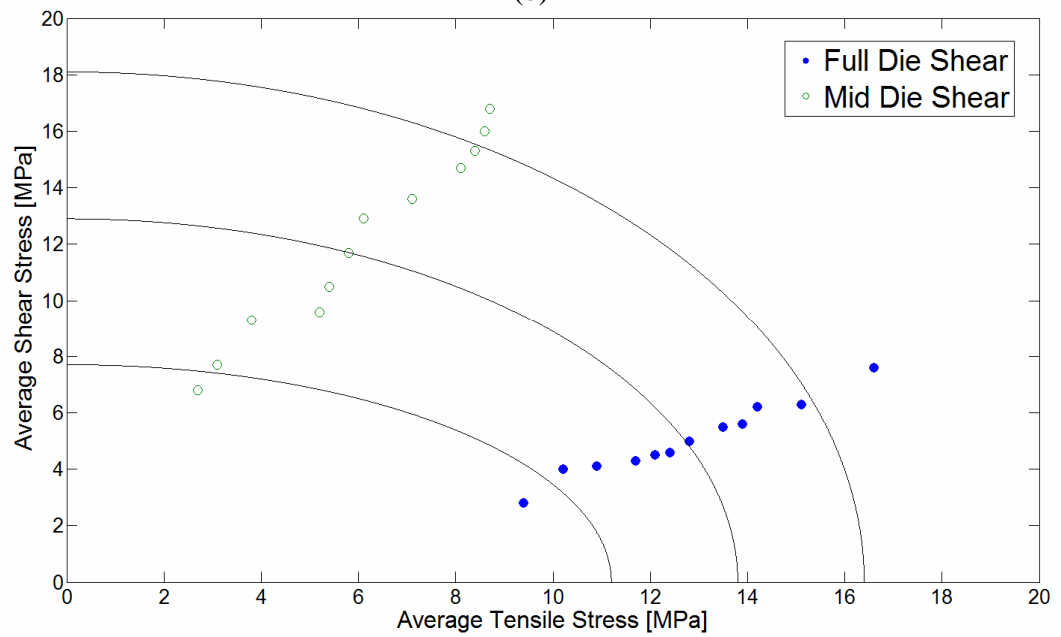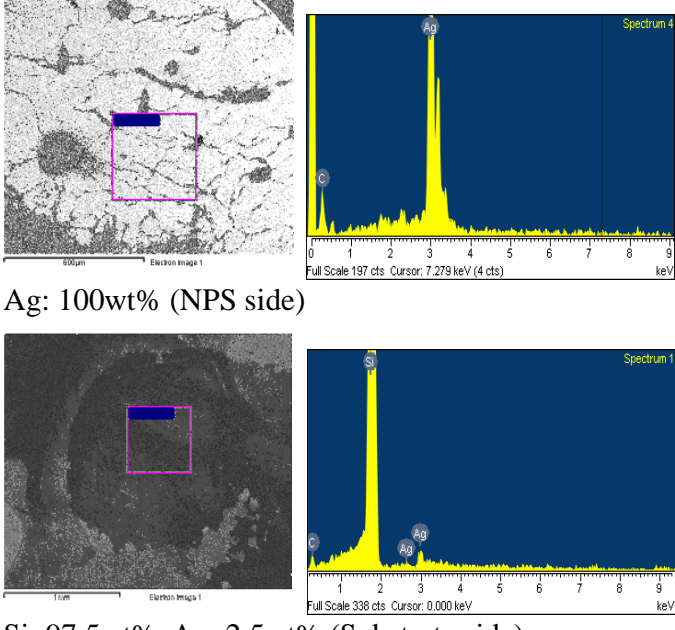
(c)

Figure 7.4 Average tensile - shear stress plot for (a) Au-NPS (b) NiO-NPS (c) SiO2-NPS adhesion

Table 7.7 Facture Mode analysis for inorganic materials

Substrate (Z)	Fracture Mode	EDX Analysis
NiO (9.7 MPa)	NPS/NiO interface	Ag: 92.3wt%, O: 7.7wt% (NPS side) Ni: 90.4wt%, P:7.8wt%, Ag: 1.8wt (Substrate side)
Au (41.6 MPa)	NPS/Au interface	Ag: 100wt% (NPS side) Ni: 46.0wt%, Au: 34.8wt%, Ag: 19.2wt% (Substrate side)

SiO2	Mostly NPS/SiO2 interface	
		Ag: 100wt% (NPS side)
		Si: 97.5wt%, Ag: 2.5wt% (Substrate side)

The hot hardness of inorganic substrates found from the literature is summarized in Table 7.8 (Wang, 1999). Contact angles are measured, and surface energy changes are calculated as tabulated in Table 7.9 using the approach in Appendix C. Adhesion distance, other calculated values, and the predicted adhesion strength between NPS and each inorganic substrate, which is calculated from Equation 6.26, are listed in Table 7.10. The error in Table 7.10 is the difference between the predicted adhesion strength, $\sigma_{NPS\ adhesion}$, and the measured adhesion strength, Z. This error can also indicate how the MBST is accurate based on the theoretical NPS adhesion prediction model.

Table 7.8 Hardness of inorganic materials at NPS sintering temperature

Material	Vickers Hardness (H_o, MPa)	Softening Coefficient of Hardness (S_o, 10-4/^{o}C)	Hardness at 230°C (H, Mpa)
Au	400	10.0	318
Ni	1325	10.0	1053
NiO	4800	*10.0	3814
Si	2540	9.5	2041
SiO2	12015	*9.5	9657
Ag	600	9.3	484
Ag2O	1350	*9.3	1090

*assumed value

Table 7.9 Contact angle and surface energy change

Materials	Contact Angle [$^\circ$]			Surface Energy Change [mJ/m^2]
	water	Glycerol	Diiodomethane	
Au	77.6±2.5	72.1±1.5	46.0±2.4	79.3
NiO	71.3±2.1	81.1±3.1	57.2±3.7	73.1
SiO2	37.2±1.1	36.7±1.0	43.3±1.8	87.2
Ag	82.4±3.7	69.5±3.9	36.7±3.1	84.4

Table 7.10 NPS adhesion model verification for inorganic substrate

Material	h [eV]	$\Delta\gamma$ [mJ/m^2]	z_o [$\overset{o}{A}$]	H [Pa]	a_o [nm]	F_{vdw} [N]	$F_{vdw\ deform}$ [N]	$\sigma_{NPS\ adhesion}$ [MPa]	Z [MPa]	Error [MPa]	Tape Test
Au	9.0	79.3	2.93	1.9E+08	2.116	2.7E-09	1.0E-08	42.9	41.6	1.3	5B
NiO	8.7	73.1	3.00	2.3E+09	0.587	2.5E-09	7.1E-10	10.6	8.2	2.4	0B
SiO2	7.9	87.2	2.62	7.2E+09	0.361	3.0E-09	3.7E-10	11.0	13.8	2.8	0B
Ag	9.0	84.4	2.84	2.9E+08	1.769	2.9E-09	7.9E-09	35.6	>73.7	N/A	5B

The predicted adhesion strength of the NPS-inorganic system is well suited to the measured interfacial tensile bond strength as plotted in Figure 7.5. In the NPS-silver

fracture, which is not shown in Figure 7.5, fracture occurs at the epoxy adhesive-NPS interface, not at the NPS-Ag interface, which means that Ag has a strong adhesion to NPS. Therefore, any additional adhesion factor might work in the NPS-Ag adhesion just like the NPS-etched Cu adhesion. On the whole, the NPS adhesion model predicts well the actual adhesion strength between NPS and inorganic materials studied.
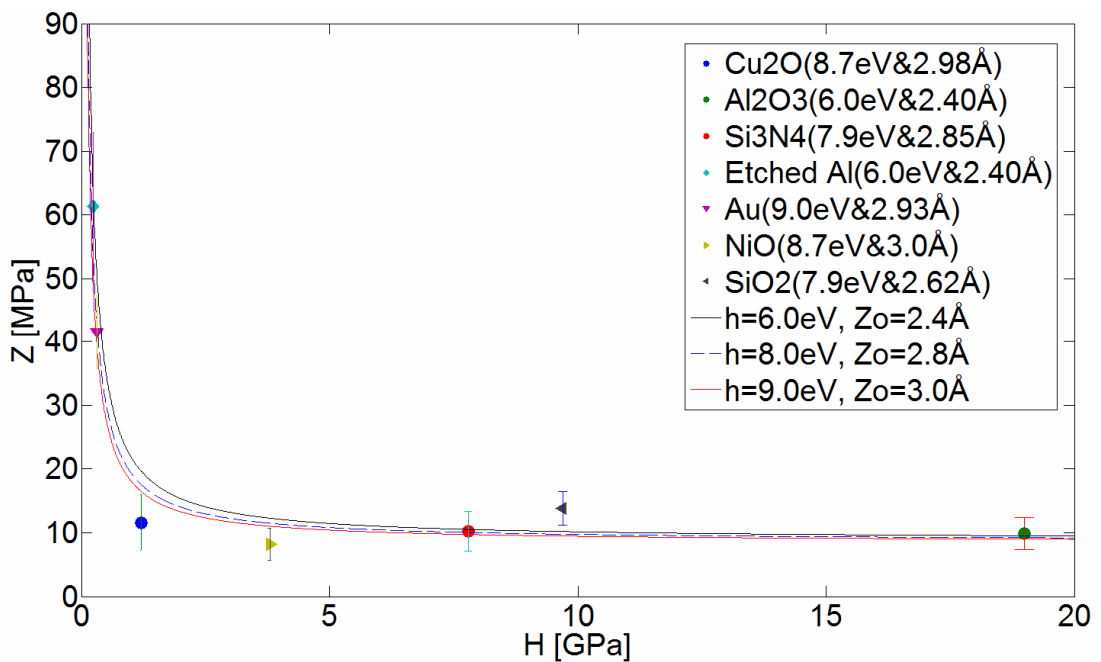

Figure 7.5 Interfacial Bond Strength in Tension Plot for Inorganic-NPS adhesion

7.4 Summary and Discussion

The proposed NPS adhesion model was successfully verified for a variety of organic and inorganic substrate materials. The adhesion strength of any new substrate material to NPS can now be predicted using the verified NPS adhesion prediction model. As schematically shown in Figure 7.6, once the hot hardness and adhesion distance are measured as input to the adhesion prediction model, the interfacial tensile bond strength, Z, can be predicted. Depending on the substrates, especially for metals, there could be additional adhesion factors such as diffusion as in Cu and Ag.
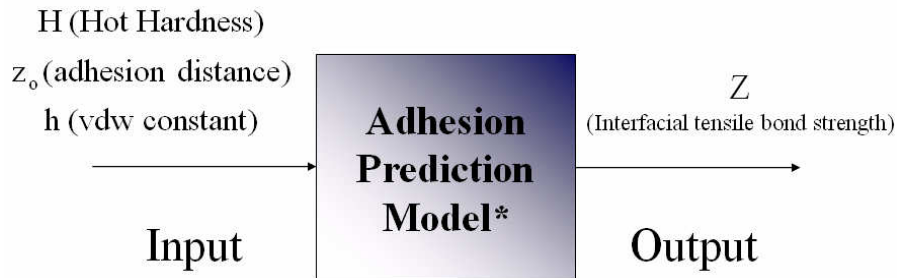
Figure 7.6 Schematic of NPS adhesion prediction model

As shown in Figure 7.3 and 7.5, the interfacial tensile bond strength increases as the substrate hardness decreases. However, this change is not linear. In other words, the adhesion strength starts increasing abruptly at a certain point of substrate hardness. The cause of this phenomenon is that the NPS adhesion strength is a combination of van der Waals force component and the additional van der Waals force component caused by deformation. As shown in Figure 7.7, the adhesion strength due to the intrinsic van der Waals force is constant regardless of substrate hardness, which is the same as when the substrate hardness is assumed to be infinite at the fixed van der Waals constant (2.6eV), adhesion distance (1.49 Å), and particle diameter (8nm).

The additional van der Waals force due to deformation starts significantly contributing to the total bond strength at the point, "T," in the Figure 7.7. This transition point depends on the adhesion parameters such as van der Waals constant, adhesion distance, and adjusting constant (C_a). It should be noticed that the T point is not related to the particle diameter. In the NPS adhesion prediction model, Equation (6.24), the transition point corresponds to the point where the additional van der Waals force component is equal to the intrinsic van der Waals force component. From Equation (6.24), the substrate hardness value at the point T can be written as Equation (7.1).
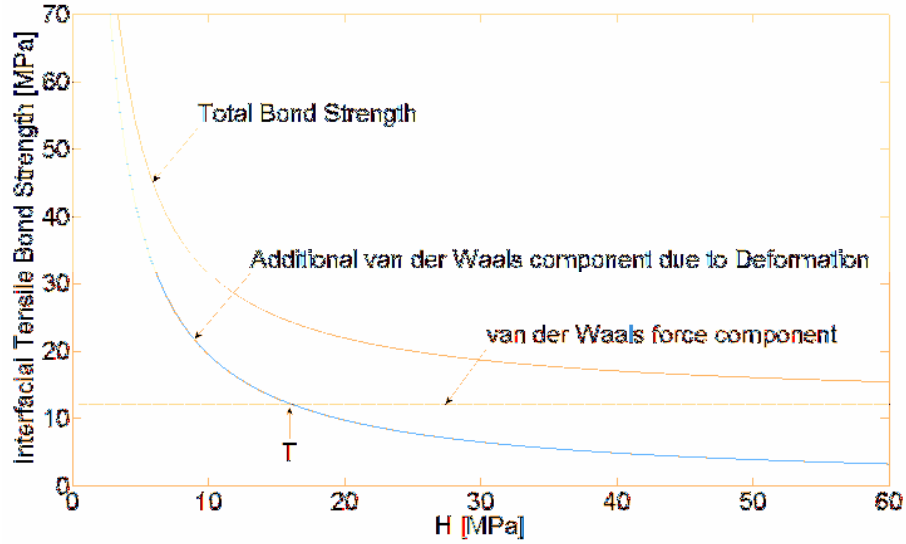
Figure 7.7 Analysis of the total interfacial tensile bond strength

$$\sigma_{NPS\ adhesion} = C_f \times 12.8 \times 10^{-10} \frac{h}{\pi\, d\, z_o^2} (1 + 6.4 \times 10^{-9} \frac{h}{z_o^3 \pi \times C_a H_{measured}}) \qquad (6.24)$$

where C_f is a fitting constant, h is the van der Waals constant in eV, d is the particle diameter in um, z_o is the adhesion distance in Å, C_a is an adjusting constant, and $H_{measured}$ is the measured substrate hardness in Pa by Vickers-like hardness test described in section 4.3.1.

$$1 = 6.4 \times 10^{-9} \frac{h}{z_o^3 \pi \times C_a H_T} \iff H_T = 6.4 \times 10^{-9} \frac{h}{C_a \pi\, z_o^3} \qquad (7.1)$$

From Equation (7.1), it can be observed that the larger van der Waals constant, h, the higher substrate hardness. That is, when the van der Waals constant is large such as inorganic materials (6.0-9.0eV) rather than organic materials (2.6eV), the substrate hardness at the higher hardness value can start significantly contributing to increase bond strength. This fact is confirmed from Figure 7.3 and 7.5 in that the transition point of inorganic materials is around 1GPa while that of organic materials is around 10MPa.

One the other hand, the larger adhesion distance, z_o, the smaller H_T. In other

words, the adhesion distance can affect the transition point of substrate hardness by moving the point to the left on the hardness axis as the adhesion distance increases. The adhesion distance effect was significant in the organic materials as in Figure 7.3, but not that much in the inorganic materials in Figure 7.5. Since the van der Waals constant is larger and the adjusting constant is much smaller for inorganic materials than those of organic materials, the change in the adhesion distance is not so significant comparing to the organic materials.

Thus, from the NPS adhesion model based on the total van der Waals force, the NPS adhesion strength can be improved either by increasing the intrinsic van der Waals force or the additional van der Waals force due to deformation. The intrinsic van der Waals force component can be increased by deceasing particle diameter and/or adhesion distance, and increasing van der Waals constant. The additional van der Waals force component due to deformation can be increased by decreasing substrate hardness and/or adhesion distance, and increasing van der Waals constant. At this point, since the van der Waals constant is fixed when the substrate material is selected and the particle diameter can be also said to be fixed as the nominal particle diameter for any chosen nano-particle metals, the ways to improve NPS adhesion strength would be decreasing substrate hardness and/or adhesion distance between silver nano particle and substrate atoms.

CHAPTER 8

ADHESION IMPROVEMENT

The NPS adhesion model has been developed as given by Equation (6.24). The two model constants, C_f and C_a, in the model have been found for organic and inorganic materials, separately. This model has been validated as the NPS adhesion model that can estimate NPS adhesion strength to electronics packaging materials with reasonable accuracy. The NPS adhesion prediction model is based on particle adhesion theory and more specifically approximates the van der Waals force as a driving force in particle adhesion.

$$\sigma_{\text{NPS adhesion}} = C_f \times 12.8 \times 10^{-10} \frac{h}{\pi\, d\, z_o^2} (1 + 6.4 \times 10^{-9} \frac{h}{z_o^3 \pi \times C_a H_{\text{measured}}}) \qquad (6.24)$$

where C_f is a fitting constant, h is the van der Waals constant in eV, d is the particle diameter in um, z_o is the adhesion distance in Å, C_a is an adjusting constant, and H_{measured} is the measured substrate hardness in Pa by Vickers-like hardness test described in section 4.3.1.

In this model, it was assumed that the omnipresent van der Waals forces is additive for assemblies of atoms and molecules, and the attraction force between larger bodies can be obtained by an integration over all pairs of atoms and molecules (Bowling, 1985). It is also assumed that the particle asperities are comparatively hard so that they can deform the opposite surface at the contact point (Zimon, 1982, Podczeck, 1996). This assumption means that the silver nano particles themselves may not be deformed when they contact the surface of substrate materials. Besides, all liquids including solvents in NPS are assumed to be evaporated at the sintering temperature of 230C, and thus any

capillary forces are assumed to be excluded in the NPS adhesion. In addition, additional interfacial reactions such as sintering, diffusive mixing, and alloying at the interface were excluded from this model, which means that the NPS adhesion prediction model is solely based on the particle adhesion associated van der Waals force. The NPS adhesion strength was obtained by dividing the total van der Waals force by the projection area of a particle, assuming that the effect of contraction during sintering on the average particle projection area was negligible.

The hardness values of organic materials in the NPS adhesion prediction model were measured using a manual Vickers hardness indenter tip made of tungsten carbide with 136° between faces. The hardness values measured are related to the model constants, C_f and C_a, in Equation (6.24), which will be changed for different hardness measurement configurations such as different indenter tip material and different tip angle. In the hardness adjustment in this study, the radius of contact was assumed not to be larger than the nominal particle radius, 4 nm. The fracture strength measurement area was assumed to be large enough to neglect the effect of the particle size distribution on the NPS adhesion strength and to estimate the adhesion strength based on the average particle size.

The van der Waals constant, which is one of the adhesion parameters in the NPS adhesion model, was assumed to be the same for all the tested organic materials to silver nano particles.

Also, some of the inorganic materials such as Cu2O, NiO, SiO2, and Ag2O were assumed for their softening coefficients of hardness to be the same as those of bare metals, Cu, Ni, Si, and Ag, respectively, because of the difficulty in finding them in the literature.

The surface energy change of etched Al was assumed to be the same as the aluminum oxide because it was impossible to measure the contact angle of the very easily

oxidized metal surface.

Based on the NPS adhesion prediction model, Equation (6.24), it is easily understood that the NPS adhesion strength can be improved either by decreasing the adhesion distance, z_o, and/or the hardness of the substrate material, $H_{measured}$.

The adhesion distance between NPS and substrate materials, Equation (6.20), could be decreased by increasing the surface energy change, $\Delta\gamma$, between them.

$$z_o[\,um\,] = 0.87 \left(\frac{h}{\Delta\gamma} \right)^{1/2} \times 10^{-3} \tag{6.20}$$

The surface energy change between NPS and substrate material can be achieved by increasing surface energy of substrate material based on Equation (4.3).

$$\Delta\gamma = \gamma_1 + \gamma_2 - \gamma_{12} \tag{4.3}$$

Substrate hardness would be decreased by increasing the sintering process temperature from Equation (4.2). Also, removing the surface oxide of metals can significantly decrease surface hardness of the metal as evidenced by the cases of copper and copper oxide (Cu2O), and aluminum and aluminum oxide (Al2O3).

$$H = H_o \exp(-S \times (T - T_o)) \tag{4.2}$$

Besides the NPS adhesion model, generating new chemical bond sites between NPS and the substrate surface using the third media such as Silane coupling agent can contribute to improving NPS adhesion.

8.1 Plasma Treatment

As a way to increase the surface energy of the substrate, plasma treatment may be a viable approach. However, in the case of NPS adhesion that requires high temperature process conditions, the plasma treatment effect for increasing surface energy of substrate

may disappear at the sintering temperature around 230C. In fact, it has been found that a temperature increase enhances polymer chain mobility and accelerates surface rearrangement, resulting in a faster recovery of the contact angle to the value of the untreated polymer surface. (Yun, 2004, Geyter, 2008)

It has been also known that plasma-treatment generates chemical bond sites in a Kapton film by cleaving some of imide groups and forming secondary amide and carboxyl groups. The cleavage of the imide rings in the Kapton films is possible because the electron energy of the plasmas is higher than the bond strength of N-C of 3eV. Breaking down the imide groups also makes Kapton films hydrophilic. (Inagaki, 1992)

Figure 8.1 shows that plasma treatments seem to improve the NPS-Kapton FPC adhesion strength, although the adhesion level is 4B, not 5B. The tape test result of the 4B NPS adhesion level for plasma-treated FPC is shown in Figure 8.2(b). Under the assumption that the contact angle of oxygen plasma-treated Kapton FPC is recovered as that of the as-received one after 1 hr of heating at 230C, the adhesion improvement is more likely to be due to the bond cleavage in the Kapton FPC film.
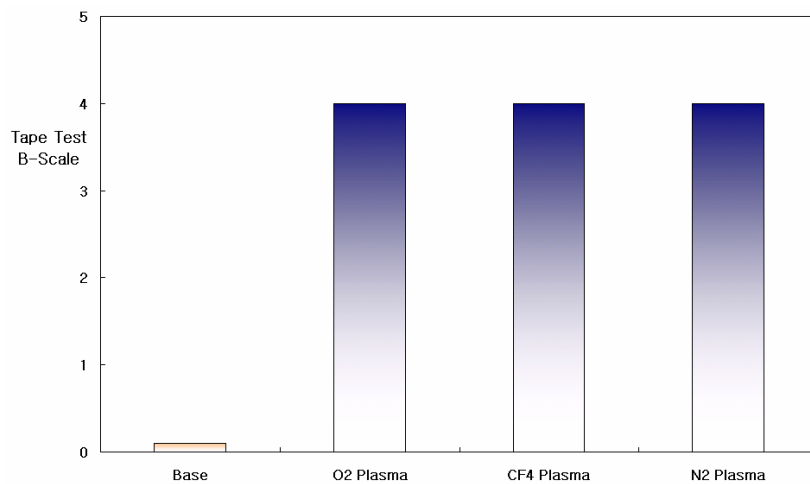

Figure 8.1 Plasma treatment effect on NPS-Kapton FPC adhesion

| (a) | (b) |
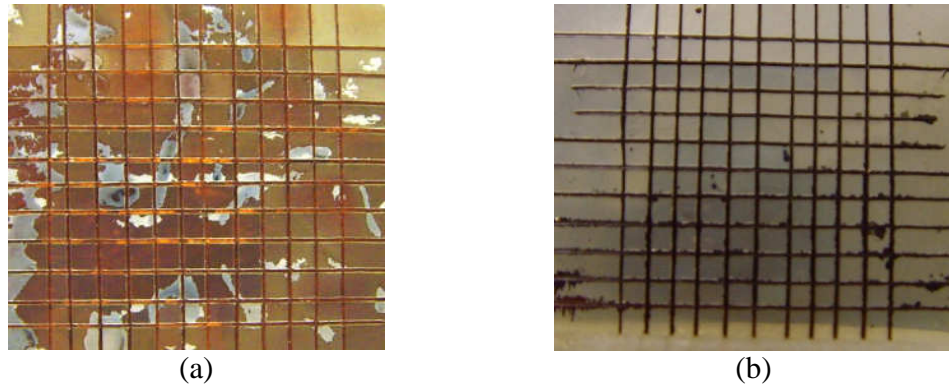
Figure 8.2 Tape Test Result for Plasma treatment effect
(a) As-received Kapton FPC (0B) and (b) O2 Plasma treated Kapton FPC (4B)

8.2 Silane Coupling Agent

As schematically shown in Figure 8.3, the Amino-silane coupling agent can improve the NPS adhesion to Kapton FPC by forming a molecular bridge at the interface between NPS and Kapton FPC (Tee, 2007). The 1.0wt% addition of Amino-silane into NPS ink turns out to be working for Kapton HN and BCB in improving the adhesion level to 5B as shown in Figure 8.4.
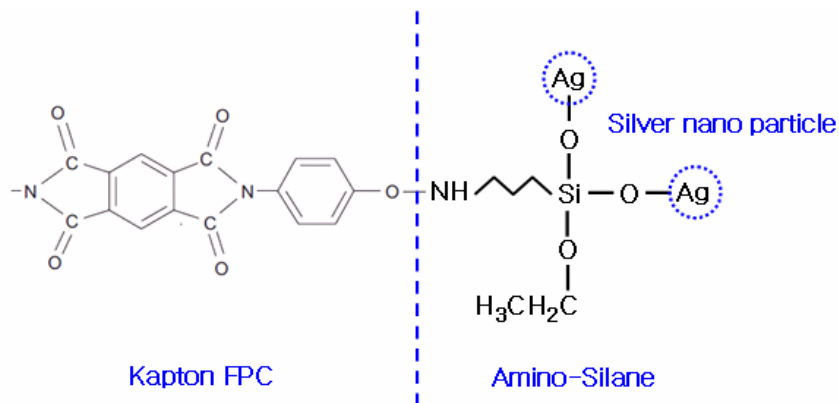

Figure 8.3 Potential chemical bond formations due to Amino-silane coupling agent
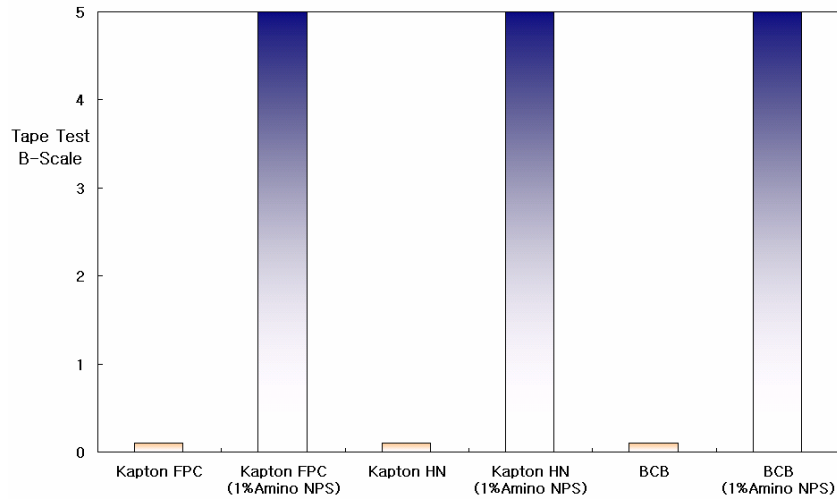
Figure 8.4 Amino-Silane addition effects

In order to understand how much the Amino-Silane coupling agent contributes to improve NPS adhesion to some organic materials such as Kapton FPC, Kapton HN, and BCB, MBST has been conducted and Kendall's model is applied to estimate the interfacial tensile bond strength.

The energy density of chemical bonding, which is equivalent to interfacial fracture energy (G_a), between Amino-NPS and substrate can be approximated once the bond density and the bond dissociation energy between Amino-NPS and substrate are known using Equation (8.1).

$$\mathrm{E_D} = D^{\circ} \times \rho_{bond} \tag{8.1}$$

where $\mathrm{E_D}$ is energy density of chemical bonding J/m^2, D° is the bond dissociation energy in J/mol, and ρ_{bond} is bond density in 1/m^2.

The bond dissociation energy of Ag-O is 221kJ/mol, while C-N is 305KJ/mol, and Si-O is 452 kJ/mol (Lide, 2006). Thus, the fracture is more likely to occur at the interface between Ag-O.

The bond density for some cases has been estimated, and they are almost in the same order of magnitude: Kinloch (1987) estimated the number of bond sites for hydroxyl (-OH) groups and carboxylic acid (-COOH) groups as $4 \times 10^{18}/m^2$ and $16 \times 10^{18}/m^2$, respectively. Fowkes (1987) estimated the number of acid-base sites for fiber-matrix composites to be $3.6 \times 10^{18}/m^2$. Yao (2000) calculated the number of reactive sites for epoxy as $1.25 \times 10^{18}/m^2$ using molecular dynamics simulation.

Thus, by taking the maximum bond density of $16 \times 10^{18}/m^2$ as the bond density of amino-silane and nano-particle silver, the interfacial fracture energy can be estimated using Equation (8.1). Equation (8.2) shows the calculation of the interfacial fracture energy based on the energy density of chemical bonds.

$$G_a = 221 \times 10^3 [\frac{\text{J}}{\text{mol}}] \times \frac{1\,\text{mol}}{6.022 \times 10^{23}} \times \frac{16 \times 10^{18}}{\text{m}^2} = 5.87[\text{J/m}^2] \qquad (8.2)$$

From Kendall's model described in section 5.2.7, Z is equal to $\sqrt{2G_a / \sum_i \frac{t_i}{K_i}}$.

Thus, additional contribution of Amino-silane coupling agent to the NPS adhesion strength can be combined with the van der Waals force contribution and can be written as Equation (8.3).

$$\sigma_{\text{NPS adhesion}} = C_f \times 12.8 \times 10^{-10} \frac{h}{\pi\,d\,z^2}(1 + 6.4 \times 10^{-9} \frac{h}{z^3 \pi \times C_a H_{\text{measured}}}) + \sqrt{2G_a / \sum_i \frac{t_i}{K_i}} \quad (8.3)$$

where C_f is a fitting constant, h is the van der Waals constant in eV, d is the particle diameter in um, z_o is the adhesion distance in Å, C_a is an adjusting constant, H_{measured} is the measured substrate hardness in Pa, Ga is interfacial fracture energy at the fracture interface in J, ti is the thickness of each layer in um, and K_i is the bulk modulus in MPa.

According to the material properties and dimensions of each component,

$\sum_{i} t_i / K_i$ and Z are calculated as in Table 8.1. Thus, Kapton FPC-NPS adhesion will be increased as much as 10.6±0.4 MPa due to the Amino-silane coupling agent, resulting in total adhesion strength of 29.2±4.3 MPa.

The interfacial tensile bond strength is measured using MBST as summarized in Table 8.2. Although the uncertainty in the Z measurement seems to be large, the predicted adhesion strength of 29.2±3.9 MPa is comparable to the measured value of 37.3±6.4 MPa.

Table 8.1 Interfacial Bond Strength of Amino-NPS/Kapton FPC interface

Materials	E [Mpa]	v	K [MPa]	t [um]	t/K [um/MPa]
Die	130000	0.28	98485	675.00	0.007
NPS	83000	0.37	106410	2.0	0.000
Epoxy	4200	0.34	4375	228±30	0.052±0.007
Kapton FPC	2800	0.34	2917	125	0.043
				$\sum_{i}\dfrac{t_i}{K_i}$	0.102±0.007
Z [MPa]		18.6±3.9	Ga [J/m^2]	17.7±7.5	
Additional Z [MPa]		10.6±0.4	Additional Ga [J/m^2]	5.9	
Total Z		29.2±3.9	Total Ga	23.6±7.5	

Table 8.2 MBST results for Amino-NPS/Kapton FPC interface

Die Configuration	$\overline{\sigma}$	$\overline{\tau}$	S	Z	Fracture Mode
Full Die	20.2±5.1	34.5±3.4	41.0±3.9	37.3±6.4	Interface
Mid Die	5.1±2.3	40.7±3.6			

8.3 Sintering Temperature

As temperature increases, substrate hardness decreases. Specially, for organic substrate materials, each has its own level of temperature at which the substrate material gets much softer, which is called a glass transition temperature (Tg). Process temperature above their glass transition temperatures significantly decreases their hardness. The hardness decrease at the NPS sintering temperature above Tg can contribute to the

increase of the interfacial adhesion strength between NPS and the organic substrate material based on the NPS adhesion prediction model.

The glass transition temperature of Kapton FPC and Kapton HN is between 360℃ and 410℃ based on the manufacturer's data (Dupont, 2009). As shown in Figure 8.5, the sintering process at 440℃ improved the adhesion level of Kapton FPC, Kapton HN, and even Glass from 0B at 230℃ sintering to 5B.

As observed in section 4.3.1, the adhesion level for organic materials depends on the substrate materials and the sintering temperatures. The adhesion levels based on the ASTM tape test with different sintering temperatures for organic substrate materials are listed in Table 8.3 along with the glass transition temperatures for the organic materials. It can be noticed that the adhesion level is distinguished at the sintering temperature below and above Tg of each material. These results verify that the NPS adhesion improvement can be achieved by decreasing substrate hardness associated with sintering temperature and glass transition temperature.
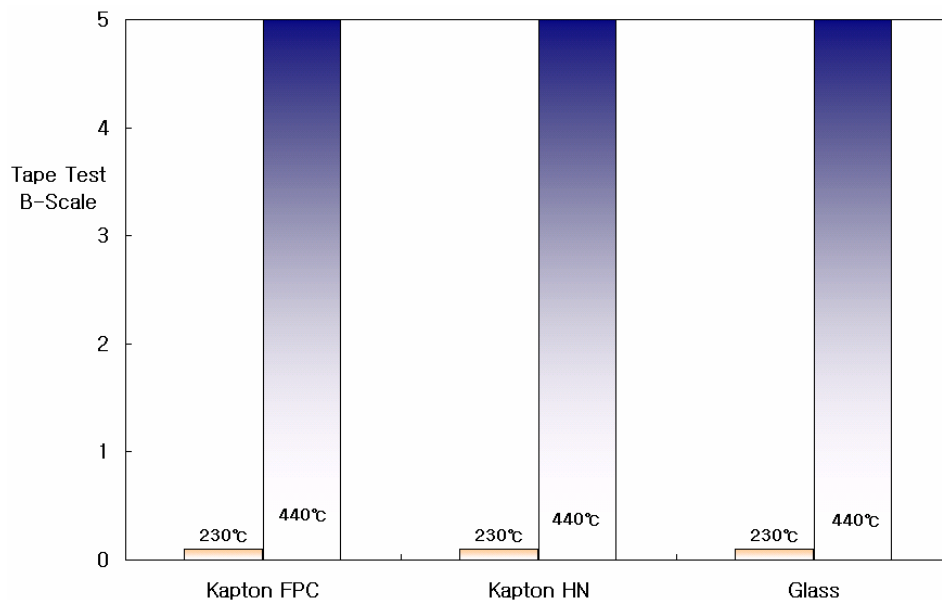

Figure 8.5 Sintering Temperature effect

Table 8.3 Tape Test Results at various sintering temperatures

Material		Kapton KJ	SS 415	BCB	FPC	HN
Tg		210℃	180-185℃	>350℃	360-410℃	360-410℃
Sintering Temp. [℃]	174	0B	0B	0B	0B	0B
	182	0B	5B	0B	0B	0B
	210	2B	5B	0B	0B	0B
	230	5B	5B	0B	0B	0B
	245	5B	5B	0B	0B	0B
	440	N/A	N/A	5B	5B	5B

8.4 Surface oxide removal

Removing the surface oxide layer can decrease the surface hardness of metals as shown in Table 7.14. The hardness decrease results in the increase of NPS adhesion strength based on the NPS adhesion prediction model. The adhesion strength increase is due to the additional van der Waals force associated with the contact area increase. The significant increase in predicted adhesion strength is for aluminum by removing the aluminum oxide layer on the surface. This increase of about 5 times in adhesion strength is expected not only because the aluminum oxide is very hard compared with other surface oxide layer, but also because the aluminum is softest of the test materials.

The softening coefficients of hardness were assumed for Cu2O, Ag2O, NiO, and SiO2 surface oxide layer as the same value for their inner materials. It is observed that since the softening coefficients of hardness for test materials are almost the same order of magnitude, the Vickers hardness at room temperature could tell the relative adhesion levels for different materials.

It should be mentioned that in this study of surface oxide removal effect on the NPS adhesion strength, diffusion was not considered, and the predicted strength in the Table 8.4 is solely based on the NPS adhesion prediction model associated with van der Waals force. Cu and potentially Ag seem to react with NPS and to form diffusion-like layer at the interface. As discussed in section 5.3.5, the interfacial tensile bond strength

between Cu and NPS based on the MBST was larger than 73.7MPa, which is appreciably

larger than 30.1Ma without diffusion as in Table 8.4.

Table 8.4 Effect of surface oxide on adhesion strength

Material	Vickers Hardness (H_o, MPa)	Softening Coefficient of Hardness (S_o, 10-4/^{o}C)	Hardness at 230°C (H, Mpa)	Predicted Adhesion Strength [MPa]
Cu2O	1600	*12.3	1206	16.1
Cu	680	12.3	512	30.1**
Al2O3	23000	7.85	19201	9.5
Al	415	23.3	243	62.6
Ag2O	1350	*9.3	1090	21.1
Ag	600	9.3	484	35.6**
NiO	4800	*10.0	3814	10.6
Ni	1325	10.0	1053	16.7
SiO2	12015	*9.5	9657	11.3
Si	2540	9.5	1672	18.5

*assumed values, **without considering diffusion

CHAPTER 9

SUMMARY AND FUTUREWORKS

9.1 Conclusions

A key mechanism of NPS adhesion to substrate materials was found to be physical bonding, which is a general particle adhesion mechanism due to van der Waals forces. Based on the van der Waals forces, an adhesion model was developed and it provides a first order estimate of the NPS adhesion strength to packaging materials. In the NPS adhesion prediction model, the significant adhesion factors were found to be substrate hardness and adhesion distance. Substrate hardness is a dominant factor in NPS adhesion strength. Adhesion distance effect calculated from surface energy change was a significant factor especially in the low hardness range. Finally, in order to improve the adhesion strength of NPS, plasma treatment, Amino-silane coupling agents, higher sintering temperature, and surface oxide removal have been verified as improvement methods.

Besides the physical bonding, diffusion or other interfacial reactions between NPS and metal substrates such as copper and silver seems to exist because a diffusion-like layer was found at the interface of silver and copper based on the AES analysis.

9.2 Contributions

An innovative rapid prototyping technology for micro-systems packages, which integrates existing technologies, has been demonstrated to potentially reduce packaging turn-around time from months to days. The rapid package prototyping technology will allow package designers to rapidly and less expensively make tangible prototypes of their

designs so that they have functional packages for testing and communicating design concepts with co-workers or customers.

A key NPS adhesion mechanism has been identified as the physical bonding mechanism attributed to van der Waals force. Since the internal van der Waals forces are high enough to deform the substrates when the substrates are heated, the NPS bonding can be achieved without external pressure as opposed to any regular bonding processes.

NPS adhesion prediction model has been developed, which provides explicit relationships between NPS interfacial tensile bond strength and adhesion factors such as substrate hardness, adhesion distance, van der Waals constant, and particle diameter. The NPS adhesion model has been verified as an appropriate adhesion model using experimental data from sixteen packaging materials.

A quantitative adhesion test method has been developed to measure NPS adhesion strength. The newly developed adhesion test method, which is called a modified button shear test (MBST), has been used for validating the NPS adhesion prediction model. The MBST is generic in nature and can be extended to other thin films' adhesion tests.

Guidelines for improving adhesion strength of NPS are provided based on the NPS adhesion prediction model. The adhesion strength can be enhanced by the contact area increase due to the substrate surface deformation. In the organic substrates to NPS adhesion, the adhesion level increases as the substrate softens and thus deforms more with increasing sintering temperature, which is an evidence of the particle adhesion mechanisms. The adhesion level increase in the inorganic substrates by removing the very hard oxide layers on the surface has been also explained by the particle adhesion mechanism.

Additional methods for NPS adhesion improvement have been evaluated. The

addition of Silane coupling agent improved the adhesion level of Kapton FPC, Kapton HN, and BCB. Plasma treatment using O2, N2, and CF4 enhanced the adhesion level of Kapton FPC and Kapton HN. Higher Sintering temperature such as 440℃ works for improving adhesion of Kapton FPC, Kapton HN, and even Glass. Removing surface oxide such as Cu2O and Al2O3 from Cu and Al substrate, respectively, contributes to adhesion improvement as expected from adhesion prediction model.

9.3 Future Works

Interfacial reactions and their effect on NPS adhesion strength between NPS and metals such as Cu and Ag needs to be investigated further since diffusion-like layer was observed in the NPS-Cu interface. Figure 9.1 shows the interface between NPS/etched Al using Focused Ion Beam (FIB) etching technique. Diffusion layer does not seem to exist from this picture. The interfacial tensile bond strength between NPS and etched Al was almost the same as that predicted from the adhesion prediction model based on van der Waals forces without considering diffusion.
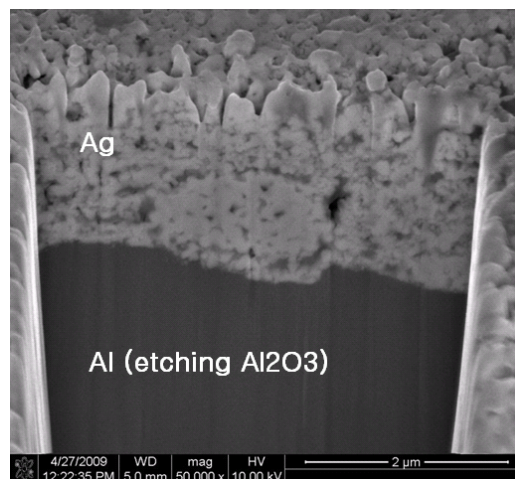
Figure 9.1 Focused Ion Beam (FIB) sample of NPS/etched Al

The adhesion mechanisms of Nano-particle Gold (NPG) and Nan-particle

Copper (NPC) are expected to be the same as that of NPS because they would have the same composition of nano-particle metal, dispersion agent coating on the particles, and solvent. In order to confirm the extendibility of adhesion mechanisms of nano-particle conductors, additional nano-particle metals such as gold and copper needs to be examined.

According to the NPS adhesion prediction model, the larger particle size, the lower strength is expected. In order to confirm this expectation, particle size effect on the adhesion strength using larger particle size than 8 nm such as 50 nm or 100nm should be experimented.

Although it is generally known that adhesion testing includes large scattering, it is recommendable to use additional interfacial bond strength measurements such as Scratch Test, Blister Test, Indentation Test, and Laser spallation test.

Effect of Adhesion on other properties such as resistivity and reliability should be studied to achieve higher performance packages. Also, the NPS thickness might be related to NPS adhesion strength because thicker NPS film tends to remain solvent in it.

APPENDIX A

MBST ANSYS CODE

```
! Unit

! Force [N], Length[um], E[N/um^2]

! Stress: N/um^2 = 10^12 Pa = 10^3 GPa

!100 GPa=0.1 N/um^2


adhesive_dia = 2345 ![um]

Fracture_Force = 116.6 ! [N]

adhesive_thick = 204 ![um]


Sub_size = 10000    ![um]


Die_size = 5000    ![um]

Die_thick = 675    ![um]

NPS_thick = 2 ![um]

LCP_thick = 50 ![um]

Cu_thick = 18 ![um]


Frac_Pressure                          =
Fracture_Force/(Die_size*Die_thick)    !
[N/um2]


esize_1 = 20    ! default = 20

esize_2 = 45    ! default = 50
```

```
esize_3 = 30    ! default = 50


/prep7

k,1,0,0,0,

k,2,0,0,adhesive_thick,

L,1,2                         ! line no.1

k,3,0,0,adhesive_thick+Die_thick,

L,2,3                         ! line no.2

k,4,0,0,-NPS_thick

L,1,4                         ! line no.3

k,5,0,0,-NPS_thick-LCP_thick

L,4,5                         ! line no.4

k,6,0,0,-NPS_thick-LCP_thick-Cu_thick

L,5,6                         !line no.5


et,1,200,6 ! plane 42 or mesh 200, 6

et,2,45        ! Brick 45


pcirc,0,Adhesive_dia/2,0,360


*do,ra,1,11

radi=2*ra*ra

pcirc,0,Adhesive_dia/2-radi,0,360
```

```
*enddo
rect,0,Sub_size/2,0,Sub_size/2
!!! x1,x2,y1,y2
rect,-Sub_size/2,Sub_size/2,0,Sub_size/2
rect,0,Sub_size/2,0,-Sub_size/2
rect,-Sub_size/2,0,-Sub_size/2,0

wpoff,0,0,adhesive_thick
!!! move working plane
pcirc,0,Adhesive_dia/2,0,360
*do,ra,1,11
radi=2*ra*ra
pcirc,0,Adhesive_dia/2-radi,0,360
*enddo
rect,0,Die_size/2,0,Die_size/2
rect,-Die_size/2,Die_size/2,0,Die_size/2
rect,0,Die_size/2,0,-Die_size/2
rect,-Die_size/2,0,-Die_size/2,0
wpoff,0,0,-adhesive_thick
!!! return to the origin

allsel
aovlap,all

asel,s,loc,z,adhesive_thick

CSYS,1
!!! Global Cylindrical Coordi.
WPCSYS,-1
asel,r,loc,x,0,adhesive_dia/2
adele,all

CSYS,1
!!! Global Cylindrical Coordinate
WPCSYS,-1
lsel,s,loc,z,0
lsel,r,loc,x,0,adhesive_dia/2
lsel,u,loc,y,0
lsel,u,loc,y,90
lsel,u,loc,y,180
lsel,u,loc,y,270
lesize,all,,,esize_2,1,,,,0

lsel,s,loc,z,0
lsel,r,loc,x,0,adhesive_dia/2-250
lesize,all,,,esize_1,2,,,,0

lsel,s,loc,z,0
lsel,r,loc,x,adhesive_dia/2-
250,adhesive_dia/2
lsel,r,loc,y,0
```

```
lesize,all,,,1,1,,,0                    mat,3              ! NPS
                                        !!!esize,3
lsel,s,loc,z,0                          amesh,all
lsel,r,loc,x,adhesive_dia/2-
250,adhesive_dia/2                      allsel
lsel,r,loc,y,90
lesize,all,,,1,1,,,0                    CSYS,0
                                        !!! Global Cartesian
lsel,s,loc,z,0                          WPCSYS,-1
lsel,r,loc,x,adhesive_dia/2-            lsel,s,loc,z,0
250,adhesive_dia/2                      lsel,r,loc,y,Sub_size/2,-Sub_size/2
lsel,r,loc,y,180                        CSYS,1
lesize,all,,,1,1,,,0                    !!! Global Cylindrical
                                        WPCSYS,-1
lsel,s,loc,z,0                          lsel,u,loc,x,0,Sub_size/2
lsel,r,loc,x,adhesive_dia/2-            lesize,all,,,esize_1,1,,,0
250,adhesive_dia/2                      lsel,s,loc,z,0
lsel,r,loc,y,270                        lsel,r,loc,y,0,360
lesize,all,,,1,1,,,0                    lsel,r,loc,x,adhesive_dia/2+10,Sub_size/2
                                        lesize,all,,,esize_2,15,,,0
allsel                                  allsel
asel,s,loc,z,0                          asel,s,loc,z,0
asel,r,loc,x,0,adhesive_dia/2           asel,u,loc,x,0,adhesive_dia/2
type,1                                  type,1              !!! area meshing
!!! mesh 200 for area meshing           mat,3              !!! NPS
```

```
amesh,all

allsel
CSYS,1
!!! Global Cylindrical
WPCSYS,-1
asel,s,loc,z,0
asel,r,loc,x,0,adhesive_dia/2
CSYS,0
!!! Global Cartesian
WPCSYS,-1
type,2
mat,2                          !!! epoxy
lsel,s,line,,1,,
lesize,all,,,5,30,,,,0      !!! epoxy NDIV: 5
vdrag,all,,,,,,1


CSYS,1
!!! Global Cylindrical Coordinate
WPCSYS,-1
lsel,s,loc,z,adhesive_thick
lsel,r,loc,x,adhesive_dia/2
lsel,r,loc,y,0,360
lesize,all,,,esize_2,1,,,,0
```

```
CSYS,0
!!! Global Cartesian Coordinate
WPCSYS,-1
lsel,s,loc,z,adhesive_thick
lsel,r,loc,y,Die_size/2,-Die_size/2
CSYS,1
!!! Global Cylindrical Coordinate
WPCSYS,-1
lsel,u,loc,x,0,Die_size/2
lesize,all,,,esize_1,1,,,,0
lsel,s,loc,z,adhesive_thick
lsel,r,loc,y,0,360
lsel,r,loc,x,adhesive_dia/2+10,Die_size/2
lsel,u,loc,x,0,adhesive_dia/2
lesize,all,,,esize_3,10,,,,0
allsel
asel,s,loc,z,adhesive_thick
asel,u,loc,x,0,adhesive_dia/2
type,1            !area meshing
mat,1                !!!!!!!! Die
amesh,all


Die_Z_node = 3


CSYS,0
```

```
!!! Global Cartesian Coordinate          asel,s,loc,z,0

WPCSYS,-1                                 lsel,s,line,,3,,

allsel                                    lesize,all,,,2,1,,,0

asel,s,loc,z,adhesive_thick               !!! NPS NDIV = 2

lsel,s,line,,2,,                          mat,3              !!! NPS

lesize,all,,,Die_Z_node,1,,,0             vdrag,all,,,,,,3

!!! Die NDIV = 3

type,2                                    allsel

mat,1              !!! Die                asel,s,loc,z,-NPS_thick

vdrag,all,,,,,,2                          lsel,s,line,,4,,

                                          lesize,all,,,5,10,,,0

!!! Add this part only for Mid Die Shear!!!   !!! LCP NDIV = 5

allsel,                                   mat,4              !!!LCP

esize,,15                                 vdrag,all,,,,,,4

asel,s,loc,y,-Die_size/2

vext,all,,,,-Die_size/2,,                 allsel

!!!!!!!!!!!!!!!!!!!!!!!!!!!!!!!!!!!!!!!!!!!!!!!!   asel,s,loc,z,-NPS_thick-LCP_thick

!!! This part only for Large Die Shear !!!   lsel,s,line,,5,,

allsel,                                    lesize,all,,,1,1,,,0

esize,,15                                 !!! Cu NDIV = 1

asel,s,loc,y,-Die_size/2                  mat,5              !!! Cu

vext,all,,,,-Die_size,,                    vdrag,all,,,,,,5

!!!!!!!!!!!!!!!!!!!!!!!!!!!!!!!!!!!!!!!!!!!!!!!!

                                          !!!--- Material Properties attributes ---!!!

allsel
```

```
allsel
nummrg,kp
nummrg,node
nummrg,kp


/number,1
/pnum,mat,1

eplot


allsel
*get,par_nd,node,0,count
*get,par_el,elem,0,count


!!!----- Material Specification ------!!!
!!! Select materials as needed!!!
/prep7


mp,ex,Die,0.13    !!! E=130 [GPa] for Die
mp,nuxy,Die,0.28
mptemp,,25,127,327
mpdata,ALPX,Die,,2.6E-6,3.22E-6,3.8E-6


mp,ex,Si,0.13    !!! 130 [GPa] for Si, SiO2
mp,nuxy,Si,0.28
mp,CTEX,Si,2.6E-6


mp,ex,Epoxy,0.0042    ! epoxy
mp,nuxy,Epoxy,0.34
mptemp,,25,119,150
mpdata,ALPX,Epoxy,,62E-6,197E-6,197E-6


mp,ex,NPS,0.083         ! Ag (NPS)
mp,nuxy,NPS,0.37
mp,ALPX,NPS,19E-6


mptemp,,25,50,100,150,200     ! LCP
mpdata,ex,LCP,,0.002255,0.0016,0.00085,0.0004,0.0002
mp,nuxy,LCP,0.3
mp,ALPX,LCP,17E-6
mp,ALPY,LCP,17E-6
mp,ALPZ,LCP,150E-6


mp,ex,Ni,0.2     ! E=200GPa for Ni
mp,nuxy,Ni,0.31
mp,ALPX,Ni,13.4E-6


mp,ex,Cu,0.127            !!! Cu
mp,nuxy,Cu,0.34
```

```
mp,ALPX,Cu,17E-6

mp,ex,Aluminum,0.070     !!! Al (70GPa)
mp,nuxy,Aluminum,0.35
mp,CTEX,Aluminum,23.1E-6

mp,ex,FPC,0.0028     !!! FPC, HN ~ BCB
mp,nuxy,FPC,0.34
mp,CTEX,FPC,20E-6

mp,ex,Si3N4,0.310    !!! Si3N4
mp,nuxy,Si3N4,0.27
mp,CTEX,Si3N4,3.3E-6


!!!----- Boundary Condition -----!!!
/solu

Asel,s,loc,z,-
(NPS_thick+LCP_thick+Cu_thick)
DA,all,all,0

allsel
Tref,150
bf,all,temp,25,,,
```

```
!!! Select for each test configuration !!!
!!!!!!!!!!!!!!!!!!!!! Full Die Shear !!!!!!!!!!!!!
/psf,pres,norm,2,0,1
Asel,s,loc,z,Adhesive_thick,Adhesive_thi
ck+Die_thick
Asel,r,loc,x,Die_size/2
SFA,all,1,pres,Frac_Pressure
!!!!!!!!!!!!!!!!!!!!!!!!!!!!!!!!!!!!!!!!!!!!!!!!!!!!!!!!!


!!!!!!!!!!!!!!!!!!! Mid Die Shear !!!!!!!!!!!!!!!
/psf,pres,norm,2,0,1
Asel,s,loc,z,Adhesive_thick,Adhesive_thi
ck+Die_thick
Asel,r,loc,x,Die_size/2
Asel,r,loc,y,0,-Die_size
SFA,all,1,pres,Frac_Pressure
!!!!!!!!!!!!!!!!!!!!!!!!!!!!!!!!!!!!!!!!!!!!!!!!!!!!!!!!!
!!!!!!!!!!!!!!!!!!! Large Die Shear !!!!!!!!!!!!!
/psf,pres,norm,2,0,1
Asel,s,loc,z,Adhesive_thick,Adhesive_thi
ck+Die_thick
Asel,r,loc,x,Die_size/2
Asel,r,loc,y,-Die_size/2,-Die_size/2-
Die_size
SFA,all,1,pres,Frac_Pressure
```

```
!!!!!!!!!!!!!!!!!!!!!!!!!!!!!!!!!!!!!!!!!!!!!!!!!!!!!!

!!!!!!!!!!!! Pull-Off !!!!!!!!!!!!
/psf,pres,norm,2,0,1
Asel,s,loc,z,Adhesive_thick+Die_thick
SFA,all,1,pres,-Frac_Pressure
!!!!!!!!!!!!!!!!!!!!!!!!!!!!!!!!!!!!!!!!!!!!!!!!!!!!!!


! Affect speed and accuracy in solution
!eqslv,iter,1e-5      ! EQuation SoLVer
Eqslv,PCG,1e-5,
!!! EQuation SoLVer = PCG !!!
PCGOPT,auto,,auto,off,off,auto


allsel
solve


!!!!! data collection along the line !!!!!
distance = 250
!!! Select angle for each test configuration
angle=0    ! Full Die & Pull-Off
angle=-30 ! Mid Die
angle=-72 ! Large Die


!!!!Avg. S_Z Calculation !!!
```

```
CSYS,1      ! Global Cylindrical Coordi.
WPCSYS,-1

nsel,s,loc,z,-NPS_thick
nsel,r,loc,y,angle
nsel,r,loc,x,adhesive_dia/2-
distance,adhesive_dia/2

*get,Node_No_z,node,,count
*Dim,Pos_z,Array,1,node_no_z+1,1
*Dim,str_z,Array,1,node_no_z+1,1

*do,j,1,node_no_z
*get,ndxmin,node,,mnloc,x
picknd=node(ndxmin,0,-NPS_thick)
*get,stress_z,node,picknd,s,z
str_z(1,j,1)=stress_z
Pos_z(1,j,1)=ndxmin
nsel,u,,,picknd
*enddo


sum_str_z=0
sum_str_z=sum_str_z+Str_z(1,1,1)*(Pos_
z(1,1,1)-(adhesive_dia/2-distance))
```

```
*do,j,2,node_no_z
sum_str_z=sum_str_z+(Str_z(1,j,1)+Str_z
(1,j-1,1))/2*(Pos_z(1,j,1)-Pos_z(1,j-1,1))
*enddo


avr_s_z=sum_str_z/distance*1000000
!!! result x 10^6 = MPa


!!!!!!!!! Avg. S_XZ Calculation !!!!!!!!!!
nsel,s,loc,z,-NPS_thick
nsel,r,loc,y,angle
nsel,r,loc,x,adhesive_dia/2-
distance,adhesive_dia/2

*get,Node_No_xz,node,,count
*Dim,Pos_XZ,Array,1,node_no_xz+1,1
*Dim,str_XZ,Array,1,node_no_xz+1,1


*do,j,1,node_no_xz
*get,ndxmin,node,,mnloc,x
picknd=node(ndxmin,0,-NPS_thick)
*get,stress_xz,node,picknd,s,xz
str_XZ(1,j,1)=stress_xz
Pos_xz(1,j,1)=ndxmin
nsel,u,,,picknd
```

```
*enddo


sum_str_xz=0
sum_str_xz=sum_str_xz+Str_XZ(1,1,1)*(
Pos_XZ(1,1,1)-(adhesive_dia/2-distance))


*do,j,2,node_no_xz
sum_str_xz=sum_str_xz+(Str_xz(1,j,1)+St
r_xz(1,j-1,1))/2*(Pos_xz(1,j,1)-
Pos_xz(1,j-1,1))
*enddo


avr_s_xz=sum_str_xz/distance*1000000
!!! result x 10^6 = MPa


!!!!!!!!!!! Avg. S_YZ Calculation !!!!!!!!!!


nsel,s,loc,z,-NPS_thick
nsel,r,loc,y,angle
nsel,r,loc,x,adhesive_dia/2-
distance,adhesive_dia/2


*get,Node_No_yz,node,,count
*Dim,Pos_yz,Array,1,node_no_yz+1,1
*Dim,str_yz,Array,1,node_no_yz+1,1
```

```
*do,j,1,node_no_yz
*get,ndxmin,node,,mnloc,x
picknd=node(ndxmin,0,-NPS_thick)
*get,stress_yz,node,picknd,s,yz
str_yz(1,j,1)=stress_yz
Pos_yz(1,j,1)=ndxmin
nsel,u,,,picknd
*enddo


sum_str_yz=0
```

```
sum_str_yz=sum_str_yz+Str_yz(1,1,1)*(P
os_yz(1,1,1)-(adhesive_dia/2-distance))


*do,j,2,node_no_yz
sum_str_yz=sum_str_yz+(Str_yz(1,j,1)+St
r_yz(1,j-1,1))/2*(Pos_yz(1,j,1)-
Pos_yz(1,j-1,1))
*enddo


avr_s_yz=sum_str_yz/distance*1000000
    !!! result x 10^6 = MPa
```

APPENDIX B

PARTIAL DERIVATIVES

For the calculation of the partial derivatives using Matlab, the symbols for average stresses were replaced as: $\overline{\tau}_1 = T1$, $\overline{\sigma}_1 = S1$, $\overline{\tau}_2 = T2$, and $\overline{\sigma}_2 = S2$.

$\dfrac{\partial S}{\partial \overline{\tau}_1} =$ pdST1 = 1/2/((T1^2*S2^2-T2^2*S1^2)/(T1^2-T2^2))^(1/2)*(2*T1*S2^2/(T1^2-T2^2)-2*(T1^2*S2^2-T2^2*S1^2)/(T1^2-T2^2)^2*T1)

$\dfrac{\partial S}{\partial \overline{\sigma}_1} =$ pdSS1 = -1/((T1^2*S2^2-T2^2*S1^2)/(T1^2-T2^2))^(1/2)*T2^2*S1/(T1^2-T2^2)

$\dfrac{\partial S}{\partial \overline{\tau}_2} =$ pdST2 = 1/2/((T1^2*S2^2-T2^2*S1^2)/(T1^2-T2^2))^(1/2)*(-2*T2*S1^2/(T1^2-T2^2)+2*(T1^2*S2^2-T2^2*S1^2)/(T1^2-T2^2)^2*T2)

$\dfrac{\partial S}{\partial \overline{\sigma}_2} =$ pdSS2 = 1/((T1^2*S2^2-T2^2*S1^2)/(T1^2-T2^2))^(1/2)*T1^2*S2/(T1^2-T2^2)

$\dfrac{\partial Z}{\partial \overline{\tau}_1} =$ pdZT1 = 1/2/(T1^2*(T1^2*S2^2-T2^2*S1^2)/(T1^2-T2^2)/((T1^2*S2^2-T2^2*S1^2)/(T1^2-T2^2)-S1^2))^(1/2)*(2*T1*(T1^2*S2^2-T2^2*S1^2)/(T1^2-T2^2)/((T1^2*S2^2-T2^2*S1^2)/(T1^2-T2^2)-S1^2)+2*T1^3*S2^2/(T1^2-T2^2)/((T1^2*S2^2-T2^2*S1^2)/(T1^2-T2^2)-S1^2)-2*T1^3*(T1^2*S2^2-T2^2*S1^2)/(T1^2-T2^2)^2/((T1^2*S2^2-T2^2*S1^2)/(T1^2-T2^2)-S1^2)-T1^2*(T1^2*S2^2-T2^2*S1^2)/(T1^2-T2^2)/((T1^2*S2^2-T2^2*S1^2)/(T1^2-T2^2)-S1^2)^2*(2*T1*S2^2/(T1^2-T2^2)-2*(T1^2*S2^2-T2^2*S1^2)/(T1^2-T2^2)^2*T1))

$$\frac{\partial Z}{\partial \sigma_1} = pdZS1 = 1/2/(T1^2*(T1^2*S2^2-T2^2*S1^2)/(T1^2-T2^2)/((T1^2*S2^2-T2^2*S1^2)/(T1^2-T2^2)-S1^2))^\wedge(1/2)*(-2*T1^2*T2^2*S1/(T1^2-T2^2)/((T1^2*S2^2-T2^2*S1^2)/(T1^2-T2^2)-S1^2)-T1^2*(T1^2*S2^2-T2^2*S1^2)/(T1^2-T2^2)/((T1^2*S2^2-T2^2*S1^2)/(T1^2-T2^2)-S1^2)^2*(-2*T2^2*S1/(T1^2-T2^2)-2*S1))$$

$$\frac{\partial Z}{\partial S} = pdZS = 1/2/(T1^2*S^2/(S^2-S1^2))^\wedge(1/2)*(2*T1^2*S/(S^2-S1^2)-2*T1^2*S^3/(S^2-S1^2)^2)$$

MATLAB CODE

```
close;
!Tensile & Shear for load 1 and load 2
syms T1 S1 T2 S2

S=SQRT((T1^2*S2^2-T2^2*S1^2)/(T1^2-T2^2));

pdST1=diff(S,T1);
pdSS1=diff(S,S1);
pdST2=diff(S,T2);
pdSS2=diff(S,S2);

syms S
Z=SQRT(T1^2*S^2/(S^2-S1^2));
pdZT1=diff(Z,T1);
pdZS1=diff(Z,S1);
pdZS=diff(Z,S);

!LCP315
T1=38.7; S1=30.1; T2=17.7; S2=45.0; S=48.1;

pdST1=1/2/((T1^2*S2^2-T2^2*S1^2)/(T1^2-T2^2))^(1/2)*(2*T1*S2^2/(T1^2-T2^2)-
2*(T1^2*S2^2-T2^2*S1^2)/(T1^2-T2^2)^2*T1)
pdSS1=-1/((T1^2*S2^2-T2^2*S1^2)/(T1^2-T2^2))^(1/2)*T2^2*S1/(T1^2-T2^2)
pdST2=1/2/((T1^2*S2^2-T2^2*S1^2)/(T1^2-T2^2))^(1/2)*(-2*T2*S1^2/(T1^2-
T2^2)+2*(T1^2*S2^2-T2^2*S1^2)/(T1^2-T2^2)^2*T2)
pdSS2=1/((T1^2*S2^2-T2^2*S1^2)/(T1^2-T2^2))^(1/2)*T1^2*S2/(T1^2-T2^2)
```

pdZT1=1/2/(T1^2*(T1^2*S2^2-T2^2*S1^2)/(T1^2-T2^2)/((T1^2*S2^2-T2^2*S1^2)/(T1^2-T2^2)-S1^2))^(1/2)*(2*T1*(T1^2*S2^2-T2^2*S1^2)/(T1^2-T2^2)/((T1^2*S2^2-T2^2*S1^2)/(T1^2-T2^2)-S1^2)+2*T1^3*S2^2/(T1^2-T2^2)/((T1^2*S2^2-T2^2*S1^2)/(T1^2-T2^2)-S1^2)-2*T1^3*(T1^2*S2^2-T2^2*S1^2)/(T1^2-T2^2)^2/((T1^2*S2^2-T2^2*S1^2)/(T1^2-T2^2)-S1^2)-T1^2*(T1^2*S2^2-T2^2*S1^2)/(T1^2-T2^2)/((T1^2*S2^2-T2^2*S1^2)/(T1^2-T2^2)-S1^2)^2*(2*T1*S2^2/(T1^2-T2^2)-2*(T1^2*S2^2-T2^2*S1^2)/(T1^2-T2^2)^2*T1))
pdZS1=1/2/(T1^2*(T1^2*S2^2-T2^2*S1^2)/(T1^2-T2^2)/((T1^2*S2^2-T2^2*S1^2)/(T1^2-T2^2)-S1^2))^(1/2)*(-2*T1^2*T2^2*S1/(T1^2-T2^2)/((T1^2*S2^2-T2^2*S1^2)/(T1^2-T2^2)-S1^2)-T1^2*(T1^2*S2^2-T2^2*S1^2)/(T1^2-T2^2)/((T1^2*S2^2-T2^2*S1^2)/(T1^2-T2^2)-S1^2)^2*(-2*T2^2*S1/(T1^2-T2^2)-2*S1))
pdZS=1/2/(T1^2*S^2/(S^2-S1^2))^(1/2)*(2*T1^2*S/(S^2-S1^2)-2*T1^2*S^3/(S^2-S1^2)^2)

!LCP315
deltaT1=4.4; deltaS1=3.9; deltaT2=2.2; deltaS2=4.0;

deltaS=((pdST1*deltaT1)^2+(pdSS1*deltaS1)^2+(pdST2*deltaT2)^2+(pdSS2*deltaS2)^2)^0.5

deltaZ=((pdZT1*deltaT1)^2+(pdZS1*deltaS1)^2+(pdZS*deltaS)^2)^0.5

APPENDIX C

SURFACE ENERGY CHANGE

The contact angles of Kapton KJ and NPS film with three different liquids were measured using Goniometer as shown in Figure 4.15, and their results are summarized in Table C.1. In the contact angle measurement, 5 replicates were used for each liquid and each substrate.

Table C.1 Contact Angles of Kapton KJ

Materials	Contact Angle [mean±σ °]			Surface Energy Change [mean, mJ/m^2]
	water	Glycerol	Diiodomethane	
Kapton KJ	70.3±5.3	59.8±3.5	28.7±1.3	89.0
NPS film	82.4±3.7	69.5±3.9	36.7±3.1	84.4

Since the surface energies of the three liquids are known as in Table C.2, the Young and Dupre equation, Equation C.1, can be used to find the surface energies of Kapton KJ and NPS film.

Table C.2 Surface energies of three liquids [mJ/m^2]

Liquids	γ_L	γ_L^{LW}	γ_L^-	γ_L^+
Water	72.80	21.80	25.50	25.50
Glycerol	64.00	34.00	3.92	57.40
Diiodomethane	50.80	50.80	0.00	0.00

$$\left. \begin{cases} \gamma_w(1+\cos\theta_{w/S}) = 2(\sqrt{\gamma_S^{LW}\,\gamma_w^{LW}} + \sqrt{\gamma_w^-\,\gamma_S^+} + \sqrt{\gamma_w^+\,\gamma_S^-}) \\ \gamma_G(1+\cos\theta_{G/S}) = 2(\sqrt{\gamma_S^{LW}\,\gamma_G^{LW}} + \sqrt{\gamma_G^-\,\gamma_S^+} + \sqrt{\gamma_G^+\,\gamma_S^-}) \\ \gamma_D(1+\cos\theta_{D/S}) = 2(\sqrt{\gamma_S^{LW}\,\gamma_D^{LW}} + \sqrt{\gamma_D^-\,\gamma_S^+} + \sqrt{\gamma_D^+\,\gamma_S^-}) \end{cases} \right\} \qquad (C.1)$$

By putting the values of surface energies into Equation (C.1), three equations in series for calculating surface energies of substrate, Kapton KJ, are obtained as Equation (C.2).

$$\begin{cases} 72.8(1+\cos(70.3)) = 2(\sqrt{\gamma_S^{LW} \times 21.8} + \sqrt{25.5 \times \gamma_S^+} + \sqrt{25.5 \times \gamma_S^-}) \\ 64.0(1+\cos(59.8)) = 2(\sqrt{\gamma_S^{LW} \times 34.0} + \sqrt{3.92 \times \gamma_S^+} + \sqrt{57.4 \times \gamma_S^-}) \\ 50.8(1+\cos(28.7)) = 2(\sqrt{\gamma_S^{LW} \times 50.8} + \sqrt{0 \times \gamma_S^+} + \sqrt{0 \times \gamma_S^-}) \end{cases} \qquad (C.2)$$

By solving the third equation in Equation (C.2), γ_S^{LW} is directly obtained for Kapton KJ as 44.72mJ/m^2. By putting this number into the two other equation and solving them, γ_S^+ and γ_S^- are obtained as 0.17 mJ/m^2 and 9.31mJ/m^2, respectively.

Likewise, the equations for NPS film can be setup as Equation (C.3), and the surface energies of NPS film can be obtained by solving the equations. The surface energies of Kapton KJ and NPS film obtained are listed in Table C.3

$$\begin{cases} 72.8(1+\cos(82.4)) = 2(\sqrt{\gamma_S^{LW} \times 21.8} + \sqrt{25.5 \times \gamma_S^+} + \sqrt{25.5 \times \gamma_S^-}) \\ 64.0(1+\cos(69.5)) = 2(\sqrt{\gamma_S^{LW} \times 34.0} + \sqrt{3.92 \times \gamma_S^+} + \sqrt{57.4 \times \gamma_S^-}) \\ 50.8(1+\cos(36.7)) = 2(\sqrt{\gamma_S^{LW} \times 50.8} + \sqrt{0 \times \gamma_S^+} + \sqrt{0 \times \gamma_S^-}) \end{cases} \qquad (C.3)$$

Table C.3 Surface energies of substrates [J/m^2]

Liquids	γ_S^{LW}	γ_S^+	γ_S^-
Kapton KJ	44.72	0.17	9.31
NPS film	42.21	0.06	3.93

The surface energy change after bonding NPS to Kapton KJ can now be calculated by putting the values of surface energies in Table C.3 into Equation (C.4), resulting in 89.0mJ/m^2.

$$\Delta\gamma = 2(\sqrt{\gamma_1^{LW}\gamma_2^{LW}} + \sqrt{\gamma_2^-\gamma_1^+} + \sqrt{\gamma_2^+\gamma_1^-}) \qquad (C.4)$$

REFERENCES

Adamson, A. W. (1967). Physical Chemistry of Surfaces. New York, Interscience.

Allara, D. L., F. M. Fowkes, et al. (1985). "BONDING AND ADHESION OF POLYMER INTERFACES." Materials science and engineering 83(2): 213-226.

Allen, G. L., R. A. Bayles, et al. (1986). "Small Particle Melting of Pure Metals." Thin Solid Films 144(2): 297-308.

Arrowsmith, D. J. (1970). Trans. Inst Met. Finish. 48: 88.

ASTM "Standard test methods for measuring adhesion by tape test."   ASTM D 3359-02.

Baxter, J. W. (1994). Industrial Minerals and Rocks. New York SME.

Bhattacharya, S. and K. L. Mittal (1978). Surf. Coat Technol. 7(413).

Bikiaris, D., P. Matzinos, et al. (2001). "Use of silane agents and poly(propylene-g-maleic anhydride) copolymer as adhesion promoters in glass fiber/polypropylene composites." Journal of Applied Polymer Science 81(3): 701-709.

Bowling, R. A. (1985). "An Analysis of Particle Adhesion on Semiconductor Surfaces." Journal of the Electrochemical Society 132(9): 2208-2214.

Brinkmann, N. R., H. F. S. III, et al. (2002). "Can the Radical Anion of Alkyl-2-cyanoacrylates Initiate Anionic Polymerization of These Instant Adhesive Monomers?" J. Phys. Chem. A 106: 847-853.

Buffat, P. h. and J. P. Borel (1976). "Size effect on the melting temperature of gold particles." Physicsal Review A 13: 2287-2298.

Bull, S. J. and E. G. Berasetegui (2006). "An overview of the potential of quantitative coating adhesion measurement by scratch testing." Tribology International 39: 99-114.

Cantrell, J. H. (2004). "Determination of absolute bond strength from hydroxyl groups at oxidized aluminum-epoxy interfaces by angle beam ultrasonic spectroscopy." J. Applied Physics 96(7): 3775-3781.

Chow, T. S. (2003). "Size-dependent adhesion of nanoparticles on rough surfaces." Journal of Physics: Condensed Matter 15: L83-L87.

Colvin, J., M. Carter, et al. (2005). Sintering behavior of silver nano-particle inks deposited by maskless mesoscale material deposition. Proceedings of Materials Science

and Technology.

Darlix, B., B. Monasse, et al. (1986). "Hardness Measurement as a Means of Determining Simultaneously the Elastic Modulus and Yield Stress of Polymers as a Function of Temperature." Polymer Testing 6: 107-120.

Daum, W., W. E. Burdick, et al. (1993). "Overlay high-density interconnect: a chips-first multichip module technology." Computer 26(4): 23-29.

De Gennes, P. G. (1974). J. Chem. Phys. 55: 572.

Derjaguin, B. V. (1955). Research 8.

Dickinson, J. T., L. C. Jensen, et al. (1994). "Fracto-emission and electrical transients due to interfacial failure." Adhesion Science and Technology 8(11): 1285-1309.

Donovan, R. P., T. Yamamoto, et al. (1993). Mater. Res. Soc. Symp. Proc. 315(3).

Dow. (2009). "Benzocyclobutene Polymer Data Sheets." from http://www.dow.com/cyclotene/solution/thermprop.htm.

Dupont. (2009). "Kapton FPC Technical Data Sheet." from http://www2.dupont.com/Kapton/en_US/assets/downloads/pdf/FPC_datasheet.pdf.

Dupont. (2009). "Kapton HN Technical Data Sheet." from http://www2.dupont.com/Kapton/en_US/assets/downloads/pdf/HN_datasheet.pdf.

Eley, D. D. (1961). Adhesion, Oxford University Press.

Fan, H. B. (2005). "An energy-based failure criterion for delamination initiation in electronic packaging." J. Adhesion Sci. Technol.

Feller, J. F. and Y. Grohens (2004). "Coupling ability of silane grafted poly(propene) at glass fibers/poly(propene) interface." Composites Part A: Applied Science and Manufacturing 35(1): 1-10.

Fowkes, F. M. (1987). "Role of acid-base interfacial bonding in adhesion." J Adhes Sci Technol 1(1): 7-27.

Fuller, S. B., E. J. Wilhelm, et al. (2002). "Ink-jet printed nanoparticle microelectromechanical systems." Journal of Microelectromechanical Systems 11(1): 54-60.

Ganghoffer, J. F. and A. N. Gent (1995). "Adhesion of a rigid punch to a thin elastic

layer." J. Adhesion and Technology 48: 75-84.

Gent, A. N. and C. W. Lin (1990). "Model Studies of the effect of surface roughness and mechanical interlocking on adhesion." J. Adhesion and Technology 32: 113-125.

Geyter, N. D., R. Morent, et al. (2008). "Influence of ambient conditions on the ageing behaviour of plasma-treated PET surfaces." Nuclear Instruments and Methods in Physics Research B 266: 3086-3090.

Good, R. J. (1992). "Contact angle, wetting, and adhesion: a critical review." J. Adhesion and Technology 6(12): 1269-1302.

Grivas, D., D. Frear, et al. (1986). "Formation of Cu/3Sn intermetallic on the reaction of Cu with 95Pb-5Sn solder." Journal of Electronic Materials 15(6): 355-359.

Horn, R. G. and D. T. Smith (1992). "Contact electrification and adhesion between dissimilar materials." Science 256(5055): 362-364.

Howatson, A. M., L. P. G., et al. (1991). Engineering Tables and Data. London, Chapman and Hall.

Hunt, S. (1993). ASME Trans. J. Electronic Packaging.

Huntsberger, J. R. (1967). "Mechanisms of adhesion." Journal of Paint Technology 39(507): 199-211.

Inagaki, N., S. Tasaka, et al. (1992). "Surface Modification of Kapton Film by Plasma Treatments." Journal of Polymer Science: Part A Polymer Chemistry 30: 1425-1431.

Israelachvili, J. (1991). Intermolecular and Surface Forces. New York, Academic.

Jeng, Y.-r. and J. Y. Chen (2005). "On the Microcontact Mechanism of Thermosonic Wire Bonding in Microelectronics: Saturation of Interfacial Phenomena." Tribology Transactions 48: 127-132.

Joo, S. C. and D. F. Baldwin (2006). "Reliability of a rapid package prototyping technology based on a data-driven chip-first approach." Proceedings of Electronic Components and Technology: 1899 – 1904.

Kalpakjian, S. and S. R. Schmid (2007). Manufacturing Processes for Engineering Materials. New York, Prentice Hall.

Kendall, K. (1971). "The adhesion and surface energy of elastic solids." J. Phys. D: Apply. Phys. 4.

Kinbara, A. and I. Kondo (1993). "Adhesion measurement of thin metal films by scratch, pull, and peel methods " J. Adhesion Sci. Technol. 7(8): 767-782.

Kingergy, W. D. and M. Berg (1955). "Study of the Initial Stages of Sintering Solids by Viscous Flow, Evaporation-Condensation, and Self-Diffusion." Journal of Applied Physics 26(10).

Kinloch, A. J. (1979). Jounral of Adhesion 10(193).

Kinloch, A. J. (1980). "The science of adhesion Part I - Surface and Interfacial aspects." J. Mater. Sci. 15(2141).

Kinloch, A. J. (1987). Adhesion and adhesives: Science and Technology. New York, Springer.

Kitchener, J. A. (1973). J. Soc. Cosmet. Chem. 24(709).

Kohl, J. G. and I. L. Singer (1999). "Pull-off behavior of epoxy bonded to silicone duplex coatings." Progress in organic coatings 36: 15-20.

Krupp, H. (1967). Adv. Colloid Interface Sci. 1(111).

Lee, H. Y. and J. Qu (2003). "Microstructure, adhesion strength and failure path at a polymer/roughened metal interface." J. Adhesion Science and Technology 17(2): 195-215.

Lee, L. H. (1991). Adhesive Bonding. New York and London, Plenum Press.

Lee, Y. G. and J. G. Duh (1999). "Interfacial morphology and concentration profile in the unleaded solder/Cu joint assembly." Journal of Materials Science: Materials in Electronics 10(1): 33-43.

Li, J., W. Fuliang, et al. (2008). "Theoretical and experimental analyses of atom diffusion characteristics on wire bonding interfaces." J. Phys. D: Appl. Phys. 41.

Lide, D. R. (2006). CRC Handbook of Chemistry and Physics.

London, F. (1930). Z. Phys. 63(245).

Manesh, H. D. and A. K. Taheri (2004). "Study of mechanisms of cold roll welding of aluminium alloy to steel strip." Materials Science and Technology August 20: 1064-1068.

Mealey, S., L. Stelandre, et al. (2006). "Impact of silane on dispersion and performance

of submicronic filled polymers." Rubber World 234(1): 27-29.

Megusar, J. (1997). "Low temperature fast-neutron and gamma irradiation of Kapton ® polyimide films." Journal of Nuclear Materials 245: 185-190.

Murali, S., Srikanth, N., Wong, Y. M., Charles, J. Vath III (2007). "Fundamentals of thermo-sonic copper wire bonding in microelectronics packaging." J Mater Sci 42: 615-623.

Oda, M. (2005). "Film Formation using Individually Dispersed Nano-Particle Inks and Pastes with existing Printing Technologies." ULVAC Technical Journal 61E: 5~17.

Parent, J. O. G., Chung, D.D.L., Bernstein, I.M., (1988). "Effects of intermetallic formation at the interface between copper and lead-tin solder." J. Materials Science 23(7): 2564-2572.

Park, S. J., J. S. Jin, et al. (2000). "Influence of silane coupling agents on the surface energetics of glass fibers and mechanical interfacial properties of glass fiber-reinforced composites." J. Adhesion Science and Technology 14(13): 1677-1689.

PATEL, K. S., S. A. BIDSTRUP-ALLEN, et al. (1998). "NOVEL TECHNIQUE FOR MEASURING THROUGH-PLANE THERMO-MECHANICAL PROPERTIES OF THIN POLYMER FILMS." Mat. Res. Soc. Symp. Proc. 511: 183 - 189.

Pauling, L. (1960). The Natural of the Chemical Bond and the Structure of Molecules and Crystal. New York, Cornell University Press.

Peschel, G. and K. H. Aldfinger (1970). J. Colloid. Interface Sci. 34: 505.

Pocius, A. V. (2002). Adhesion and Adhesives Technology. Cincinnati, Hanser/Gardner Publications.

Podczeck, F., J. M. Newton, et al. (1996). "The estimation of the true area of contact between microscopic particles and a flat surface in adhesion contact." J. Appl. Phys. 79(3).

Possart, W. (1988). "Experimental and theoretical description of the electrostatic component of adhesion at polymer/metal contacts." International Journal of Adhesion and Adhesives 8(2): 77-83.

Princen, H. M. (1969). Surface and Collid Science. New York, Wiley-Interscience.

Ranade, M. B. (1987). Aerosol. Sci. Technol. 7(161).

Roberts, A. D. and A. B. Othman (1977). "Rubber adhesion and the dwell time effect." Wear 42(1): 119-133

Rogers. (2009). "ultralam 3000 liquid crystal polymer circuit material." from http://www.rogerscorp.com/documents/730/acm/ULTRALAM-3000-LCP-laminate-data-sheet-ULTRALAM-3850.aspx.

Shi, S. and C. P. Wong (1999). "Recent advances in the development of no-flow underfill encapsulants - a practical approach towards the actual manufacturing application." IEEE Trans-Electronics Packaging Manufacturing 22(4): 331-339.

Shimosaka, A. (2003). "Sintering Mechanism of Two Spheres Forming a Homogeneous Solid Solubility Neck,." KONA 21: 219-233.

Shirzadi, A. A., H. Assadi, et al. (2001). "Interface evolution and bond strength when diffusion bonding materials with stable oxide films." Surface and Interface Analysis 31: 609-618.

Shyu, S. S. and S. M. Chen (1985). "Effect of silane coupling agent on glass-fiber reinforced composite." Journal of the Chinese Institute of Chemical Engineers 16(4): 311-316.

Sun, T. C. (1998). J. Reinf. Plast. Composit.

Tan, F., X. Qiao, et al. (2005). "Effects of coupling agents on the properties of epoxy-based electrically conductive adhesives." Int J Adhes Adhe 26(6): 406- 413.

Tee, D. I. and e. al (2007). "Effect of silane-based coupling agent on the properties of silver nanoparticles filled epoxy composites " Composites Science and Technology 67: 2584-2591.

Toikka, G., G. M. Spinks, et al. (2001). "Fine Particle Adhesion Measured at Elevated Temperatures Using a Dedicated Force Rig." Langmuir 17: 6207-6212.

Topper, M., K. Buschick, et al. (1997). Embedding technology-a chip-first approach using BCB. Advanced Packaging Materials. Proceedings, 3rd International Symposium on.

Towle, S. N. and H. C. Braunisch (2001). Bumpless build-up layer packaging. Proceedings of ASME International Mechanical Engineering Congress and Exposition (IMECE).

Trunov, M. A., M. Schoenitz, et al. (2005). "Effect of polymorphic phase transformations in Al2O3 film on oxidation kinetics of aluminum powders." Combustion and Flame 140:

310-318.

Valli, J. (1986). "A review of adhesion test methods for thin hard coatings." J. Vac. Sci. Technol. A 4(6): 3007-3014.

Van Oss, C. J. and R. J. Good (1990). "Estimation of the polar surface tension parameters of Glycerol and Formamide for use in contact angle measurement on polar solids." J. Dispersion science and technology 11(1): 75-81.

Vasenin, R. M. (1969). Problems in the diffusion theory of adhesion of polymers, in: Adhesion, Fundamentals and Practice. London, Ministry of Technology, U.K. Gordon and Breach.

Venables, J. D. (1984). "Adhesion and durability of metal-polymer bonds." J. Mater. Sci.(19).

Vest, R. W. (1986). "Materials science of thick film technology." American Ceramic Society Bulletin 65(4): 631-636.

Visser, J. (1975). Surf. Colloid Sci. 8(3).

Visser, J. (1995). "PARTICLE ADHESION AND REMOVAL: A REVIEW." Particulate Science and Technology 13(3): 169 - 196.

Voyutskii (1963).

Wang, H. L. and M. H. Hon (1999). "Temperature dependence of ceramics hardness." Ceramics International 25 267-271.

Waterhouse, G. I. N., G. A. Bowmaker, et al. (2001). "The thermal decomposition of silver (I, III) oxide : A combined XRD, FT-IR and Raman spectroscopic study." Phys. Chem. Chem. Phys. 3: 3838-3845.

Wu, S. and H. K. Chuang (1986). "Diffuse interface between polymers: structure and kinetics." J. Polymer Science: Polymer Physics Edition 24: 143-159.

Wu, X., E. Sacher, et al. (1999). "The effects of hydrogen bonds on the adhesion of inorganic oxide particles on hydrophilic silicon surfaces." Journal of Applied Physics 86(3): 1744-1748.

Xiang, D., M. Chen, et al. (2008). "Adhesive strength of CVD diamond thin films quantitatively measured by means of the bulge and blister test." Journal of University of Science and Technology Beijing 15(4).

Yao, Q. (2000). Modeling and Characterization of Interfacial Adhesion and Fracture, Georgia Institute of Technology.

Yi, S. (2000). "A failure criterion for debonding between Encapsulants and leadframes in plastic IC packages." J. Adhesion Sci. Technol. .

Yosomiya, R. (1989). Adhesion and Bonding in Composites. London, CRC.

Yu, J. and J. Y. Song (2002). "Analysis of the T-peel strength in a Cu/Cr/Polyimide system,." Acta Materialia 50(16): 3985-3994.

Yu, N. (2004). "Adhesive contact based on the Lennard–Jones potential: a correction to the value of the equilibrium distance as used in the potential " J. Colloid and Interface Science 278: 428-435.

Yun, Y. I., K. S. KIM, et al. (2004). "Aging behavior of oxygen plasma-treated polypropylene with different crystallinities." J. Adhesion Sci. Technol. 18(11): 1279-1291.

Zhang, J., S. Xie, et al. (2004). "Lithium insertion in naturally surface-oxidized copper." Journal of Power Sources 137 88-92.

Zimon, A. D. (1982). Adhesion of Dust and Powders. New York, Consultants Bureau.